

On the evolution of field galaxies

Thesis by

David W. Hogg

In Partial Fulfillment of the Requirements

for the Degree of

Doctor of Philosophy



California Institute of Technology

Pasadena, California

1998

(Submitted November 25, 1997)

© 1998

David W. Hogg

All Rights Reserved

Acknowledgements

I enjoyed graduate school immensely. I attribute this unconventional feeling to having had Roger Blandford as my advisor. He has great physical intuition; he works on the most interesting scientific problems; he is a generous mentor who cares about his students and colleagues; and he has an unlimited sense of humor. Roger has taken care of me academically and professionally for five years and for this I owe him a huge debt. He has also been a great friend.

The first scientific observations with the Keck Telescope were taken just about when I arrived at Caltech; it would not have been possible for me to get involved without the generosity of Judy Cohen, Gerry Neugebauer and Tom Soifer. All three patiently helped me understand how to plan, take, reduce and understand difficult observations with the finest instruments. They also deserve thanks, along with Keith Matthews and Bev Oke, from the entire Keck and Palomar communities, for instrument design, construction and maintenance. I want to specifically thank Judy for involving me in every aspect of the redshift survey and for giving me my first opportunities to go to Keck.

Caltech has a tremendous faculty; it is great to work with the omniscient Sterl Phinney, and I have learned from and enjoyed talking to George Djorgovski, Steve Frautschi, Fiona Harrison, Jim McCarthy, Mark Metzger, Tom Prince, Tony Readhead, Neill Reid, Anneila Sargent, Wal Sargent and Chuck Steidel. The graduate students and postdocs at Caltech are of the same caliber; it has been both fun and educational to collaborate with Lee Armus, Chris Fassnacht, Tomislav Kundić, James Larkin, Mike Pahre, Ian Smail and Lin Yan.

It is impossible to make it through graduate school without very supportive friends. In particular Lee Armus, Ken Banas, Blanton Bartlett, Rebecca Bernstein, Deepto Chakrabarty, Chris Darroch, Mary Eddy, Mathew Englander, Chris Fassnacht, Rachel Gibbons, John Gizis, John Hartman, Christina Hood, Mindy Kellogg,

Penny Kneebone, Adam Leibovich, Lori Lubin, Hideo Mabuchi, Lou Madsen, Peter Mao, David McMillen, Greg McDonald, Paul Ray, Alycia Rossiter, Alice Shapley, Quentin Turchette and Alan Wiseman all saved me in different ways. I actually owe my sanity variously to Banas, Fassnacht, Gizis and Penny. My mother and father, Fran and Peter, and my sister, Anne, provided encouragement and understanding. Heather Stratton, my wife during most of this project, constantly inspired me with love, humor and style; I will miss her.

Financial support was provided by an NSF Fellowship, several NSF grants, several NASA HST data reduction grants, and grants from the Kingsley Foundation. Thanks go to the members of society who understand the value of pure scientific research. Much of the thesis is based on data acquired at the Keck Observatory, operated jointly by Caltech and the University of California; the Palomar Observatory, owned and operated by Caltech; and the NASA/ESA Hubble Space Telescope, operated by NASA. The Hubble Deep Field (HDF) database was planned, taken, reduced and made public by a large team at Space Telescope Science Institute headed by Bob Williams. Text was set with \LaTeX and all but one of the Figures were made with SM. This research made use of the NOAO/IRAF software, the NASA Extragalactic Database, and the Astrophysics Data System.

Abstract

This thesis presents the analysis of spectroscopic and photometric data on faint galaxies in an 8-arcmin diameter region centered on the Hubble Deep Field. Source detection and photometry is performed in the U_n , G , \mathcal{R} and K_s -band images to create catalogs complete to $U_n = 25$, $G = 26$, $\mathcal{R} = 25.5$ and $K_s = 20$ mag. Number counts and color distributions are consistent with those found in other, similar imaging surveys. Keck Telescope spectroscopy exists for 483 sources in the sample.

The rest-frame equivalent widths of the [O II] 3727 Å emission line are measured as a function of galaxy flux, color and redshift. The probability that a source of a given flux, color and redshift has its [O II] line detected is estimated. [O II] line luminosity functions and integrated [O II] line luminosity densities are computed; they show strong evolution, implying a much higher star formation rate density at redshifts $z > 0.6$ than locally.

The spectroscopic survey is incomplete; not all selected sources have been observed spectroscopically, and not all observed sources have redshifts. Four methods for estimating the luminosity function in an incomplete survey are developed, three based on the maximum-likelihood method. Simulated catalogs which accurately reproduce the redshift structure and redshift-incompleteness found in real redshift surveys are created and used to test the methods for bias. All methods are biased for “steep” (i.e., dwarf-rich) luminosity functions.

The B -band luminosity function for the \mathcal{R} -selected sample is computed using an estimate of the probability that a source is assigned a redshift given that it has been observed spectroscopically, based on the [O II] detection probability. The luminosity function is flat (constant number per log luminosity) and consistent with local determinations except for a higher overall normalization. No evidence is found for dependence of the luminosity function on redshift or environment, but the blue galaxy luminosity function is more dwarf-rich than the red.

It is argued that, taken together, the observations support the existence of a dwarf-dominated, strongly star forming galaxy population in the past which merged into (or otherwise became physically associated with) the luminous galaxies observed locally.

Contents

Acknowledgements	iii
Abstract	v
1 Introduction	1
1.1 The number problem	1
1.2 Local galaxies	4
1.3 Galaxy evolution	7
1.4 Cosmogony	10
1.5 Cosmography	11
1.6 This thesis	13
References	13
2 Source detection and photometry in the Hubble Deep Field survey region	19
2.1 Introduction	19
2.2 Data	20
2.3 Source detection	21
2.4 Calibration with HST imaging	21
2.5 Photometry	22
2.6 Color measurement	23
2.7 Completeness	23
2.8 Discussion	24
Acknowledgements	25
References	25

3	Faint galaxy oxygen-II emission, redshift identification, and star formation rates	33
3.1	Introduction	33
3.2	Sample, observations, and line measurement	35
3.3	Equivalent width distributions	36
3.4	Equivalent width distribution model	39
3.5	Instrumental sensitivity to line emission	40
3.6	Line detection probability function	43
3.7	The [O II] luminosity function	44
3.8	The [O II] luminosity and star formation rate densities	46
	References	47
4	Determination of the galaxy luminosity function from an incomplete redshift survey	62
4.1	Introduction	62
4.2	Luminosity estimation	63
4.3	Completeness functions	65
4.4	Luminosity function determination methods	66
4.4.1	Generalized V-max method	66
4.4.2	Generalized STY method	68
4.4.3	ASF method	69
4.4.4	BFR method	71
4.5	Simulated redshift surveys	71
4.6	Tests	73
	References	75
5	The luminosity function of field galaxies and its evolution at redshifts $z < 1.5$	86
5.1	Introduction	86
5.2	Sample	88
5.3	Methods	89

5.4	Completeness functions	91
5.5	Luminosity function results	93
5.5.1	Whole sample results	93
5.5.2	Division by redshift	94
5.5.3	Division by color	95
5.5.4	Division by environment	95
5.6	Discussion	96
	References	97
6	The evolution of field galaxies	109
	References	114
A	Magnitude systems	116
A.1	Vega-relative magnitudes	116
A.2	A note on absolute calibration	117
A.3	Absolute magnitudes	118
A.4	“AB” magnitudes	118
A.5	Transformations between magnitudes	119
	Acknowledgments	119
	References	120
B	Distance measures in cosmology	124
B.1	Introduction	124
B.2	Cosmographic parameters	124
B.3	Redshift	126
B.4	Comoving distance (line-of-sight)	127
B.5	Comoving distance (transverse)	128
B.6	Angular diameter distance	130
B.7	Luminosity distance	130
B.8	Parallax distance	132
B.9	Comoving volume	132

B.10 Lookback time	133
B.11 Probability of intersecting objects	133
Acknowledgments	134
References	134
C Computer code	142
C.1 Cosmography routines in “cosmography.c”	142
C.2 Luminosity function estimation and simulation routines in “glf.c” . .	148
Biography	164

List of Figures

2.1	The final K_s -band mosaic.	27
2.2	Comparison of ground-based visual and transformed HST magnitudes.	28
2.3	U_n -selected sample numbers and colors.	29
2.4	G -selected sample numbers and colors.	30
2.5	\mathcal{R} -selected sample numbers and colors.	31
2.6	K_s -selected sample numbers and colors.	32
3.1	Example [O II] lines.	50
3.2	Rest-frame [O II] equivalent widths vs. redshift.	51
3.3	Rest-frame [O II] equivalent widths vs. magnitude.	52
3.4	Rest-frame [O II] equivalent widths vs. luminosity.	53
3.5	Rest-frame [O II] equivalent widths vs. color.	54
3.6	Scaled [O II] equivalent widths W/w	55
3.7	The distribution of sensitivities to [O II] emission.	56
3.8	The probability of detecting [O II] emission.	57
3.9	The a priori completeness function for the [O II] measurement sample.	58
3.10	The [O II] luminosity function.	59
3.11	The [O II] luminosity function as a function of redshift.	60
3.12	The [O II] luminosity and SFR density as a function of redshift.	61
4.1	Spectral index distribution function.	80
4.2	Example single-field redshift-survey simulation.	81
4.3	Another example single-field redshift-survey simulation.	82
4.4	Results of tests of the generalized V-max method.	83
4.5	Results of the STY, ASF and BFR methods.	84
4.6	Relationships between the STY, ASF and BFR methods.	85

5.1	Comparison of number counts in sample.	100
5.2	The <i>a priori</i> completeness function.	101
5.3	Basic V-max GLF results.	102
5.4	Basic maximum-likelihood GLF results.	103
5.5	V-max GLF results as a function of redshift.	104
5.6	Maximum-likelihood GLF results as a function of redshift.	105
5.7	Maximum-likelihood GLF results as a function of world model.	106
5.8	ASF method GLF results vs. color and redshift.	107
5.9	STY method GLF results vs. environment and redshift.	108
A.1	The Hayes (1985) calibrated spectrum of Vega.	123
B.1	The dimensionless proper motion distance D_M/D_H	135
B.2	The dimensionless angular diameter distance D_A/D_H	136
B.3	The dimensionless luminosity distance D_L/D_H	137
B.4	The distance modulus DM	138
B.5	The dimensionless comoving volume element $(1/D_H)^3 (dV_C/dz)$	139
B.6	The dimensionless lookback time t_L/t_H and age t/t_H	140
B.7	The dimensionless differential intersection probability dP/dz	141

List of Tables

2.1	Imaging data parameters	26
3.1	Fractions of sources in [O II] equivalent width bins	49
4.1	Recent luminosity function determinations	76
4.2	Luminosity function determination as a function of galaxy number . .	77
4.3	Luminosity function determination as a function of faint end slope . .	78
4.4	Luminosity function determination as a function of redshift and world model	79
A.1	Vega-relative magnitude wavelengths, frequencies and absolute calibra- tions.	121
A.2	Neugebauer's Vega-relative magnitude wavelengths, frequencies and zeropoints.	122

Chapter 1 Introduction

1.1 The number problem

Even the darkest, blankest patch of sky, in between Galactic stars and bright, nearby galaxies, is teeming with hundreds of thousands of sources of light per square degree (Hall & MacKay 1984; Tyson 1988; Koo & Kron 1992; Djorgovski *et al.* 1995; Metcalfe *et al.* 1995; Smail *et al.* 1995; Hogg *et al.* 1997b). These sources are so faint that they can only be detected over the emission of the night sky after hours of integration time with a near-perfect photon detector on a telescope ten meters in diameter. They are small (fractions of an arcsecond), irregular and fuzzy; they are thought to be distant galaxies, small and faint because they are so far away. With the Hubble Deep Field observations taken in 1995 (Williams *et al.* 1996) with the Hubble Space Telescope, the deepest image of blank sky ever taken, the number of these faint galaxies is now measured to be 8×10^{10} over the whole sky (although only a patch of 5 arcmin^2 solid angle has actually been observed to this depth). At the faintest detectable levels, the number of sources is increasing rapidly with depth; the number of faint galaxies roughly doubles every time the surveys are pushed a magnitude fainter (magnitudes are defined in Appendix A) and there is no sign of this trend letting up.

The Universe is big; why worry about these eighty billion galaxies? The Universe is indeed big, but it is not infinite, at least not that part of it visible to us. The total number of faint galaxies expected can be easily computed based on the local number density of galaxies, which is something on the order of a few 10^8 per Hubble volume (Efsthathiou *et al.* 1988; Loveday *et al.* 1992; Marzke *et al.* 1994a; Lin *et al.* 1996, 1997; Griffiths *et al.* 1997; Ratcliffe *et al.* 1997; Hubble volumes are defined in Appendix B) times the volume of the visible Universe, which ought to be just a few Hubble volumes, although this does depend on cosmological model (Appendix B). This order of magnitude argument suggests that there is a factor of 10 to 100 discrepancy and

the discrepancy will only get worse as deep images get deeper.

There are many possible resolutions to this “number problem.” (1) There could be a huge population of galaxies with low surface brightnesses which are not detected in local surveys but which nonetheless contribute significantly to deep counts (McGaugh 1994). It is currently thought that galaxies may exist with a wide range of surface brightnesses (McGaugh *et al.* 1995), while only the brightest are noticeable in the wide-field photographic plate surveys which have been used to survey the local Universe. The ultra-deep images used to measure faint counts, on the other hand, are sensitive to extremely faint surface brightnesses. (2) Dwarf (*i.e.*, low intrinsic luminosity) galaxies visible at moderate redshift (recall that because the Universe is expanding, redshift is related to distance and because light travels at finite speed, distance is related to lookback time; see Appendix B) may fade or evaporate with time and therefore not appear in local surveys (Babul & Rees 1992; Babul & Ferguson 1996). Galaxies are expected to be brighter in their youths because bright, massive stars burn out more quickly than the dimmer ones with lower masses; low-mass galaxies are doubly subject to this effect because the mechanical energy output of their first burst of star formation can eject from the galaxy the materials which would be needed for future episodes of star formation. Some possible evidence for this fading-dwarf type of model comes from redshift surveys which show an increasing significance of low-luminosity galaxies in the luminosity function with redshift (Broadhurst *et al.* 1988; Eales 1993; Treyer & Silk 1994; Lilly *et al.* 1995; Ellis *et al.* 1996). On the other hand, such models tend to produce a lot of infrared-bright remnants locally because the faded galaxies are left with a population of old, dim stars (Babul & Ferguson 1996). Such remnants are not seen in near-infrared faint galaxy counts (Djorgovski *et al.* 1995) or faint galaxy colors (Hogg *et al.* 1997a). (3) If the galaxy-galaxy merger rate is high, large numbers of small objects at high redshift will evolve into much smaller numbers of large galaxies locally (Rocca-Volmerange & Guiderdoni 1990; Pascarelle *et al.* 1996). Merging must be a significant process because it is seen happening in the local Universe; in fact, the Milky Way is currently merging with the small and large Magellanic clouds and the recently-discovered Sagittarius dwarf

galaxy (*e.g.*, Ibata *et al.* 1997). (4) It could be that at very faint levels, galaxies contain multiple bright patches of star formation in otherwise fairly quiescent larger bodies and those bright patches are erroneously counted as separate galaxies. There are hints from the faint-galaxy angular autocorrelation function that this might be a significant problem (Colley *et al.* 1997). (5) More speculatively, standard cosmological theory could be wrong and the Universe might be much more voluminous than is currently believed. If the cosmological world model is dominated by a cosmological constant term, it would contain significantly more volume than the standard world models (Fukugita *et al.* 1990; Yoshii & Sato 1992). Unfortunately, solving the number problem by changing the world model alone forces consideration of truly extreme models such as “loitering universes” which would make many other results in cosmology (such as the incidence of gravitational lensing or the growth of gravitationally bound large-scale structure) difficult to understand.

It may be an important clue that number counts divided by morphological type show an increasing fraction of irregular galaxies at faint (and therefore presumably high-redshift) flux levels (Griffiths *et al.* 1994a, 1994b; Glazebrook *et al.* 1995a; Driver *et al.* 1995; Abraham *et al.* 1996; Odewahn *et al.* 1996), as if galaxies start out ratty and evolve into the regular galaxies seen locally over the age of the Universe. If these faint galaxies are at moderate redshift, they are being observed in the rest-frame ultraviolet where even local grand design galaxies appear more ratty (Giavalisco *et al.* 1996; Marcum & O’Connell in prep; Abraham *et al.* in prep), but it has been argued that the effect nonetheless represents a real evolution in the galaxy population since high redshift (Odewahn *et al.* 1996). Also, faint galaxies are smaller in angular extent than the predictions for the appearance of a galaxy equivalent to the Milky Way but at high redshift (Griffiths *et al.* 1994b; Smail *et al.* 1995); again this could be in part a wavelength-dependence of morphology (Giavalisco *et al.* 1996). It could also be an observational bias, related to standard techniques for performing surface photometry (Hogg & Bernstein in preparation).

To resolve these issues, redshift surveys are undertaken in which spectrographs are used to measure the redshifts, and hence radial distances (Appendix B) for a large

number of galaxies to determine their intrinsic luminosities (among other things). This thesis presents the analysis of one such survey. Although some of the simpler faint galaxy models can be ruled out with existing spectroscopic surveys, the resolution of the number problem will be found by somehow obtaining redshift distribution information at very faint magnitudes, fainter than the ability of current telescopes and spectrographs to measure spectroscopic features. There are several methods for getting a handle on the redshift distribution at magnitudes fainter than the current capabilities of spectroscopy, none of which has been properly implemented. The ultraviolet-dropout technique (Steidel *et al.* 1996a, 1996b; Madau *et al.* 1996)—*i.e.*, finding the spectral break caused by the opacity of galaxies and the intergalactic medium to Lyman limit photons with broadband photometry—can be pushed to lower redshift with deep far-ultraviolet imaging with the Hubble Space Telescope. This would provide a strong discriminant among the various models which put very different fractions at redshifts $z > 1$. The multiple-imaging gravitational lens rate among faint galaxies is a strong function of redshift distribution, so a comparison of the optical galaxy lens rate with the radio galaxy or quasar lens rate (for the sources of which the redshift distribution is known) would put a strong constraint on faint galaxy models (Hogg *et al.* 1996a; Blandford *et al.* in preparation). If the bulk of faint galaxies are at $z < 1$, their supernovae ought to be detectable in deep images taken weekly or monthly with 4–10 meter telescopes, whereas if the galaxies are at higher redshift, the supernovae will only be visible to the Hubble Space Telescope. For this reason, the “blank-sky” supernova rate, brightness distribution and color distribution can be used to put quantitative constraints on the faint galaxy redshift distribution.

1.2 Local galaxies

Containing about 10^{11} stars and with a mass of about $10^{12} M_{\odot}$ (Solar masses), our Galaxy, the Milky Way, appears to be a typical bright galaxy. It is a spiral galaxy, with a quasi-spherical central bulge of old stars surrounded by a thin disk of younger stars and an exponential scale length of about 5 kpc (1 pc, defined to be the distance

at which the parallax due to the Earth's orbit is one arcsec, is roughly 3×10^{16} m). The rotation curve of the disk is fairly flat (*i.e.*, rotation velocity independent of radius) at 220 km s^{-1} , implying the existence of a massive halo with $M(< R) \propto R$ which extends out many kpc. See Binney & Tremaine (1987) and references therein for a good review of Milky Way properties. It appears that in terms of all these properties, the Milky Way is typical. In particular spiral disks tend to contain younger stars than the bulges do; rotation curves tend to be flat; and pretty much all bright local galaxies have massive halos which extend beyond 100 kpc (Zaritsky *et al.* 1997). The Milky Way has several small, close companions which are in the process of merging with it; again this appears to be a generic property of bright galaxies (Zaritsky *et al.* 1997). These companions are likely to merge completely with the Milky Way in many 10^8 yr. As mentioned above, the companions suggest the possible importance of the merger of small objects into larger systems in the life histories of galaxies. An important project now underway is the determination of the merger history of the Milky Way in order to put limits on such cosmological models (*e.g.*, Johnston 1997).

Large area, bright, local galaxy redshift surveys are used to measure the local galaxy luminosity function $\phi(L)$ (number density per unit luminosity L). These are heroic efforts usually involving several 10^4 galaxies and very careful selection and photometry taken from photographic sky survey plates. Strangely, the various surveys are in strong disagreement over the characteristic number density ϕ^* in the Schechter (1976) parameterization of the luminosity function

$$\phi(L) = \frac{\phi^*}{L^*} \left(\frac{L}{L^*} \right)^\alpha e^{-L/L^*} \quad (1.1)$$

where L^* is a characteristic luminosity and α parameterizes the faint-end behavior. All groups find the Schechter form with $\alpha = -1$ (called “flat” because in per-logarithmic form $\phi(\log L)$ the luminosity function shows a constant number per log luminosity) to be a good fit. The range of results for the characteristic density is $3 < \phi^* \ll 10 \times 10^8$ per Hubble Volume with $M_B^* + 5 \log h \sim 20$ mag where h is the Hubble constant divided by $100 \text{ km s}^{-1} \text{ Mpc}^{-1}$ and M_B^* is the absolute magnitude

in the B band (see Appendix A) corresponding to the characteristic luminosity L^* (Efsthathiou *et al.* 1988; Loveday *et al.* 1992; Marzke *et al.* 1994a; Lin *et al.* 1996, 1997; Griffiths *et al.* 1997; Ratcliffe *et al.* 1997). For reference, the luminosity of the Milky Way is on the order of L^* .

There are several possible explanations for the discrepancies between the different local survey results for the characteristic density ϕ^* , including the influence of large-scale structure, systematic photometric errors resulting from the use of photographic plates for flux estimates, and differing sensitivity to low-surface-brightness galaxies (Dalcanton in preparation). None of these suggestions are really well-developed, in the sense that none of them can quantitatively explain the survey-to-survey scatter. These issues may be resolved by large-area CCD surveys now in planning, such as the upcoming Sloan Digital Sky Survey.

Strangely, what the local surveys *do* agree upon is the exponent α . All find consistency with $\alpha = -1$ (called a “flat” luminosity function because $\phi(\log L)$ or $\phi(M)$, the number density per unit log luminosity or per unit absolute magnitude, is independent of luminosity at the faint end, $L < L^*$). It is interesting that the flat luminosity function is such a robust observational result because hierarchical clustering theory predicts a very steep (*i.e.*, much more dwarf-dominated) luminosity function with $\alpha = -2$ (Press & Schechter 1974; Kauffmann *et al.* 1993). Those convinced of the *a priori* truth of hierarchical clustering have been forced to believe that light does not democratically trace mass but in fact that low-mass objects form stars very inefficiently or the majority of low-mass objects don’t form stars at all (Kauffmann *et al.* 1993). In either case, the Milky Way ought to be swimming in a swarm of low-mass galaxies not observed in large-area galaxy surveys.

One of the first results of importance in the study of galaxies was that they can be easily classified according to their shapes, or morphological properties, into a one or two-dimensional classification scheme (Sandage 1961). The photometric and other properties of galaxies vary in systematic ways along this Hubble sequence, with “early-type” galaxies (ellipticals) having red colors, old stars, little current star formation, and little specific angular momentum and “late-type” galaxies (spirals) being bluer,

containing apparently younger stars, and showing strong rotation (*e.g.*, Kennicutt *et al.* 1994; Roberts & Haynes 1994). Galaxy morphology appears to be related to environment, with denser environments showing a higher proportion of early-type galaxies (Dressler 1980). Another type of environment-dependence appears in the study of compact groups where the members of each compact group tend to all have the same morphology, although that morphology changes from group to group (Hickson 1997). These results demonstrate that morphological classification is not mere philately but in fact almost certainly has physical importance. The fractions of galaxies in each morphological type vary strongly with luminosity, with more elliptical galaxies at the bright end, and more irregulars at the faint (Sandage *et al.* 1985; Marzke *et al.* 1994b). The same result can be found by exploiting the morphology-color relation; blue galaxies have a steeper (*i.e.*, more dwarf-rich) luminosity function than red (Marzke & da Costa 1997); or the morphology-spectrum relation; apparently star-forming galaxies have a steeper luminosity function than quiescent (Lin *et al.* 1996; Heyl *et al.* 1997).

In the nearby Universe, galaxies appear to live in groups, rarely isolated. The Milky Way is in the Local Group, which appears to be a dynamically young, perhaps still collapsing structure dominated by the Milky Way and Andromeda. Beyond the Local Group, significantly more than half of the galaxies in the low-redshift Universe seem to be in groups, depending upon exactly how one defines a group. These ubiquitous groups are likely to contain a significant fraction of the mass in the Universe (Mulchaey *et al.* 1996).

1.3 Galaxy evolution

This thesis is about galaxy evolution, a subject which aims to answer the following questions (among others): When were the first galaxies born and what did they look like at that stage? How do birth rates and birth environments relate to galaxy masses, sizes and luminosities? What is the typical merging or interaction history? Are the present-day parameters of local galaxies set by their initial conditions or by

environmental effects during their evolution (and is there a difference between these scenarios)? Are galaxies steady and slowly evolving in their properties or do they undergo vast, rapid changes?

The uniform, old stellar populations observed in elliptical galaxies have been used to argue that ellipticals must form in giant, brief starbursts at high redshift. Observations of the fundamental plane—a three-way correlation between galaxy radius, luminosity and velocity dispersion (or mass) discovered in the local universe (Faber & Jackson 1980; Djorgovski & Davis 1987)—at high redshift suggest that the photometric evolution of ellipticals is consistent with no evolution save the fading of the old stellar populations they contain (van Dokkum & Franx, 1996). Similarly, studies of the Tully–Fisher (1977) relation—a correlation between luminosity and circular velocity (or mass)—for disk or spiral galaxies at high redshift have also shown little or no evolution in their statistical properties (Vogt *et al.* 1996a, 1996b). Also, evolution in disk surface brightnesses appears to be consistent with that expected from their present-day stellar populations and star formation rates (Schade *et al.* 1995, 1996). Basically, large bright galaxies do not seem to be evolving dramatically to redshifts $z \approx 1$.

In models of hierarchical clustering, on the other hand, galaxies merge frequently. Massive galaxies are built up by successive mergers of less massive systems (Press & Schechter 1974). Furthermore, a natural explanation of the excess faint galaxy counts is that there were many more intrinsically faint galaxies in the past which by the present day have merged into the smaller number of larger, brighter galaxies we observe locally (*e.g.*, Pascarelle *et al.* 1996). Hierarchical clustering makes predictions for the numbers of close pairs as a function of redshift; observational results are somewhat contradictory, but they generally support a picture in which there is significant merging to redshift $z \approx 1$, with the rate increasing with redshift (Carlberg *et al.* 1994; Griffiths *et al.* 1994b; Yee & Ellingson 1995; Woods *et al.* 1995).

Are the merger rate estimates—which suggest that galaxies are merging and thus evolving strongly even at $z < 1$ —inconsistent with the passive evolution results—which suggest that little dynamical evolution is going on? No. After all the first

says that *individual objects* may be evolving strongly while the latter says that the properties of *broad classes* of objects do not evolve rapidly. This fits in with a recent result that although the fundamental plane appears very stable, the number density of ellipticals appears to be increasing with time (Kauffmann *et al.* 1996). This brings up an important question for galaxy evolution studies: How do we distinguish evolution in the statistical properties of samples from the evolution of individual objects? It is certainly important not to over-interpret evolutionary results.

If the picture currently developing is correct, *i.e.*, that the statistical properties of the classes of bright spirals and ellipticals are not changing rapidly while the objects in the classes are forming recently or undergoing significant merging, then the theoretical challenge is to explain how such tight regularities as the fundamental plane and Tully-Fisher relations can apply to groups of heterogeneously formed, dynamically young objects. Presumably an important hint is that these tight regularities only apply to objects in a single morphological class, and, as mentioned above, there are tremendous correlations between morphological class (Sandage 1961) and internal stellar populations (Kennicutt *et al.* 1994; Roberts & Haynes 1994), internal dynamics (Roberts & Haynes 1994), and environment (Dressler 1980).

As for dwarf (low-luminosity) galaxies, an important recent discovery is that the broadband colors, Balmer decrements, and [OII] linewidths all indicate that the intrinsically faintest galaxies in the Universe form latest (Cowie *et al.* 1996; Heyl *et al.* 1996). This contradicts the most naive interpretation of hierarchical clustering (Press & Schechter 1974). Strangely, it appears that star formation rates in local galaxies are not strongly correlated with total luminosities (Soifer *et al.* 1987; Gallego *et al.* 1995); in other words we are concluding that the dwarf galaxies are younger simply because there is some luminosity-independent average star formation rate which accounts, on average, for a larger fraction of the total light in intrinsically fainter systems. This might seem like an explanation for the fainter–younger effect, but in fact it is difficult to imagine what kind of mechanism could set the total star formation rate in a galaxy in a way which is insensitive to the total galaxy size. On the other hand, selection effects could be involved, since low-mass objects will only be detectable in

flux-limited surveys when their star formation rates are high, while the larger galaxies will be observable whatever their star formation rates. In addition, star formation can blow remnant gas out of small potential wells (Babul & Rees 1992), perhaps preventing low-mass galaxies from having mid-range star formation rates for any significant length of time; *i.e.*, they are either “full-on” or “shut off.” Interestingly, if it is true that fainter galaxy counts are produced, by-and-large, by intrinsically fainter objects, then the fact that to $B \approx 26$ mag apparently fainter galaxies are bluer (Koo & Kron 1992; Smail *et al.* 1995; Hogg *et al.* 1997a) would be naturally interpreted as evidence for the relative youth of intrinsically fainter galaxies, even at moderate redshift.

1.4 Cosmogony

Astrophysicists are interested in fundamental physical properties of the Universe, not just what can be easily seen through a telescope, of course. For example, much of the study of galaxies to date has assumed that mass and light are at least closely related. Locally this seems true, since the Milky Way and Andromeda and the Local Group all seem to be massive and the dynamics are at least consistent with a good match between mass and light. Furthermore, it is known that there is a connection between mass and light at the massive end of the distribution, even out to redshifts around unity, because the great majority of multiply imaging gravitational lens systems show a luminous lensing object (*e.g.*, Keeton & Kochanek 1996). There must also be a connection at the bright end, since the high-redshift fundamental plane and Tully–Fisher studies mentioned above do find the expected mass associated with survey objects (van Dokkum & Franx 1996; Vogt *et al.* 1996a, 1996b). However, it is easy to imagine scenarios in which the connection between mass and light is not strong, especially for smaller, less massive systems, for which it is difficult to measure masses. It is well known that star formation is closely related to galaxy–galaxy interactions and it appears that such interactions may even give birth to isolated dwarf galaxies which are flung out in tidal arms (Hunsberger *et al.* 1996). Perhaps there is an alternate scenario in which galaxy formation is more tied to shocking or shearing of

gas than mass overdensity *per se*. These questions are especially important in light of the very strong velocity-space clustering found for high-redshift galaxies out to $z \approx 1$ (Cohen *et al.* 1996a, 1996b; Koo *et al.* 1996) and, it appears, out to $z \approx 3$ (Steidel *et al.* 1997).

Another matter of importance is the star formation rate or metal production rate of the Universe. This can be estimated in a number of ways, with the changing metallicity of intergalactic gas (Pei & Fall 1995), the blue or ultraviolet luminosity density of the Universe (Lilly *et al.* 1996; Madau *et al.* 1996) and the emission line luminosities of galaxies (Gallego *et al.* 1995; Chapter 3). So far the results suggest that the star formation rate of the Universe was much higher at redshifts around unity than it is locally. Unfortunately, all these methods have to assume that star formation in the high-redshift universe is similar to that locally, although in principle this can be tested with detailed spectral analyses. They also mostly assume that the bulk of star formation in the Universe is not enshrouded in dust, although there are some hints that this is not the case (*e.g.*, Omont *et al.* 1996).

1.5 Cosmography

Telescopes and their instruments have improved dramatically since the construction of the 200-inch Hale Telescope on Palomar mountain. Over the same period, however, interest in performing the “classical cosmological tests” (*e.g.*, Sandage 1988), for which the Hale Telescope was ostensibly built, has waned. Cosmologists have become aware that in most of these tests, *e.g.*, the number counts of galaxies described above, poorly understood evolutionary changes in the populations under study is more significant than variations introduced by adjusting the cosmological world model (Koo & Kron 1992). The response has been to “give up,” re-casting the tests entirely as diagnostics of galaxy and quasar evolution. In addition, in the last few years, theoretical work on the cosmic background radiation (CBR) has shown that all of the cosmological parameters ought to be encoded in the details of its small-scale power spectrum. Several space-based missions under development, including the MAP and

Planck satellites, if successful, will measure the CBR spectrum with sufficient detail to constrain all the cosmological parameters to within a few percent. To a surprisingly large extent, observers have decided to rely on these CBR missions to provide the cosmological parameters, which will then be input to evolutionary studies (*e.g.*, Efstathiou, 1996).

It is my strong feeling that this is a mistake. The CBR is emitted at $z \approx 1000$, so even if the spectrum of CBR fluctuations exactly matches the predictions of some standard world model, it is an unprecedented (and almost certainly unjustified) reliance on theory to assume that it completely determines all cosmography at $z = 0$. It is tantamount to assuming that all cosmological theory, very little of which has been stringently tested, is correct! Furthermore there is the possibility that any number of confusing or obscuring foreground source populations might degrade or contaminate the signal and make it disagree with the predictions, perhaps even in subtle ways. The CBR missions are very important observational projects which must be executed, especially since they have the unique capability to apply a very strong test to the standard cosmological model, in a field where the data is usually far ahead of the theory. On the other hand, it would be irresponsible for observers to leave the theoretical connection between the surface of last scattering and the present-day geometry of the Universe untested. Success in the classical tests is as important a scientific goal as it ever was. More so because not only will they determine the local geometry, they will also test the connection between the geometry and the CBR spectrum.

What we have learned since the construction of the Hale Telescope is not that the classical tests are useless for cosmology; just that they are very very difficult. This is not a reason to give them up. There are several “neo-classical” cosmological tests (terminology of Peebles 1993), using galaxies as probes of geometry, which might be possible over the same timescales as the construction and flight of the new CBR missions. One of the motivations of this thesis is to help improve the understanding of galaxy evolution to the point that galaxies can be used in these neo-classical cosmological tests. Of course the tests are really a goal for the distant future, once

the questions raised in this introductory Chapter have all been—at least to some extent—answered.

1.6 This thesis

This thesis aims to obtain some results on the evolution of galaxies from a spectroscopic survey underway at Caltech. The spectroscopic sample consists of several hundred galaxies in the Hubble Deep Field and a surrounding patch of sky. The particular results presented here are mainly on the luminosity function of galaxies, in the [O II] emission line and in the broad B bandpass. The following four Chapters are almost entirely observational; attempts to construct measures of galaxy evolution directly from the data. Interpretation is postponed until Chapter 6.

References

- Abraham R. G., Tanvir N. R., Santiago B. X., Ellis R. S., Glazebrook K. & van den Bergh S., 1996, Galaxy morphology to $I = 25$ mag in the Hubble Deep Field, MNRAS 279 L47
- Babul A. & Rees M. J., 1992, On dwarf elliptic galaxies and the faint blue counts, MNRAS 255 346
- Babul A. & Ferguson H. C., 1996, Faint blue galaxies and the epoch of dwarf galaxy formation, ApJ 458 100
- Bahcall J. N., Kirhakos S., Saxe D. H. & Schneider D. P., 1996, Hubble Space Telescope images of a sample of twenty nearby luminous quasars, ApJ 479 642
- Binney J. & Tremaine S., 1987, *Galactic Dynamics*, Princeton University Press, Princeton
- Broadhurst T. J., Ellis R. S. & Shanks T., 1988, The Durham Anglo-Australian Telescope faint galaxy redshift survey, MNRAS 235 827
- Carlberg R. G., Pritchet C. J. & Infante L., 1994, A survey of faint galaxy pairs, ApJ 435 540
- Cohen J. G., Hogg D. W., Pahre M. A. & Blandford R., 1996a, Strong redshift clustering of distant galaxies, ApJ 462 L9
- Cohen J. G., Cowie L. L., Hogg D. W., Songaila A., Blandford R., Hu E. M. & Shopbell P., 1996b, Redshift clustering in the Hubble Deep Field, ApJ 471 L5
- Colley W. N., Gnedin O. Y., Ostriker J. P. & Rhoads J. E., 1997, Dynamics of “small galaxies” in the Hubble Deep Field, ApJ 488 579

- Cowie L. L., Songaila A., Hu E. M. & Cohen J. G., 1996, New insight on galaxy formation and evolution from Keck spectroscopy of the Hawaii Deep Fields, *AJ* 112 839
- Djorgovski S. & Davis M., 1987, Fundamental properties of elliptical galaxies, *ApJ* 313 59
- Djorgovski S. *et al.*; 1995, Deep galaxy counts in the *K* band with the Keck Telescope, *ApJ* 438 L13
- Dressler A., 1980, Galaxy morphology in rich clusters: Implications for the formation and evolution of galaxies, *ApJ* 236 351
- Driver S. P., Windhorst R. A., Griffiths R. E., 1995, The contribution of late-type irregulars to the faint galaxy counts from Hubble Space Telescope Medium Deep Survey images, *ApJ* 453 48
- Driver S. P. & Phillips S., 1996, *ApJ*, submitted
- Dunlop J., Peacock J., Spinrad H., Dey A., Jimenez R., Stern D. & Windhorst R., 1996, A 3.5 Gyr old galaxy at redshift 1.55, *Nature* 381 581
- Eales S., 1993, Direct construction of the galaxy luminosity function as a function of redshift, *ApJ* 404 51
- Efstathiou G., Ellis R. S. & Peterson B. A., 1988, Analysis of a complete galaxy redshift survey II: The field-galaxy luminosity function, *MNRAS* 232 431
- Efstathiou G., 1996, in *HST and the High Redshift Universe*, eds. Tanvir N. R., Aragón-Salamanca A. & Wall J. V., Cambridge University Press, Cambridge
- Ellis R. S., Colless M., Broadhurst T., Heyl J. & Glazebrook K., 1996, Autofib Redshift Survey I: Evolution of the galaxy luminosity function, *MNRAS* 280 235
- Faber S. M. & Jackson R. E., 1976, Velocity dispersions and mass-to-light ratios for elliptical galaxies, *ApJ* 204 668
- Fukugita M., Yamashita K., Takahara F. & Yoshii, Y., 1990, Test for the cosmological constant with the number count of faint galaxies, *ApJ* 361 L1
- Gallego J., Zamorano J., Aragón-Salamanca A. & Rego M., 1995, The current star formation rate of the local Universe, *ApJ* 455 L1
- Gardner J. P., Cowie L. L. & Wainscoat R. J., 1993, Galaxy number counts from $K = 10$ to $K = 23$, *ApJ* 415 L9
- Gardner J. P., Sharples R. M., Frenk C. S., Carrasco B. E., 1997, A wide-field K-band survey: The luminosity function of galaxies, *ApJ* 480 L99
- Giavalisco M., Livio M., Bohlin R. C., Macchetto F. D. & Stecher T. P., 1996, On the morphology of the HST faint galaxies, *AJ* 112 369
- Glazebrook K., Ellis R., Santiago B. & Griffiths R., 1995a, The morphological identification of the rapidly evolving population of faint galaxies, *MNRAS* 275 L19
- Glazebrook K., Ellis R., Colless M., Broadhurst T., Allington-Smith J. & Tanvir N., 1995b, A faint galaxy redshift survey to $B = 24$, *MNRAS* 273 157
- Griffiths R. E. *et al.*, 1994a, The morphology of faint galaxies in medium deep survey images using WFPC2, *ApJ* 435 L19
- Griffiths R. E. *et al.*, 1994b, The Hubble Space Telescope Medium Deep Survey with the Wide Field and Planetary Camera I: Methodology and results on the field near 3C 273, *ApJ* 437 67

- Gronwall C. & Koo D. C., 1995, Resurrection of traditional luminosity evolution models to explain faint field galaxies, *ApJ* 440 L1
- Guhathakurta P., Tyson J. A. & Majewski S. R., 1990, A redshift limit for the faint blue galaxy population from deep *U*-band imaging, *ApJ* 357 L9
- Hall P. & Mackay C. D., 1984, Faint galaxy number magnitude counts at high galactic latitude I, *MNRAS* 210 979
- Heyl J., Colless M., Ellis R. S. & Broadhurst T., 1997, Autofib Redshift Survey II: The evolution of the galaxy luminosity function by spectral type, *MNRAS* 285 613
- Hickson P., Compact groups of galaxies, *ARA&A* 35 357
- Hogg D. W., Blandford R., Kundić T., Fassnacht C. D. & Malhotra S., 1996a, A candidate gravitational lens in the Hubble Deep Field, *ApJ* 467 L73
- Hogg D. W., Neugebauer G., Armus L., Matthews K., Pahre M. A., Soifer B. T. & Weinberger A. J., 1997a, Near infrared imaging of the Hubble Deep Field with the Keck Telescope, *AJ* 113 474
- Hogg D. W., Pahre M. A., McCarthy J. K., Cohen J. G., Blandford R., Smail I. & Soifer B. T., 1997b, Counts and colors of faint galaxies in the U and R bands, *MNRAS* 288 404
- Hunsberger S. D., Charlton J. C. & Zaritsky D., 1996, The formation of dwarf galaxies in tidal debris: A study of the compact group environment, *ApJ* 462 50
- Ibata R. A., Wyse R. F. G., Gilmore G., Irwin M. J. & Suntzeff N. B., The kinematics, orbit, and survival of the Sagittarius dwarf spheroidal galaxy, *AJ* 113 634
- Im M., Griffiths R. E. & Ratnatunga K. U., 1996, A measurement of the cosmological constant using elliptical galaxies as strong gravitational lenses, *ApJ* 475 457
- Johnston K., 1997, A prescription for building the Milky Way's halo from disrupted satellites, *ApJ* in press
- Kauffmann G., White S. D. M. & Guiderdoni B., 1993, The formation and evolution of galaxies within merging dark matter haloes, *MNRAS* 264 201
- Kauffmann G., Charlot S. & White S. D. M., 1996, Detection of strong evolution in the population of early-type galaxies, *MNRAS* submitted
- Keeton C. R. II & Kochanek C. S., 1996, Summary of data on secure multiply imaged systems, *Astrophysical Applications of Gravitational Lensing*, eds. Kochanek C. S. & Hewitt J. N., Kluwer, Dordrecht
- Kennicutt R. C. Jr., Tamblyn P. & Congdon C. E., 1994, Past and future star formation in disk galaxies, *ApJ* 435 22
- Kochanek C. S., 1996, Is there a cosmological constant?, *ApJ* 466 638
- Koo D. C. & Kron R. G., 1992, Evidence for evolution in faint field galaxy samples, *ARA&A* 30 613
- Koo D. C., Gronwall C. & Bruzual G. A., 1993, Counter-evolution of faint field galaxies, *ApJ* 415 L21
- Koo D. C. *et al.*; 1996, Redshift $z \approx 1$ field galaxies observed with the Keck Telescope and the Hubble Space Telescope, *ApJ* 469 535
- Lilly S. J., Cowie L. L. & Gardner J. P., 1991, A deep imaging and spectroscopic survey of faint galaxies, *ApJ* 369 79

- Lilly S. J., Tresse L., Hammer F., Crampton D. & Le Fevre O., 1995, The Canada-France redshift survey VI: Evolution of the galaxy luminosity function to $z \sim 1$, *ApJ* 455 108
- Lilly S. J., Le Fèvre O., Hammer F. & Crampton D., 1996, The Canada-France Redshift Survey: The luminosity density and star formation history of the Universe to $z \sim 1$, *ApJ* 460 L1
- Lin H., Kirshner R. P., Shectman S. A., Landy S. D., Oemler A., Tucker D. L. & Schechter P. L., 1996, The luminosity function of galaxies in the Las Campanas Redshift Survey, *ApJ* 464 60
- Lin H., Yee H. K. C., Carlberg R. G. & Ellingson E. E., 1997, The luminosity function of field galaxies in the CNOC1 redshift survey, *ApJ* 475 494
- Loveday J., Peterson B. A., Efstathiou G. & Maddox S. J., 1992, The Stromlo-APM Redshift Survey I: the luminosity function and space density of galaxies, *ApJ* 390 338
- Madau P., Ferguson H. C., Dickinson M. E., Giavalisco M., Steidel C. C. & Fruchter A., High redshift galaxies in the Hubble Deep Field: Color selection and star formation history to $z = 4$, 1996, *MNRAS*, in press
- Maoz D. & Rix H.-W., 1993, Early-type galaxies, dark halos, and gravitational lensing statistics, *ApJ* 416 425
- Marzke R. O., Huchra J. P. & Geller M. J., 1994a, The luminosity function of the CfA redshift survey, *ApJ* 428 43
- Marzke R. O., Geller M. J., Huchra J. P. & Corwin H. G., 1994b, The luminosity function for different morphological types in the CfA redshift survey, *AJ* 108 437
- Marzke R. O. & da Costa L. N., 1997, The galaxy luminosity function at $z \leq 0.05$: Dependence on color, *AJ* 113 185
- McGaugh S. S., 1994, A possible local counterpart to the excess population of faint blue galaxies, *Nature* 367 538
- McGaugh S. S., Bothun G. D. & Schombert J. M., 1995, Galaxy selection and the surface brightness distribution, *AJ* 110 573
- Metcalfe N., Shanks T., Fong R. & Roche N., 1995, Galaxy number counts III: Deep CCD observations to $B = 27.5$ mag, *MNRAS* 273 257
- Metcalfe N., Shanks T., Campos A., Fong R. & Gardner J. P., 1996, Galaxy formation at high redshifts, *Nature* 383 236
- Mobasher B., Sharples R. M. & Ellis R. S., 1993, A complete galaxy redshift survey—V. Infrared luminosity functions for field galaxies, *MNRAS* 263 560
- Mulchaey J. S., Davis D. S., Mushotzky R. F. & Burstein D., 1996, The intragroup medium in poor groups of galaxies, *ApJ* 456 80
- Odewahn S. C., Windhorst R. A., Driver S. P. & Keel W. C., 1996, Automated morphological classification in deep HST UVBI fields: Rapidly and passively evolving faint galaxy populations, *ApJ* 472 L130
- Omont A., Petitjean P., Guilloteau S., McMahon R. G., Solomon P. M. & Pecontal E., 1996, Molecular gas and dust around a radio-quiet quasar at redshift 4.69, *Nature* 382 428

- Pascarelle S. M., Windhorst R. A., Keel W. C. & Odewahn S. C., 1996, Sub-galactic clumps at a redshift of 2.39 and implications for galaxy formation, *Nature* 383 45
- Peebles P. J. E., 1993, *Principles of Physical Cosmology*, Princeton University, Princeton
- Pei Y. C. & Fall S. M., 1995, Cosmic chemical evolution, *ApJ* 454 69
- Press W. H. & Schechter P., 1974, Formation of galaxies and clusters of galaxies by self-similar gravitational condensation, *ApJ* 187 425
- Ratcliffe A., Shanks T., Parker Q. A. & Fong R., 1997, The Durham/UKST Galaxy Redshift Survey II: The field galaxy luminosity function, *MNRAS* in press
- Roberts M. S. & Haynes M. P., 1994, Physical parameters along the Hubble sequence, *ARA&A* 32 115
- Rocca-Volmerange B. & Guiderdoni B., 1990, Merging-driven evolution of high-redshift galaxies in a universe with $\Omega_0 = 1$, *MNRAS* 247 166
- Sandage A., 1961, *The Hubble Atlas of Galaxies*, Carnegie Institute of Washington, Washington
- Sandage A., Binggeli B. & Tammann G. A., 1985, Studies of the Virgo Cluster V: Luminosity functions of Virgo Cluster galaxies, *AJ* 90 1759
- Sandage A., 1988, Observational tests of world models, *ARA&A* 26 561
- Schade D., Lilly S. J., Crampton D., Hammer F., Le Fèvre O. & Tresse L., 1995, The Canada-France Redshift Survey IX: HST imaging of high-redshift field galaxies, *ApJ* 455 L1
- Schade D. J., Lilly S. J., Le Fèvre O., Hammer F., Crampton D., 1996, The Canada-France Redshift Survey XI: Morphology of high redshift field galaxies from high-resolution ground-based imaging, *ApJ* 464 79
- Schechter P., 1976, An analytic expression for the luminosity function for galaxies, *ApJ* 203 297
- Smail I., Hogg D. W., Yan L. & Cohen J. G., 1995, Deep optical galaxy counts with the Keck Telescope, *ApJ* 449 L105
- Soifer B. T., Sanders D. B., Madore B. F., Neugebauer G., Danielson G. E., Elias J. H., Lonsdale C. J. & Rice W. L., 1987, The IRAS bright galaxy sample II: The sample and luminosity function, *ApJ* 320 238
- Soifer B. T. *et al.*; 1994, Deep imaging of the field of the $z = 4.9$ quasar PC 1247+3406 and faint galaxy counts in the K band with the Keck telescope, *ApJ* 420 L1
- Steidel C. C. & Hamilton D., 1993, Deep imaging of high redshift QSO fields below the Lyman limit II: Number counts and colors of field galaxies, *AJ* 105 2017
- Steidel C. C., Giavalisco M., Pettini M., Dickinson M. & Adelberger K. L., 1996a, Spectroscopic Confirmation of a Population of Normal Star-forming Galaxies at Redshifts $z > 3$, *ApJ* 462 L17
- Steidel C. C., Giavalisco M., Dickinson M. & Adelberger K. L., 1996b, Spectroscopy of Lyman break galaxies in the Hubble Deep Field, *AJ* 112 352
- Steidel C. C., Adelberger K. L., Dickinson M., Giavalisco M., Pettini M. & Kellogg M., 1997, A large structure of galaxies at redshift $z \sim 3$ and its cosmological implications, *ApJ* in press

- Treyer M. A. & Silk J., 1994, The faint end of the galaxy luminosity function, *ApJ* 436 L143
- Tully R. B. & Fisher J. R., 1977, A new method of determining distances to galaxies, *A&A* 54 661
- Turner E. L., 1990, Gravitational lensing limits on the cosmological constant in a flat universe, *ApJ* 365 L43
- Tyson J. A., 1988, Deep CCD survey: Galaxy luminosity and color evolution, *AJ* 96 1
- van Dokkum P. G. & Franx M., 1996, The fundamental plane in CL 0024 at $z = 0.4$: Implications for the evolution of the mass-to-light ratio, *MNRAS* 281 985
- Vogt N. P., Forbes D. A., Phillips A. C., Gronwall C., Faber S. M., Illingworth G. D. & Koo D. C., 1996a, Optical rotation curves of distant field galaxies I: Keck results at redshifts to $z \sim 1$, *ApJ* 465 L15
- Vogt N. P. *et al.*, 1996b, Optical rotation curves of distant field galaxies II: an extension to lower luminosity systems, in preparation
- Williams R. E. *et al.*, 1996, The Hubble Deep Field: Observations, data reduction and galaxy photometry, *AJ* 112 1335
- Woods D., Fahlman G. G. & Richer H. B., 1995, Counting pairs of faint galaxies, *ApJ* 454 32
- Yee H. K. C. & Ellingson E., 1995, Statistics of close galaxy pairs from a faint-galaxy redshift survey, *ApJ* 445 37
- Yoshii Y. & Sato K., 1992, Constraints on the universe with a decaying cosmological constant from a number count of faint galaxies, *ApJ* 387 L7
- Zaritsky D., Smith R., Frenk C. & White S. D. M., 1997, More satellites of spiral galaxies, *ApJ* 478 39

Chapter 2 Source detection and photometry in the Hubble Deep Field survey region

2.1 Introduction

This Chapter describes the detection and photometry of catalogs of sources in a region of the sky centered on the Hubble Deep Field (HDF, Williams *et al.* 1996) for spectroscopic study as part of the faint field galaxy redshift surveys underway at Caltech. This totally observational project is the starting point for the spectroscopic results which follow in the subsequent Chapters.

The HDF was chosen to be at high Galactic latitude, at low extinction, and free of bright or unusual sources; it has quickly become a “standard field” for the study of very faint extragalactic sources. The Hubble Space Telescope (HST) images of the HDF are the deepest optical images of the sky ever taken, reaching source densities of roughly 10^6 deg^{-2} . Unfortunately, the HST images are very small, covering only about 5 arcmin^2 , so they are poorly matched to the 15 arcmin^2 spectroscopic field of the Low Resolution Imaging Spectrograph (LRIS, Oke *et al.* 1996) instrument on the Keck Telescope, the instrument with which the Caltech faint galaxy redshift surveys are being performed. For this reason the spectroscopic surveys in the HDF are performed in a larger region of the sky surrounding the HST image, with sources selected with the ground-based data presented here.

2.2 Data

For visual data U_n , G and \mathcal{R} images taken with the 200-inch Hale Telescope at the Palomar Observatory were used. The images are 8.6×8.7 arcmin² and centered on the HST image of the HDF (Williams *et al.* 1996). The images were taken in order to identify candidate $z > 3$ galaxies; details of the observations, calibration, and reduction of these images are described in Steidel *et al.* (in preparation).

To maintain a consistent flux or magnitude system, the U_n , G and \mathcal{R} images are calibrated by comparison with the extremely deep HST images of the HDF. The acquisition, reduction and calibration of these images are described in Williams *et al.* (1996).

For near-infrared data, an 8-arcmin diameter circular region centered on the HDF was imaged on 1997 March 19–21 using a K_s filter with a near-infrared camera (Jarrett *et al.* 1994) mounted at the prime focus of the 200-inch Hale Telescope. The instrument reimages the focal plane at 1:1 onto a NICMOS–3 256×256 pixel² HgCdTe array (produced by Rockwell), producing a 0.494 arcsec projected pixel size and a 2.1 arcmin instantaneous field of view. Fourteen separate pointings, offset by 2 arcmin, were required in order to mosaic the entire circular field; each of these subfields was imaged once per night. For each subfield each night, 45 separate frames were taken; each frame consisted of six exposures of three seconds each, coadded in the electronics before writing to disk. The telescope was dithered by 5–15 arcsec between frames. As a result, each subfield was exposed for 810 s each night, or 2430 s for the three nights. The seeing was ~ 1.0 arcsec for most of the three nights. The first two nights were judged photometric, and were calibrated using the faint Solar-type standard stars of Persson (private communication).

The K_s -band data were reduced by the method of Pahre *et al.* (1997). Each subfield was reduced separately for each night. The third night's data were rescaled in order to account for the thin cirrus; the scaling factors were determined from a fit to a large number of sources. The subfields were then registered by aligning the objects in common with adjacent subfields in the overlap region. Individual pixels in a given

field were weighted by the number of contributing to that pixel. A “sky” image was created by median-filtering the mosaic with a wide filter and sigma-clipping. This sky image was subtracted from the mosaic in order to remove any subfield-to-subfield variations in the sky brightness of the final mosaic. The final K_s -band mosaic is displayed in Figure 2.1.

Table 2.1 gives the properties of the final, stacked images.

2.3 Source detection

Sources are detected in all four images independently to construct four catalogs, hereafter “ U_n -selected,” “ G -selected,” “ \mathcal{R} -selected” and “ K_s -selected.” All catalogs are created with the SExtractor source detection and photometry package (Bertin & Arnouts 1996). The detection algorithm is as follows: Images are smoothed with a Gaussian filter which has roughly the same FWHM as the seeing (1.13 arcsec for the visual images and 1.5 arcsec for the K_s -band image). Sources in the smoothed image with central-pixel surface brightness above a certain limit are added to the catalog. If a source has multiple peaks within its $1.2\text{-}\sigma$ isophotal area on the image (where σ is the pixel-to-pixel root-mean-square fluctuation in the sky brightness), each peak is split into a separate catalog source if it contains at least one percent of the original source’s isophotal flux.

Several sources which, by eye, appear that they ought to be split off of brighter nearby objects but were not, and several very faint sources which appear (with the aid of the deeper HST images, see below) to exist but which were missed by the detection algorithm, were added to the \mathcal{R} -selected catalog to make it as inclusive as possible for spectroscopy.

2.4 Calibration with HST imaging

In order to maintain a consistent set of flux measurements, the U_n , G and \mathcal{R} -band images are calibrated by comparison with the HST images of the HDF (Williams *et*

al. 1996).

The absolute calibrations and effective wavelengths for the HST and ground-based filters are used to compute the following transformation equations under the assumption that the sources have power-law spectral energy distributions (see Appendix A for the method):

$$U_n = 0.53 F300W + 0.47 F450W - 0.29 \quad (2.1)$$

$$G = 0.82 F450W + 0.18 F606W - 0.07 \quad (2.2)$$

$$\mathcal{R} = 0.46 F606W + 0.54 F814W - 0.02 \quad (2.3)$$

where $F300W$, $F450W$, $F606W$ and $F814W$ are Vega-relative magnitudes in the HST bandpasses of the same name.

The “Version 2” HST HDF images (Williams *et al.* 1996) are transformed onto the U_n , G and \mathcal{R} image coordinate system and all seven images are Gaussian-smoothed to have the same effective seeing. Aperture magnitudes are measured for the \mathcal{R} -selected sample through matched, 2-arcsec diameter apertures. For calibration, the Vega-relative magnitude zeropoints are used (not the “AB” zeropoints used by Williams *et al.* 1996). The measured U_n , G and \mathcal{R} -band magnitudes are zeropointed so the comparison with transformed HST magnitudes in Figure 2.2 shows the best possible agreement. This HST-relative calibration ought to be good to roughly 5 percent.

2.5 Photometry

All catalog sources are photometered two ways: Isophotal magnitudes are measured down to the $2\text{-}\sigma$ isophote (where σ is the pixel-to-pixel root-mean-square fluctuation in the sky brightness). Aperture magnitudes are measured through apertures of diameter 1.7 arcsec for the visual images and 2.0 arcsec for the K_s -band image. To the aperture magnitudes corrections are added to account for flux outside the aperture. The aperture corrections are -0.13 , -0.10 , -0.10 and -0.12 mag for the U_n , G , \mathcal{R} and K_s images respectively, computed to correct aperture magnitudes to

total magnitudes for point sources. Although faint galaxies are not point sources, these corrections are used because in these ground-based images there is almost no detectable difference between a faint galaxy and star at the faintest levels. Each source in the catalogs is assigned a “total magnitude” which is the brighter of the isophotal and corrected-aperture magnitudes. In practice this is the isophotal magnitude for all but a fraction of the sources in the last magnitude bin.

2.6 Color measurement

To measure fair colors, the visual images are smoothed with Gaussians to the same effective seeing as the K_s -band image. A catalog of over 500 objects common to the visual and K_s -band images are used to derive the fourth-order polynomial transformation mapping the visual images onto the K_s -band image and vice versa (with NOAO/IRAF tasks “geomap” and “geotran”). Colors are measured through matched apertures of diameter 2 arcsec. For the U_n , G and \mathcal{R} -selected catalogs colors are measured in the smoothed visual image and the K_s -band image transformed onto the visual coordinates. For the K_s -selected catalog, colors are measured in the smoothed visual images transformed onto the K_s -band image coordinates and the K_s -band image.

The numbers of sources and the color distributions for the four catalogs are shown in Figures 2.3 through 2.6.

2.7 Completeness

It appears from Figures 2.3 through 2.6 that the catalogs are complete to roughly $U_n = 25$, $G = 26$, $\mathcal{R} = 25.5$ and $K_s = 20$ mag. No completeness simulations have been performed because the primary purpose of this study is to construct catalogs for spectroscopy, not to measure ultra-deep number counts. For the latter study, better data exist and have been analyzed.

Although a few objects have had redshifts measured with the LRIS instrument on

the Keck Telescope as faint as $R \approx 26$ mag (*e.g.*, Djorgovski *et al.* in preparation), the practical limit of a large, complete, magnitude-limited survey is around $R = 24$ mag, or $K = 20$ mag, so the imaging data are well matched to the capabilities of the spectrograph.

2.8 Discussion

The results of this observational Chapter are entirely contained in Figures 2.3 through 2.6. However, they can be compared with the results of other authors. When divided by the solid angle of the 8.6×8.7 arcmin² field, the integrated number of sources is 1.3×10^5 deg⁻² to $\mathcal{R} = 25.0$ mag. This is consistent with the number counts from similar studies (*e.g.*, Hogg *et al.* 1997b). The color distributions are also consistent with previous studies, in mean and scatter (Hogg *et al.* 1997a, 1997b; Pahre *et al.* 1997).

Number-flux relations of the power-law form $d \log N/dm = Q$, where Q is a constant, are fit to the U_n , G and \mathcal{R} -selected catalogs over the 4-magnitude range terminating at the completeness limits given in Section 2.7. In the K_s -selected catalog the fit is only over $18 < K < 20$ mag because many studies have shown that the slope changes significantly at $K \approx 18$ mag (*e.g.*, Djorgovski *et al.* 1995). The resulting faint-end slopes are $Q = 0.42, 0.33, 0.27$ and 0.31 for the U_n , G , \mathcal{R} and K_s counts respectively. These slopes are consistent with those found in previous studies (Djorgovski *et al.* 1995; Metcalfe *et al.* 1995; Hogg *et al.* 1997b; Pahre *et al.* 1997).

Although all these observations are consistent with previous observational studies, the bulk of the faint sources are significantly bluer than normal, bright galaxies would be if there were no evolution in galaxy spectra. For example, a non-evolving spiral galaxy would have $\mathcal{R} - K_s \approx 3$ mag at redshift $z = 0.6$, and the bluest local galaxies would have $\mathcal{R} - K_s \approx 2.5$ mag (Neugebauer private communication), but in the samples presented here, where the median redshift is roughly 0.6 (Chapter 5), there are many galaxies with $\mathcal{R} - K_s < 2$ mag. This discrepancy has many possible explanations but even taken alone it is strong evidence that galaxies are evolving.

Acknowledgements

Thanks go to Gerry Neugebauer and Mike Pahre for taking, reducing, calibrating and mosaicing the near-infrared image, and to Kurt Adelberger and Chuck Steidel for generously providing the visual images after taking, reducing and calibrating them. The Hubble Deep Field (HDF) database was planned, taken, reduced and made public by a large team at Space Telescope Science Institute headed by Bob Williams.

References

- Bertin E. & Arnouts S., 1996, SExtractor: Software for source extraction, *A&AS* 117 393
- Djorgovski S. *et al.*, 1995, Deep galaxy counts in the *K* band with the Keck Telescope, *ApJ* 438 L13
- Hogg D. W., Neugebauer G., Armus L., Matthews K., Pahre M. A., Soifer B. T. & Weinberger A. J., 1997a, Near infrared imaging of the Hubble Deep Field with the Keck Telescope, *AJ* 113 474
- Hogg D. W., Pahre M. A., McCarthy J. K., Cohen J. G., Blandford R. D., Smail I. & Soifer B. T., 1997b, Counts and colors of faint galaxies in the *U* and *R* bands, *MNRAS* 288 404
- Jarrett T. H., Beichman C., Van Buren D., Gautier N. & Bruce C., 1994, in *Infrared Astronomy with Arrays: The Next Generation*, ed. McLean I., Kluwer, Dordrecht, 293
- Metcalfe N., Shanks T., Fong R. & Roche N., 1995, Galaxy number counts III: Deep CCD observations to $B = 27.5$ mag, *MNRAS* 273 257
- Pahre M. A. *et al.*, 1997, An infrared-selected faint field galaxy redshift survey II: *U B V R_C I_C K* photometry of a field at J0053+1234, *ApJS* submitted
- Steidel C. C. & Hamilton D., 1993, Deep imaging of high redshift QSO fields below the Lyman limit II: Number counts and colors of field galaxies, *AJ* 105 2017
- Williams R. E. *et al.*, 1996, The Hubble Deep Field: Observations, data reduction and galaxy photometry, *AJ* 112 1335

band	area (arcmin ²)	exposure (s)	pixel size (arcsec)	seeing FWHM (arcsec)	flux limit (mag)
U_n	75	23400	0.283	1.3	25.0
G	75	7200	0.283	1.2	26.0
\mathcal{R}	75	6000	0.283	1.1	25.5
K_s	56	2430	0.494	1.5	20.0

Table 2.1: Parameters of the imaging data, for the final, stacked mosaics. The “flux limit” is approximate and explained in Section 2.7.

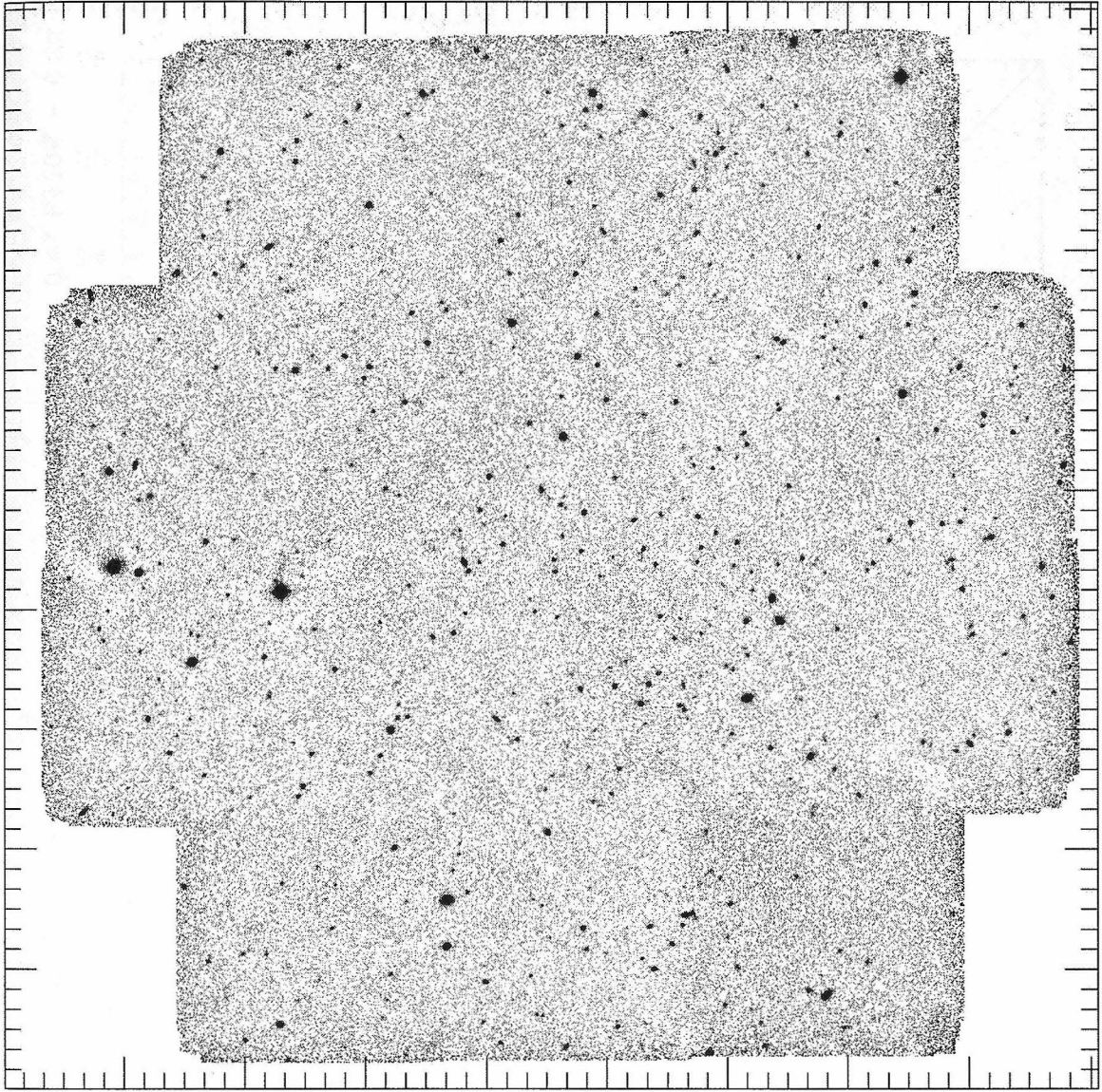


Figure 2.1: The final K_s -band mosaic. The small tick marks are separated by 10 arc-sec, the large by 1 arcmin.

May 22 10:51:54 1997

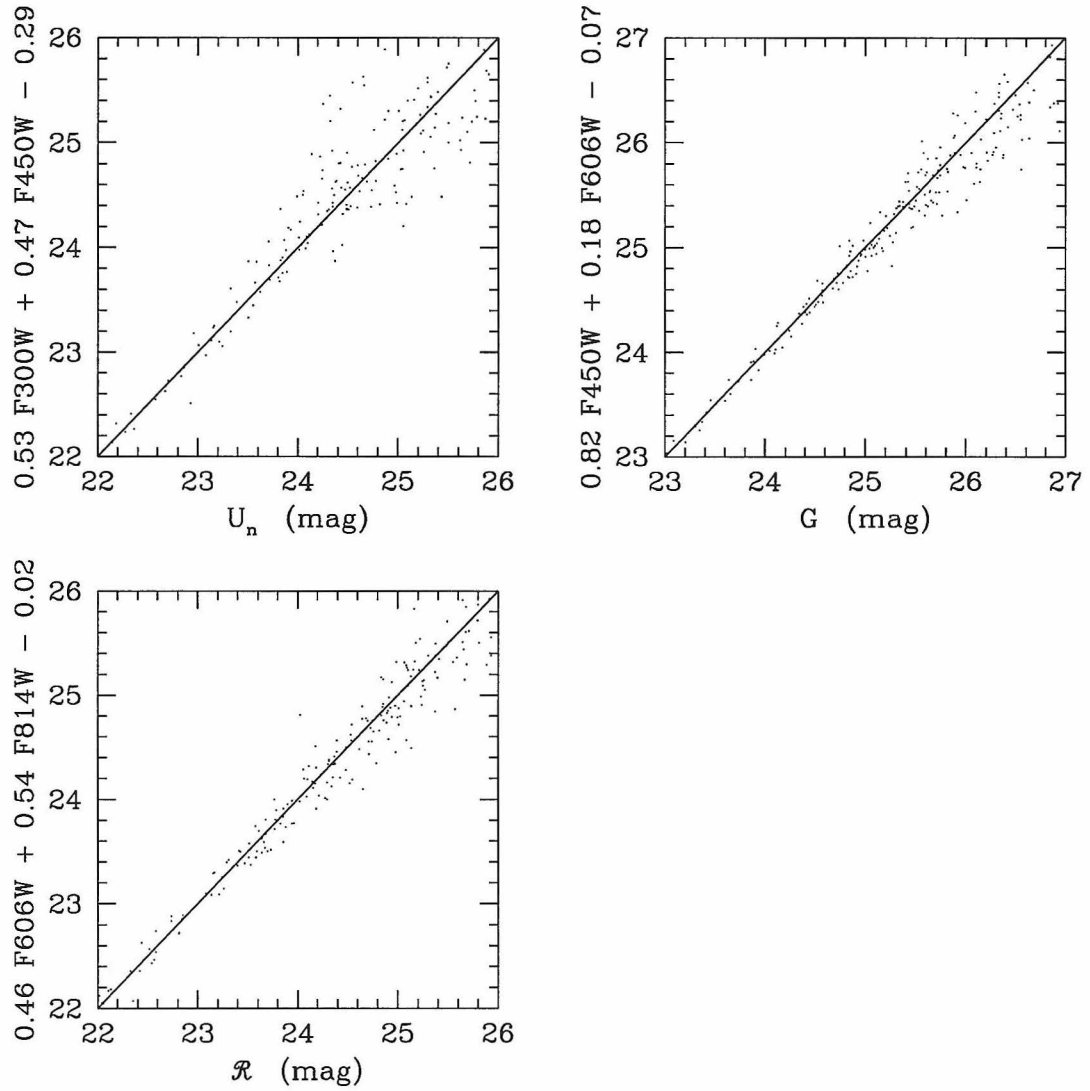
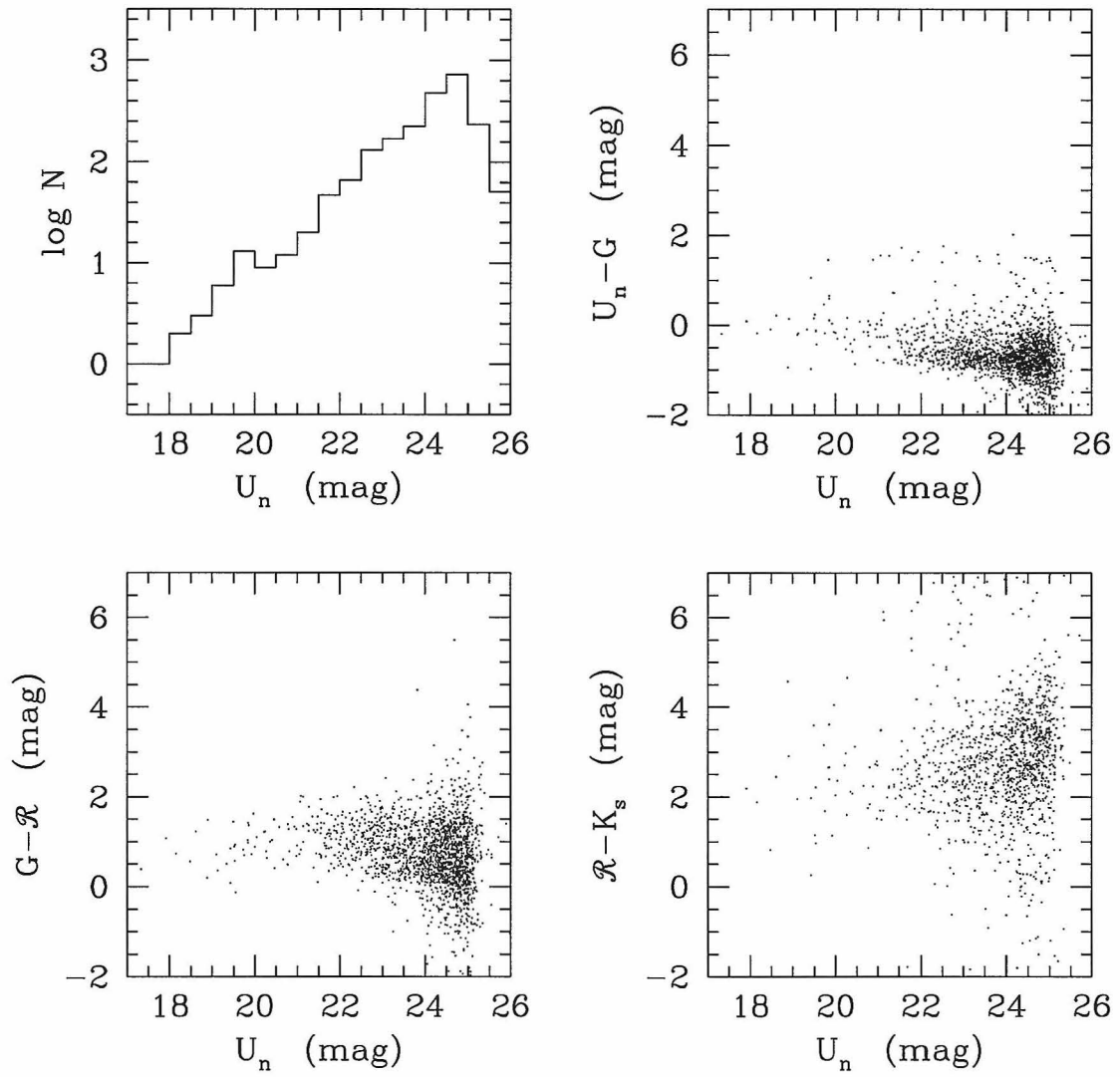
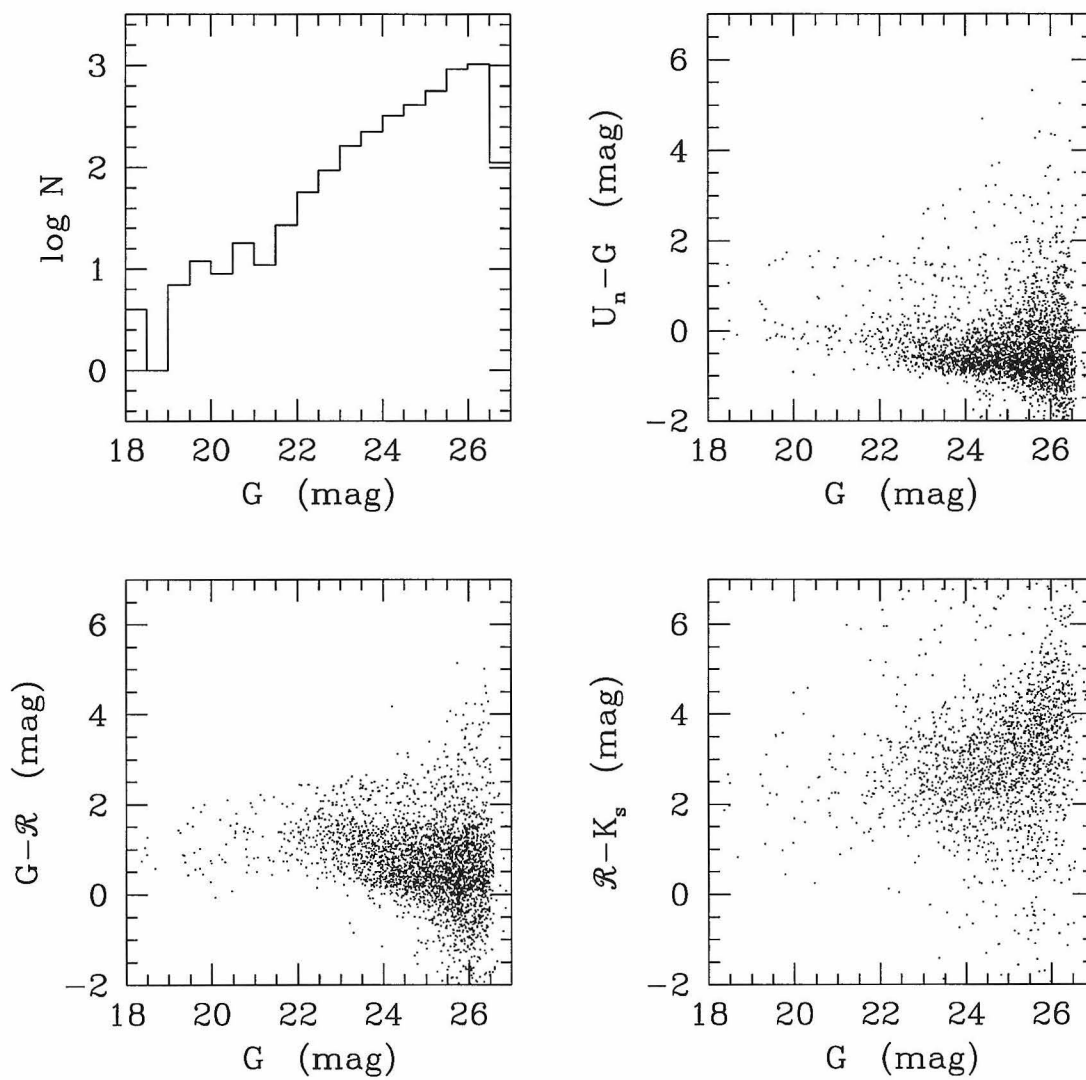


Figure 2.2: Comparison of ground-based visual and transformed HST magnitudes for the \mathcal{R} -selected sample. These plots were used to calibrate the U_n , G and \mathcal{R} images.

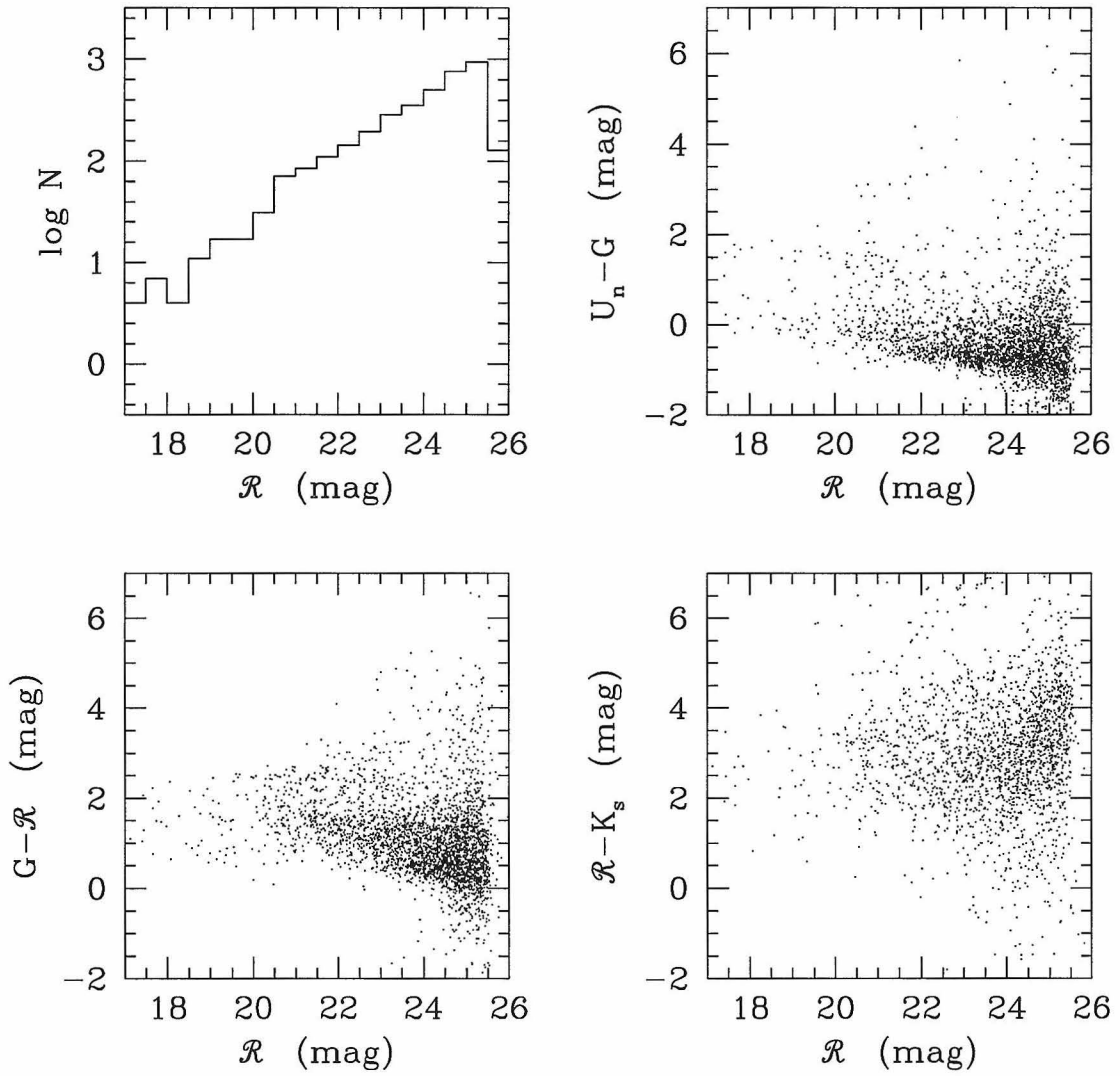
May 22 10:52:14 1997

Figure 2.3: Number counts of U_n -selected sources and their colors.

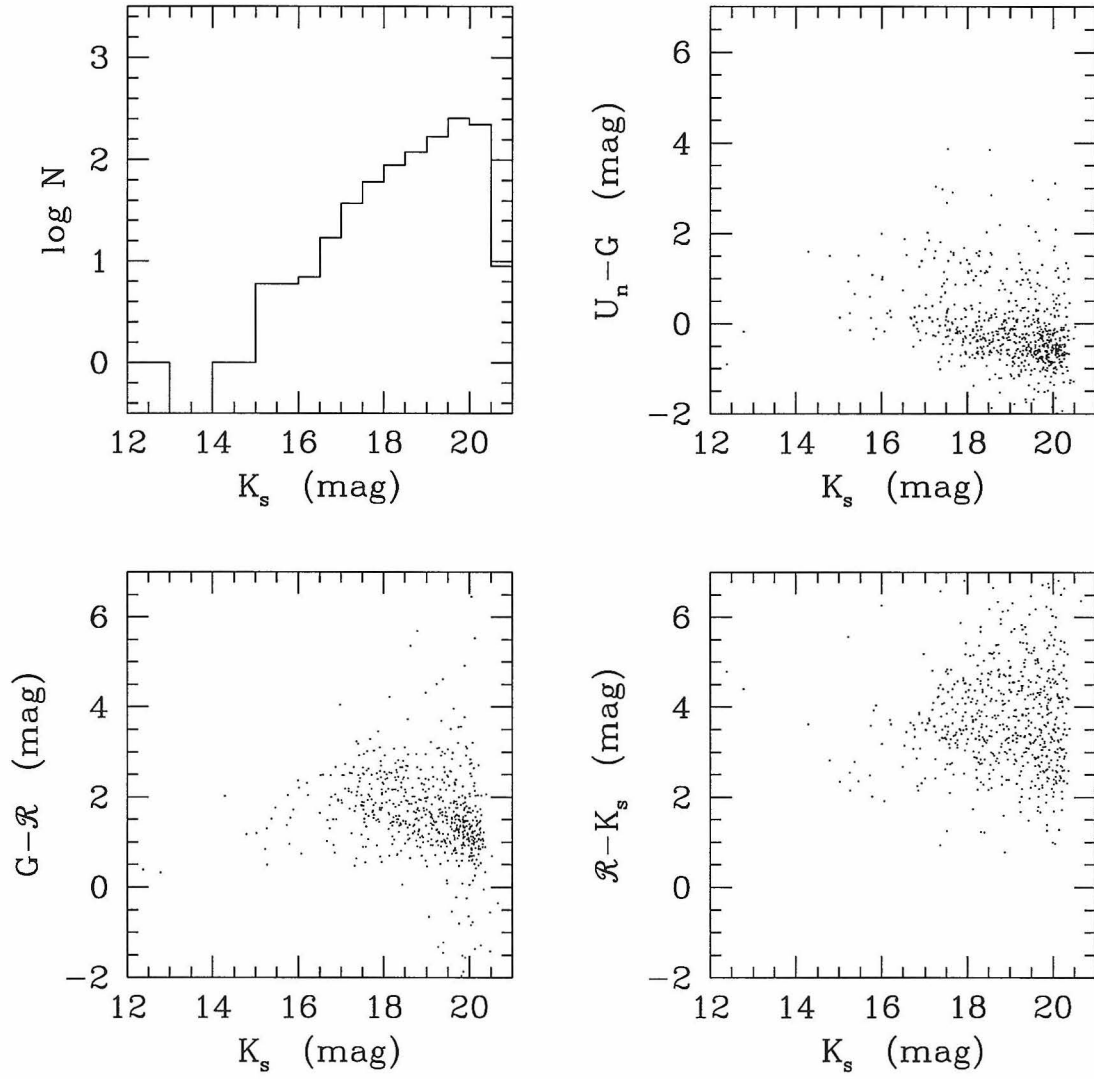
May 22 10:52:23 1997

Figure 2.4: Number counts of G -selected sources and their colors.

May 22 10:52:36 1997

Figure 2.5: Number counts of \mathcal{R} -selected sources and their colors.

May 22 10:52:46 1997

Figure 2.6: Number counts of K_s -selected sources and their colors.

Chapter 3 Faint galaxy oxygen-II emission, redshift identification, and star formation rates

3.1 Introduction

The [O II] line at 3727 Å is actually a pair of atomic transitions for singly ionized oxygen, the $^2D_{3/2}$ to $^4S_{3/2}$ at 3726 Å and the $^2D_{5/2}$ to $^4S_{3/2}$ at 3729 Å. The transitions are forbidden, meaning that there is no electric dipole connection between the initial and final states, so the spontaneous emission rates are small, 1.8×10^{-4} and $3.6 \times 10^{-5} \text{ s}^{-1}$ for the 3726 and 3729 Å transitions respectively (Osterbrock 1989). For this reason, the [O II] line is usually collisionally excited by free electrons in hot nebulae, where “hot” means around 10^4 K to excite the 3.3 eV transitions. If the electron density is very low, collisional excitation is rare, whereas if it is very high, excited atoms are more likely to be deexcited by a subsequent collision than by spontaneous emission, so there are critical electron densities n_c at which the transitions saturate observationally, defined to be the electron densities at which the collisional excitation rates equal the spontaneous emission rates. The critical densities depend on temperature because the collisional excitation cross sections do, but at typical temperatures they are roughly 1.6×10^4 and $3 \times 10^3 \text{ cm}^{-3}$ for the 3726 and 3729 Å transitions respectively (Osterbrock 1989). (The fact that the two critical densities are different means that the 3726/3729 line ratio can be used to measure electron density.)

The conditions of temperature and density required to excite the [O II] 3727 Å line are met in H II regions, clouds of ionized hydrogen heated by massive, young, luminous stars. For this reason, the [O II] emission of a galaxy is sensitive to its young stellar population, or recent star formation history. In the local Universe, the

relationship between [O II] luminosity and star formation has been calibrated

$$L_{[\text{O II}]} = 2 \times 10^{33} \text{ W} \frac{R}{1 \text{ M}_{\odot} \text{ yr}^{-1}} \quad (3.1)$$

where R is the star formation rate (Kennicutt 1992). Of course this relationship shows a strong galaxy-to-galaxy scatter. It depends on galaxy dust content because dust absorbs strongly in the ultraviolet. It also depends on the stellar initial mass function because the [O II] luminosity is tied only to the massive star population, not to the broad mass range thought to be produced simultaneously in star forming regions. Furthermore, because the line is always optically thin, its luminosity ought to be proportional to oxygen abundance, which depends on a galaxy's age and star formation history.

Because the [O II] line tends to be a strong emission line in objects with significant young stellar populations, and because it is inside the window for visual spectroscopy in the redshift range $0.2 < z < 1.5$, it is a very important line for faint galaxy redshift identification. The faintest faint galaxy redshift surveys will always be subject to significant incompleteness among the faintest sources, because that is the design criterion by which samples are selected. For example, a recent flux-limited survey to $B = 24$ mag at the 4-m William Herschel Telescope is 73 percent complete (Glazebrook *et al.* 1995). A deeper survey with the 10-m Keck Telescope more-or-less shows that most of the incompleteness in the shallower survey probably consists of sources at redshifts around unity and beyond (Cowie *et al.* 1996), unidentified because [O II] 3727 is difficult to find in the red where sky lines become more numerous and strong and the spectrograph sensitivity is dropping. But of course now the Keck Telescope redshift surveys are also being pushed to flux levels at which they are substantially incomplete, with no possibility of testing the incompleteness with a larger telescope in the near future. These very faint levels are the most interesting for constraining the evolution of galaxies, both because the faintest samples are most likely to contain the largest numbers of high-redshift sources, and because what evolution has been found in the luminosity function has been most dramatic among low-luminosity

galaxies (Lilly *et al.* 1995; Ellis *et al.* 1996). Unfortunately, conclusions about galaxy evolution drawn from an incomplete sample are sensitive to what is assumed about the redshift dependence of the incompleteness.

The redshift-dependence of the incompleteness of a redshift survey can be computed (or at least constrained) if the statistical properties of the spectra of the sources under study are known or can be estimated and the spectrograph and observing technique are understood. This is the primary goal of this Chapter. Even if it is impossible to quantitatively determine the full completeness function, it is important to know whether the majority of the incompleteness in Keck Telescope redshift surveys can be entirely attributed to the difficulty of detecting [O II] 3727 at high redshift, or whether a significant low-redshift incompleteness is required as well. This question can be answered without perfect knowledge of the completeness function because it only requires a one-sided limit.

As a spin-off of these studies, [O II] equivalent width and line strength distributions are obtained, along with a luminosity function of galaxies in the [O II] line and its evolution. These directly constrain the ages and star formation histories of galaxies in the Universe.

In what follows, physical quantities are quoted in SI units, with Hubble constant $H_0 = 100 h \text{ km s}^{-1} \text{ Mpc}^{-1}$, in world model $(\Omega_M, \Omega_\Lambda) = (0.3, 0)$ (Appendix B). The only exception are number densities, which are given in $h^3 \text{ Mpc}^{-3}$. Fluxes and luminosities are given as flux and luminosity densities per logarithmic frequency interval, *i.e.*, νS_ν or λS_λ and νL_ν or λL_λ , in W m^{-2} and W. Luminosities are all-sphere (not per-steradian).

3.2 Sample, observations, and line measurement

For the purposes of this Chapter, the sample is an incompletely observed magnitude-limited sample, selected in the R band, in the Hubble Deep Field (HDF, Williams *et al.* 1996) and a roughly 8-arcmin diameter circular field surrounding it. The general sample selection is described in the previous Chapter and the spectroscopy is described

by Cohen *et al.* (in preparation). Briefly, the sample is selected to be all sources, independent of morphology, brighter than $R = 23$ mag in the 8-arcmin diameter circular field and brighter than $R = 24$ mag in the small HDF proper (most of the central 2×2 arcmin²). The spectroscopy of this sample is only about 55 percent complete for the purposes of this Chapter, which is based on 256 spectra. Fluxes in the \mathcal{R} band and $\mathcal{R} - K_s$ colors are measured with data from the COSMIC and Prime Focus IR cameras on the Hale 200-inch Telescope as described in Chapter 2. Spectroscopy is performed with the LRIS instrument on the Keck Telescope (Oke *et al.* 1995) with a 300 mm^{-1} grating, at a resolution of about 2.5 \AA per pixel, for exposure times of 6000 to 9000 s (Cohen *et al.* in preparation).

Figure 3.1 shows some example spectra from the sample, cut out around the [O II] 3727 \AA line.

The continua are fit over the wavelength range from 200 \AA to 50 \AA shortward of the observed 3727 location and the range from 50 \AA to 200 \AA longward. Each fit is performed with six iterations of sigma-clipping at $\pm 2.5 \sigma$, where σ is the root-mean-square (RMS) residual noise per pixel. The uncertainty in the continuum value at the line center is taken to be the per-pixel RMS divided by the square root of the number of pixels contributing to the continuum fit (after sigma-clipping).

The line strength is measured by summing the differences between observed spectrum and continuum fit in the 30 \AA (full-width) aperture centered on the line location. The uncertainty in this strength is taken to be the per-pixel RMS times the number of pixels contributing to the line flux.

3.3 Equivalent width distributions

The rest-frame equivalent width W of a line in the spectrum of an object at redshift z is the wavelength interval of continuum which would provide the same total flux, corrected for redshift

$$W \equiv \frac{1}{1+z} \frac{\int S_\lambda d\lambda}{S_\lambda^{(c)}} \quad (3.2)$$

where z is redshift, the integral is over only that spectral region which contains the line, S_λ is the flux density (per unit observed wavelength λ) and $S_\lambda^{(c)}$ is the flux density in the continuum at the location of the line; *i.e.*, the flux density which would be observed sans line. The equivalent width is a robust measure of the strength of a spectral feature relative to the source's continuum measure; it does not depend on absolute calibration of the spectrum or even the relative calibration of different parts of the spectrum. *I.e.*, it is a local, geometric measure of the line strength.

For the purposes of this Chapter, the fractional uncertainty in an equivalent width measurement is taken to be the sum in quadrature of the fractional uncertainties in the continuum measurement and line strength. The latter uncertainty estimates are described above.

The rest-frame [O II] 3727 equivalent widths for the sample are shown in Figures 3.2 and 3.3, plotted against R -band magnitude and redshift z . Only spectra with good (signal-to-noise better than 2 in a pixel) continuum detections are plotted because badly estimated or zero continuum leads to large, unreliable equivalent width estimates. Figures 3.2 and 3.3 are encouraging for those undertaking faint galaxy redshift surveys because it shows that at higher redshifts and fainter fluxes, the equivalent widths of [O II] 3727 lines become greater. The observed equivalent widths become even greater because of the additional factor of $(1 + z)$. Just how much this helps faint galaxy redshift surveys is the subject of this Chapter.

The trend of increasing [O II] 3727 equivalent width with magnitude shown in Figure 3.3 suggests the possibility of a non-trivial relationship between equivalent width and source luminosity. The most crude estimate of the source absolute magnitude M_R (absent color information) is $M_R = R - DM$ where DM is the distance modulus, $5 \log[D_L/(10 \text{ pc})]$, where D_L is the luminosity distance (see Appendix B). The rest-frame equivalent widths are plotted against this crude absolute magnitude estimate in Figure 3.4 in four different redshift bins.

Figure 3.4 shows weak evidence for an interesting trend: at redshifts less than 0.8, the [O II] equivalent width distribution appears to have a larger upper bound for intrinsically fainter sources. This effect has been noted before (*e.g.*, Cowie *et al.*

1996), and is thought to indicate that smaller galaxies have formed a larger fraction of their stars recently; or, smaller galaxies formed more recently. Only at high redshifts does one find intrinsically bright galaxies with large [O II] 3727 equivalent widths.

Interestingly, there is another context in which such an “inverse” correlation between equivalent width and luminosity is seen: The equivalent widths of high-ionization lines such as [C IV] and [N V] in quasars is inversely correlated with source luminosity (Baldwin 1977; Osmer *et al.* 1994). Dubbed the “Baldwin effect,” this anti-correlation is usually attributed to an orientation effect. Quasar continuum is thought to come at least partly in a beamed component, while the high-ionization lines come from an isotropically emitting cloud around the nucleus. Higher-luminosity sources are by-and-large seen more “head-on” and will therefore show higher continuum to line ratios, or smaller equivalent-width emission lines. Although the effect seen for faint galaxies at redshifts $z < 0.8$ is empirically identical to the Baldwin effect seen for high-redshift quasars, it is attributed to a totally different mechanism, the more recent formation of smaller galaxies. One argument that any faint-galaxy Baldwin effect is really due to variations in star formation rate is that there is a correlation between color and equivalent width, with bluer (and hence younger) sources showing stronger [O II] 3727 lines, shown in Figure 3.5. Furthermore, if the [O II] line really comes from H II regions, it should be emitted isotropically, so beaming ought not be important.

Figures 3.2, 3.3 and 3.4 are subject to an important selection effect: faint or high-redshift sources with small equivalent widths will simply not be successfully assigned a redshift at all. This selection effect clears out the faint–small-width and high-redshift–small-width parts of Figure 3.2 and the intrinsically-faint–small-width parts of Figure 3.4. However, it does not explain the lack of observed objects at bright levels or low redshifts with large equivalent widths. So this Baldwin effect for faint galaxies cannot be entirely explained away in this manner. On the other hand, sources with very weak continuum detections will tend to have over-estimated equivalent widths (because the Gaussian-distributed continuum level is in the denominator of a ratio) and there are more such weak-continuum sources at the faint end of the survey. It

is possible that some of the apparent faint-galaxy Baldwin effect may be due to this bias although Figure 3.4 is not obviously dominated by weak continuum sources.

It is also worthy of note that Figure 3.2 shows clumps in redshift–equivalent-width space. This suggests that the galaxies which are likely to be dynamically related in high-redshift groups (Cohen *et al.* 1996a, 1996b) are also related in terms of stellar content. It suggests that at least some of the galaxies in each group formed at the same time and with similar stellar populations. This is nicely consistent with the observation that groups are long-lived, primordial structures which exist at high redshift in relatively high abundance (Cohen *et al.* 1996a, 1996b; Steidel *et al.* 1997).

3.4 Equivalent width distribution model

The completeness function requires a model for the distribution of [O II] equivalent widths as a function of redshift, magnitude and color. Unfortunately, the sample includes only a few hundred sources and is subject to the selection biases mentioned above, so extremely accurate modeling is not possible.

It is assumed that the distribution function $f(W)$ (probability per wavelength, normalized so $\int f dW$ is unity) for rest-frame equivalent widths W is a function of W/w only, where

$$w \equiv (1+z)^a b^n \quad (3.3)$$

where a and b are constants, z is redshift, and n is the spectral power-law slope, defined by $\nu f_\nu \propto \nu^n$, measured in the $\mathcal{R} - K_s$ spectral region. The idea is to use w to scale out all the color- and redshift-dependence of the equivalent width distribution. Assuming that galaxy spectra are close to power-laws, the spectral index n can be estimated by

$$n \approx \frac{\mathcal{R} - K_s}{2.5 \log[\nu_{K_s}/\nu_{\mathcal{R}}]} + \frac{Z_{K_s} - Z_{\mathcal{R}}}{\log[\nu_{K_s}/\nu_{\mathcal{R}}]} = -0.82(\mathcal{R} - K_s) + 0.89 \quad (3.4)$$

where ν_{K_s} and $\nu_{\mathcal{R}}$ are the effective frequencies and Z_{K_s} and $Z_{\mathcal{R}}$ are the logarithmic absolute calibrations $\log[\nu f_\nu^{(0)}]$ for the K_s and \mathcal{R} bands, given in Appendix A.

Unfortunately, the number of sources with good [O II] equivalent width measurements is not large enough to determine a and b very accurately, especially since the analysis has been restricted to those sources with per-pixel continuum detections better than a signal-to-noise of two. However, manual variation of b to remove the strong color–width correlation shown in Figure 3.5 followed by variation of a to remove some residual redshift–width correlation gave rough values of $a \approx 1$ and $b \approx 2$. The degree to which these values scale out the trends of W with magnitude, color and redshift is shown in Figure 3.6. The values $a = 1$ and $b = 2$ are adopted hereafter.

Bins of width 20 \AA in W/w are assigned and the fraction of sources with scaled, rest-frame equivalent widths W/w in each bin is estimated. The low- W/w part of the distribution (*i.e.*, the relative numbers in the $0 < W/w < 20 \text{ \AA}$ and $20 < W/w < 40 \text{ \AA}$ bins) is estimated with sources with $\mathcal{R} < 21.5$ mag and the higher- W/w part estimated with all sources with $\mathcal{R} < 23$ mag. The results are given in Table 3.1. Unfortunately, the distribution of W/w does not fit any simple functional form, such as an exponential distribution, so from here on, the step-function probability distribution implied by Table 3.1 is used as the true distribution.

3.5 Instrumental sensitivity to line emission

Since the interest here is in the completeness function for a particular survey, the Caltech faint galaxy redshift survey, information about the instrument used, the Keck Low Resolution Imaging Spectrograph (LRIS; Oke *et al.* 1995) is necessary. In particular, sensitivity and spectral coverage functions are required which can be combined with a model for the distribution of line strengths to provide an estimate of the probability $\eta_{\text{got}}(m, z)$ that an object with magnitude m and redshift z is successfully assigned a redshift on the basis of identification of the [O II] line.

The identification of the line at redshift z depends on (a) the fraction of spectra in the sample which include wavelength $(3727 \text{ \AA})(1 + z)$ in their spectral range, (b) the total sensitivity of the atmosphere plus telescope plus instrument to line flux at $(3727 \text{ \AA})(1 + z)$, and (c) the accuracy to which night sky and other background

emission can be subtracted at $(3727 \text{ \AA})(1+z)$. Because the spectrograph is a multi-slit design, different sources in the survey are observed over different wavelength ranges, depending on the position of the source within the field of the instrument. The wavelength coverage function can be constructed by taking the minimum and maximum possible source locations and assuming that on any given slitmask sources are evenly distributed between these extremes. The sensitivity to flux (in the sense of νS_ν) can be estimated with observations of spectrophotometric standard stars. The sensitivity varies from night to night, so in principle this function should be replaced with a distribution function which takes into account the variation in observing conditions. Furthermore, in the multislit design, if there are any positional errors in the catalog or mask misalignment while observing, different sources will be centered on their slits with different precisions. This leads to a random scatter in throughputs, even for sources observed simultaneously. The sky brightness, color and emission line spectrum also vary from night to night. In principle the expected sensitivity to 3727 emission can be estimated from the coverage, sensitivity, and sky brightness functions. However, because the sensitivity depends on data reduction technique, includes the complications of assessing slitmask alignment, and may be compromised by unknown instrumental effects, a purely empirical approach is taken here, using the reduced spectra themselves to assess the sensitivity.

The signal-to-noise ratio r (defined to be continuum level divided by pixel-to-pixel rms), is measured in every spectrum in the sample at a set of wavelengths corresponding to the 3727 line at various redshifts in the range $0 < z < 1.8$, by exactly the procedure used to estimate the continuum in the equivalent width measurements described above. The rms is computed from only those pixels not rejected by the sigma-clipping algorithm, which is perhaps optimistic. These continuum signal-to-noise ratios are “scaled” to the value they would have if the source had $\mathcal{R} = 23$ mag and a $\mathcal{R} - K_s$ spectral index $n = 0$. This scaling is done by multiplying the measured signal-to-noise ratio by

$$10^{0.4(\mathcal{R}-23)} \left(\frac{1+z}{1.85} \right)^n \quad \text{if } \mathcal{R} > 21.5 \text{ mag}$$

$$10^{0.4(-1.5)} \left(\frac{1+z}{1.85} \right)^n \quad \text{if } \mathcal{R} < 21.5 \text{ mag} \quad (3.5)$$

where the switch-over at $\mathcal{R} = 21.5$ mag takes place because fainter than that most of the source is in the slit and intensity through the slit is proportional to total source flux, while brighter than that the source is typically larger than the slit and intensity through the slit depends only weakly on total source flux since the bright galaxies in the sample have similar surface brightnesses. The $1+z$ term is divided by 1.85 because $z = 0.85$ puts 3727 into the center of the \mathcal{R} band. The switch-over magnitude was determined by trial-and-error, with the test being that the distribution of scaled signal-to-noise ratios not depend strongly on magnitude. The signal-to-noise ratio can be converted into a sensitivity to rest-frame equivalent width, expressed in terms of the smallest detectable rest-frame equivalent width

$$W_{\text{lim}} = \frac{\eta \lambda_1}{r} \left(\frac{\Delta\lambda}{\lambda_1} \right)^{1/2} (1+z)^{-1/2} \quad (3.6)$$

where η is the minimum necessary signal-to-noise ratio for 3727 to be detected, taken to be 3, r is the scaled signal-to-noise ratio in the continuum, λ_1 is the wavelength per pixel, usually 2.5 Å for these spectra, $\Delta\lambda$ is the rest-frame full-width of the 3727 line, taken to be 10 Å, and z is the redshift. Because the formula for W_{lim} includes r in the denominator, the scaled value can be converted back into the true sensitivity to rest-frame equivalent width by multiplying by the factors given in (3.5).

Since the continuum of every spectrum is measured at every redshift, there are a huge number of scaled W_{lim} estimates from which a model of the spectrograph sensitivity can be constructed. At each redshift the scaled sensitivities are ranked and a cumulative distribution is constructed. This distribution is shown in Figure 3.7. The distribution is plotted cumulatively so that it can be treated as a probability, given a source with a given redshift and [O II] equivalent width, that the line is detected.

Note that this sensitivity function is empirical, derived from the sample of spectra themselves, and is only valid for this survey, because it depends on the instrument, site, observational technique, reduction method, and selection function. The sensitiv-

ity gets worse at redshifts $1 < z < 1.25$ because the CCD efficiency is dropping while the sky brightness and number of bright night sky emission lines are both increasing, and then very bad at redshifts $1.25 < z < 1.5$ because in addition the fraction of spectra with coverage at long enough wavelength is also decreasing. Similarly, the bad sensitivity at low redshifts $z < 0.3$ is also caused by a decreasing fraction of spectra with coverage at short enough wavelengths.

3.6 Line detection probability function

The convolution of the [O II] equivalent width distribution computed in Section 3.4 and given in Table 3.1 with the sensitivity to [O II] emission computed in the previous Section and displayed in Figure 3.7 is the probability that any individual source in the survey will have a detected [O II] line. This probability is a function of magnitude \mathcal{R} because the sensitivity depends on the amount of flux. It depends on spectral index n because the bluer objects have stronger [O II] lines and because the magnitude is defined in the observed \mathcal{R} band while the sensitivity depends on the flux at the [O II] line at the relevant redshift. It depends on redshift z because both the sensitivity and line strengths vary with it, the former strongly and the latter weakly. The derived [O II] detection probability function $p(\mathcal{R}, n, z)$ is important because at redshifts $z > 0.6$, where redshifts are usually based on the [O II] line, it is closely related to the completeness of the survey. This probability function is plotted, versus redshift, for a few different magnitudes and spectral indices, in Figure 3.8.

Of course the [O II] detection probability function is not the completeness function of the survey, because, especially at low redshift, there are other spectral features on which redshifts can be based. However, at redshifts $z > 0.6$, when other features are falling off the long-wavelength end of the spectrum, this may be an accurate estimate.

3.7 The [O II] luminosity function

The observations of line widths, along with photometry and, most importantly, the sensitivity function shown in Figure 3.7, can be used to compute a luminosity function of galaxies in the [O II] line. This in turn provides a luminosity density of the Universe in this line, as a function of redshift, which can be related directly to a volume-averaged star formation rate in the context of a stellar population model.

For any galaxy, the line luminosity $L_{[\text{O II}]}$ can be crudely computed with the rest-frame equivalent width W , the flux S (defined to be νS_ν) and the index n (defined so $\nu S_\nu \propto \nu^n$) by

$$\log L_{[\text{O II}]} = \log \left[\frac{W}{3727 \text{ \AA}} \right] + \log S + \log[4\pi] + 2 \log D_L(z) - n \log \left[(1+z) \frac{3727 \text{ \AA}}{\lambda_{\mathcal{R}}} \right] \quad (3.7)$$

where $D_L(z)$ is the luminosity distance in an $(\Omega_M, \Omega_\Lambda) = (0.3, 0.0)$ universe (Appendix B), and $\lambda_{\mathcal{R}}$ is the effective wavelength of the \mathcal{R} band, or 6900 Å. Note that this is an all-sphere (not per-steradian) luminosity definition. Fluxes are derived from \mathcal{R} -band magnitudes using the conversions in Appendix A. This prescription for line luminosity is crude because the spectral energy distributions of galaxies are not pure power-laws, and, furthermore, in this Chapter the index n has been computed from the $\mathcal{R} - K_s$ color, which does not “bracket” the [O II] line unless the redshift is $z > 0.85$. A refinement would be to compute n from, say, $G - \mathcal{R}$ at redshifts $z < 0.85$. In principle the need to use the flux S and index n can be obviated entirely because line fluxes can be measured directly from spectra when there are a spectrophotometric standard data. However, such procedures depend on perfect slit alignment on the galaxies and aperture corrections to account for line flux outside the slit. The procedure used here is more robust.

The luminosity function is estimated with a modified version of the V-max method (Chapter 4), in which each galaxy in the survey is assigned a volume V_{max} which is the volume of the Universe in which that source could lie and still meet the survey criteria. The inverse volumes of all the galaxies in a particular luminosity bin are

summed to estimate the luminosity function in that bin. In this application, there are two important complications in computing V_{\max} . The first is that the survey is highly incomplete, in the sense that only about half of the sources in the field are observed, at least for the data subsample used in this Chapter. Figure 3.9 shows the a priori completeness function, which is defined to be the fraction of the total sources in the field which were observed spectroscopically (see Chapter 4), as a function of \mathcal{R} -band flux. The second complication is that whether or not a source is in the sample depends not only on the a priori completeness function but also on the detection of the [O II] line itself, both because if it is not detected there is no luminosity (for the luminosity function) and because redshift identification often depends on [O II] detection anyway. Fortunately, however, the sensitivity to the [O II] line is computed in Section 3.5 and shown in Figure 3.7. Recall that the plotted sensitivity function is scaled to an equivalent $\mathcal{R} = 23$ mag, $n = 0$ source by the scaling given in (3.5); the scaling and the function in Figure 3.7 can be combined to make a total probability $p_{\text{detect}}(S, n, z, W)$ of detecting an [O II] line of equivalent width W in a source with flux S , index n and redshift z .

Given the completeness function and detection probability function, the appropriate formula for each galaxy's volume V_{\max} is

$$V_{\max} = \int_0^{\infty} \eta_{\text{try}}(S') p_{\text{detect}}(S', n, z', W) \frac{dV_{z'}}{d\Omega dz'} \Delta\Omega dz' \quad (3.8)$$

where S' is the flux the source would have if it were at redshift z' rather than its true redshift. The luminosity function $\phi(\log L_i)$ (number density per logarithmic interval in luminosity) in a bin of [O II] luminosity width $\Delta \log L$ centered on [O II] luminosity $L_{[\text{O II}]} = L_i$ is estimated with

$$\phi(\log L_i) = \frac{1}{\Delta(\log L)} \sum_{|\log L_{[\text{O II}],j} - \log L_i| < \Delta(\log L)} \frac{1}{V_{\max,j}} \quad (3.9)$$

where the sum is over all galaxies with luminosities in the bin, so index i labels luminosity bins and index j labels galaxies. Variances are computed by summing the

squares of the inverse volumes; the error bars on the Figures are the root variances.

The [O II] luminosity function is shown in Figure 3.10 for the entire sample used in this Chapter, in the redshift range $0 < z < 1.5$. It is compared to the local $H\alpha$ luminosity function from the UCM survey (Gallego *et al.* 1995) where the $H\alpha$ points have been shifted by a factor of 0.46 in luminosity because that is the mean observed [O II]/ $H\alpha$ flux ratio in the local Universe (Kennicutt 1992). Figure 3.11 shows the luminosity for two subsamples split in redshift at $z = 0.6$. This Figure shows a strong evolution in the [O II] luminosity function at the bright end. Although the total number density of [O II]-emitting galaxies is not significantly different between the two subsamples, the typical line luminosity is higher by an order of magnitude in the higher-redshift subsample. Both subsamples show a higher line luminosity than that which would be predicted from the very local UCM results, given the local [O II]/ $H\alpha$ flux ratio. Although there is some bias against luminous, low-redshift sources, it is not strong enough to produce the apparent evolution shown in Figure 3.11, especially since even the “low-redshift” sample goes to redshift $z = 0.6$, where there are many galaxies in the sample with luminosities around L^* .

3.8 The [O II] luminosity and star formation rate densities

As discussed in Section 3.1, the [O II] line luminosity is a star formation indicator, so the [O II] luminosity function is a measure of the star formation rate density of the Universe. For these purposes the entire luminosity function is not necessary, only the integrated luminosity density is needed. Because this is a single number rather than a function, it is possible to subdivide the sample more finely in redshift than was possible in Section 3.7.

The luminosity density $\mathcal{L}_{[\text{O II}]}$ in the [O II] line is estimated similarly to the luminosity function, using the same volumes V_{max} computed for those purposes (Section 3.7).

The integrated luminosity density is computed with

$$\mathcal{L}_{[\text{O II}]} = \sum_j \frac{L_{[\text{O II}],j}}{V_{\text{max},j}} \quad (3.10)$$

where galaxies are named by index j . The variance on this quantity is the sum of the square contributions. The [O II] line luminosity density as a function of redshift is shown in Figure 3.12. The Figure also shows the star formation rate density, computed from the luminosity density with the local calibration

$$L_{[\text{O II}]} = 2 \times 10^{33} \text{ W} \frac{R}{1 \text{ M}_{\odot} \text{ yr}^{-1}} \quad (3.11)$$

where R is the star formation rate (Kennicutt 1992). The point in Figure 3.12 at $z = 0.5$ is high relative to its neighbors; this is more likely due to several rich redshift-space overdensities in this redshift bin (Cohen *et al.* 1996b) than a true evolutionary trend.

Overall, Figure 3.12 implies that the star formation rate density was higher in the past and has dropped to the present day, although a full analysis must take account of the changing metallicities, gas and dust contents of high-redshift galaxies.

References

- Cohen J. G., Hogg D. W., Pahre M. A. & Blandford R., 1996a, Strong redshift clustering of distant galaxies, *ApJ* 462 L9
- Cohen J. G., Cowie L. L., Hogg D. W., Songaila A., Blandford R., Hu E. M. & Shopbell P., 1996b, Redshift clustering in the Hubble Deep Field, *ApJ* 471 L5
- Cowie L. L., Songaila A., Hu E. M. & Cohen J. G., 1996, New insight on galaxy formation and evolution from Keck spectroscopy of the Hawaii Deep Fields, *AJ* 112 839
- Ellis R. S., Colless M., Broadhurst T., Heyl J. & Glazebrook K., 1996, Autofib Redshift Survey I: Evolution of the galaxy luminosity function, *MNRAS* 280 235
- Gallego J., Zamorano J., Aragón-Salamanca A. & Rego M., 1995, The current star formation rate of the local Universe, *ApJ* 455 L1
- Glazebrook K., Ellis R., Colless M., Broadhurst T., Allington-Smith J. & Tanvir N., 1995b, A faint galaxy redshift survey to $B = 24$, *MNRAS* 273 157

- Kennicutt R. C. Jr., 1992, The integrated spectra of nearby galaxies: General properties and emission-line spectra, ApJ 388 310
- Lilly S. J., Tresse L., Hammer F., Crampton D. & Le Fevre O., 1995, The Canada-France redshift survey VI: Evolution of the galaxy luminosity function to $z \sim 1$, ApJ 455 108
- Oke J. B. *et al.*, 1995, The Keck Low-Resolution Imaging Spectrometer, PASP 107 375
- Osterbrock D. E., 1989, *Astrophysics of Gaseous Nebulae and Active Galactic Nuclei*, University Science Books, Mill Valley
- Steidel C. C. *et al.*, 1997, ApJ submitted
- Williams R. E. *et al.*, 1996, The Hubble Deep Field: Observations, data reduction and galaxy photometry, AJ 112 1335

W/w bin (\AA)	fraction
< 20	0.42
20–40	0.31
40–60	0.15
60–80	0.06
80–100	0.05
100–120	0.01
> 120	0

Table 3.1: Fractions of sources with scaled rest-frame [O II] equivalent widths W/w in each of several bins. See text for the definition of w , which scales out the color- and redshift-dependence of the equivalent width distribution. Fractional uncertainties in the fractions are at least at the tens of percent level.

Aug 27 09:48:21 1997

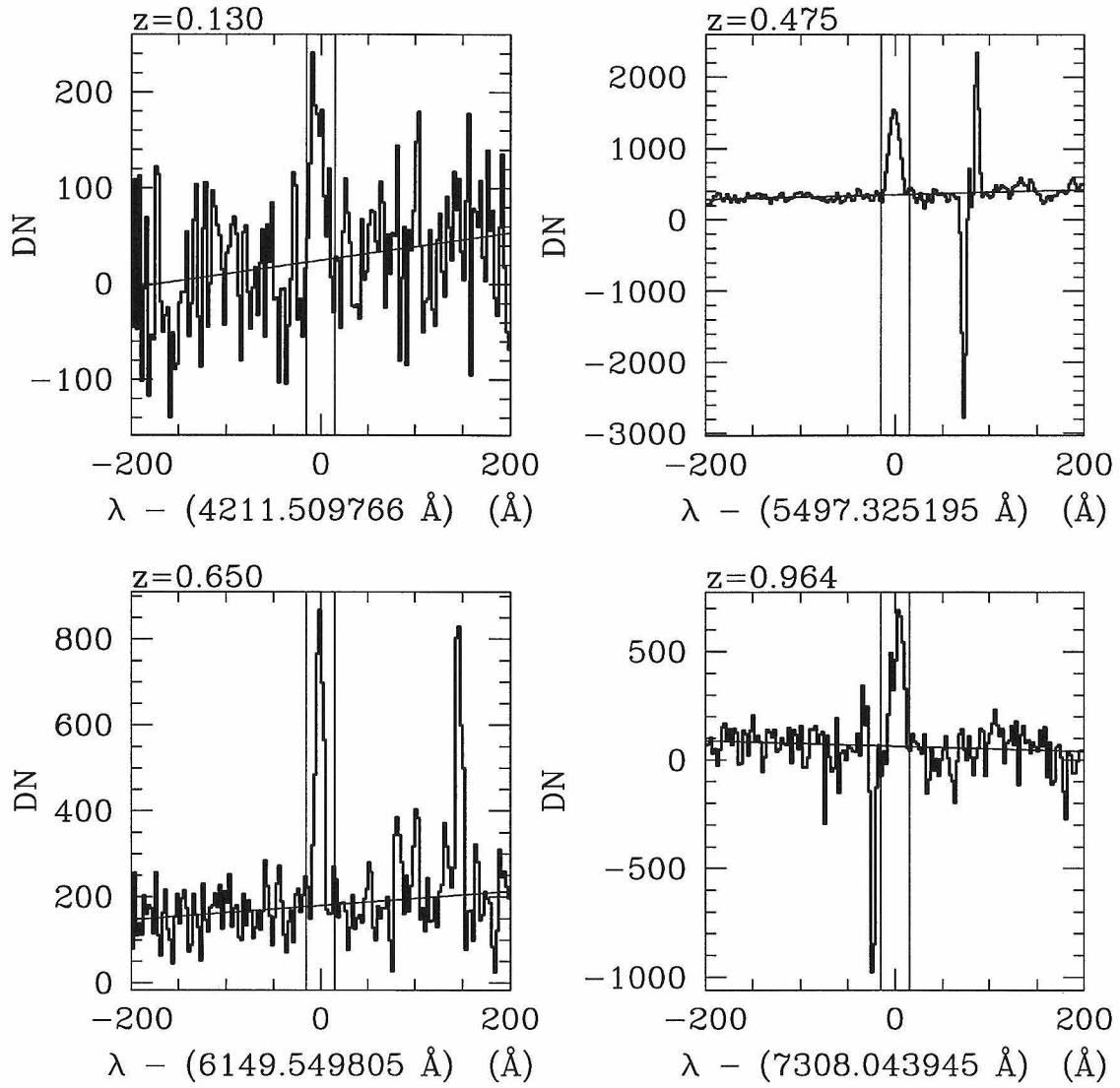


Figure 3.1: Example [O II] 3727 Å line detections for four sources from the sample. The data (in “data numbers” or DN) are shown with a dark line, the fit continuum with a thin straight line, and the aperture in which the 3727 line strength is measured with two thin vertical lines. The redshift of each source is given in the top left corner of each plot. Spikes or features not at zero wavelength are residuals of sky lines imperfectly subtracted.

Aug 27 10:01:03 1997

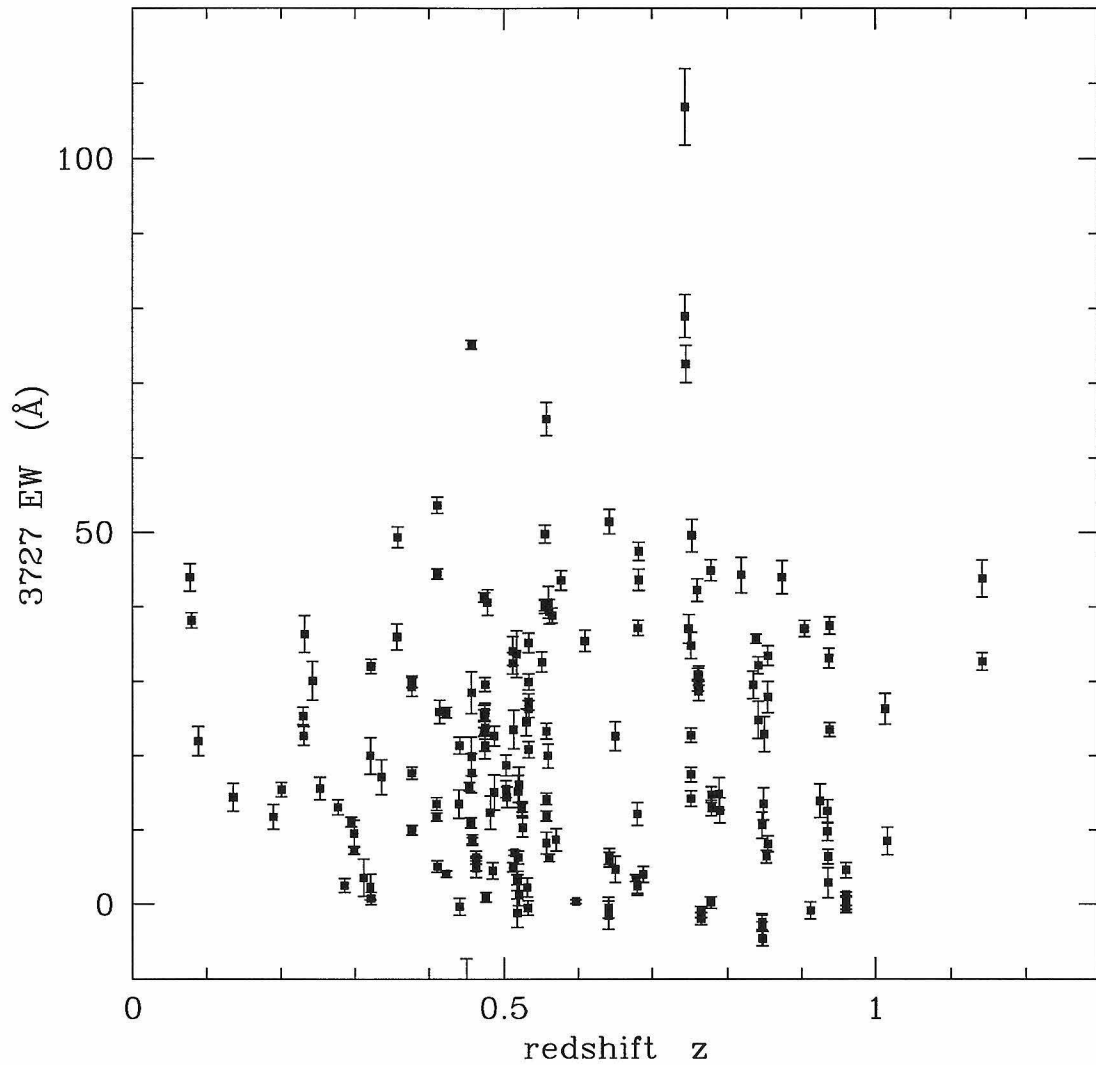


Figure 3.2: Rest-frame [O II] 3727 Å line equivalent widths plotted against redshift z . Only those spectra with continuum detections near rest-frame 3727 Å better than a signal-to-noise ratio of 2 (in one pixel) are plotted. Uncertainty estimates are described in Section 3.2. The error bars are all much smaller than 50 percent because the two-sigma limit on the continuum is a per-pixel limit, while in fact many pixels around 3727 were used to determine the continuum level, making the continuum measurement much more secure than two sigma.

Aug 27 10:01:23 1997

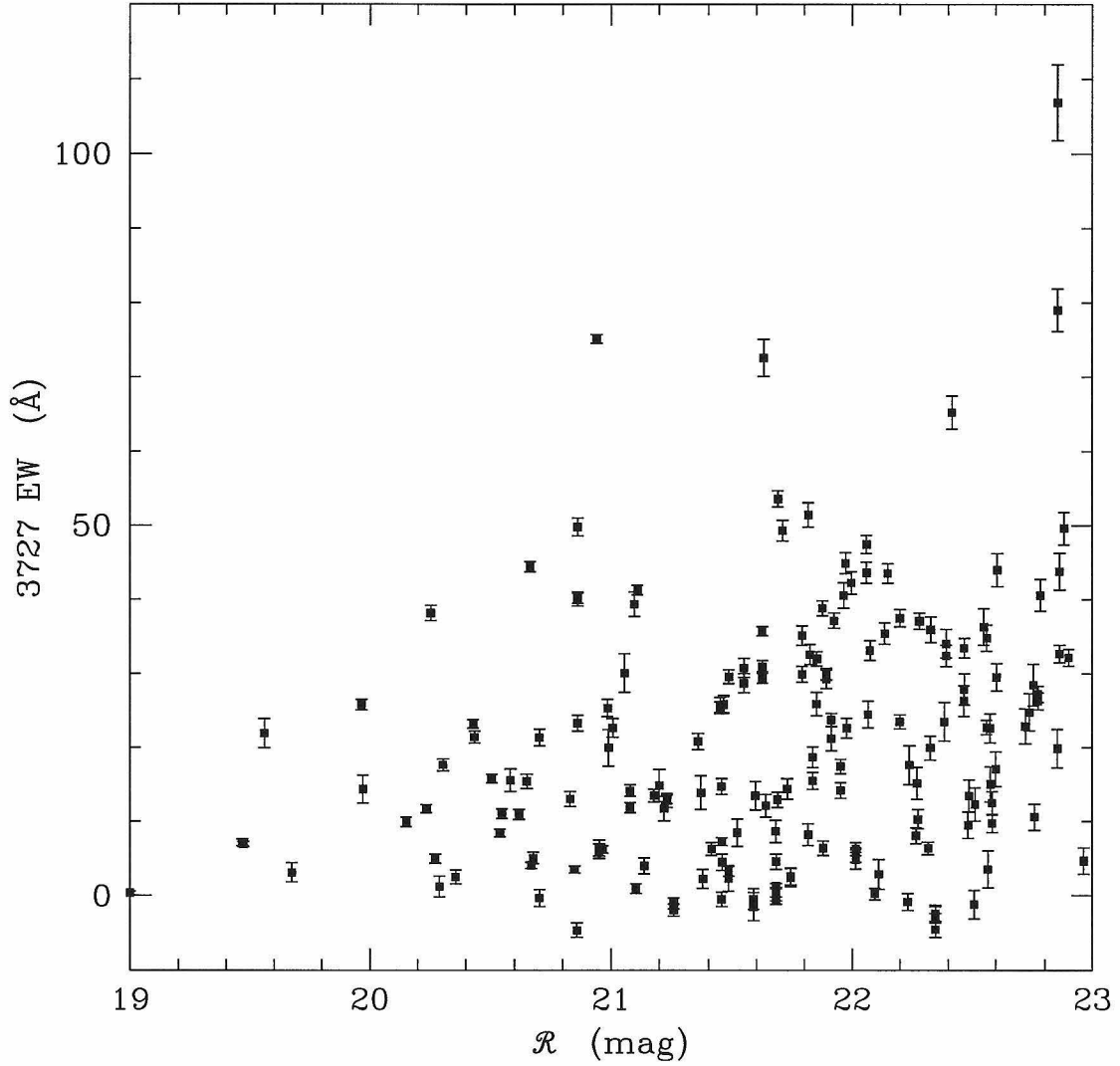


Figure 3.3: Rest-frame [O II] 3727 Å line equivalent widths plotted against \mathcal{R} -band apparent magnitude. Only those spectra with continuum detections near rest-frame 3727 Å better than a signal-to-noise ratio of 2 (in one pixel) are plotted. Uncertainty estimates are described in Section 3.2.

Oct 3 11:34:44 1997

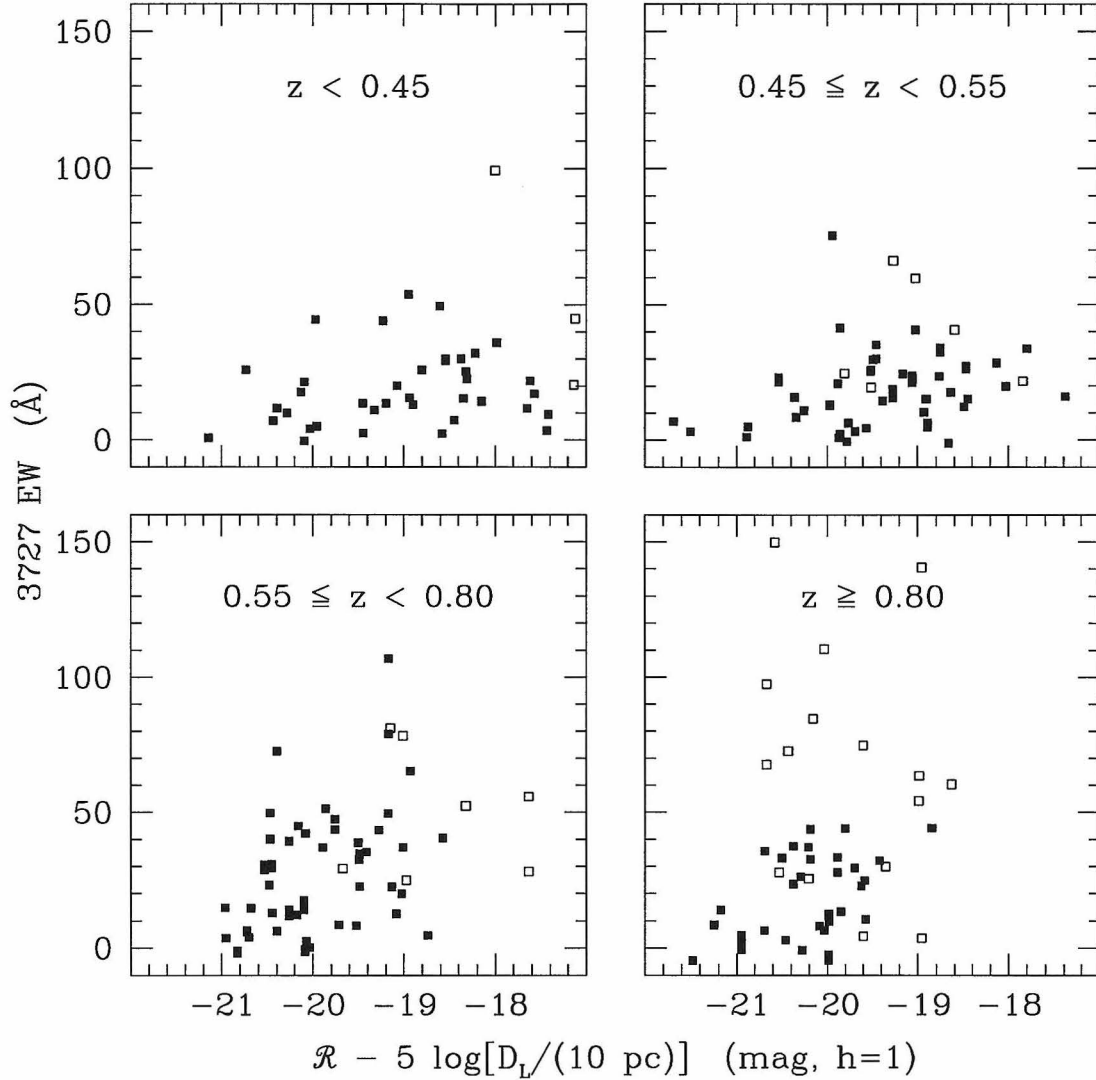


Figure 3.4: Rest-frame [O II] 3727 Å line equivalent widths plotted against crudely estimated \mathcal{R} -band absolute magnitude in four different redshift bins. Those spectra with continuum detections near rest-frame 3727 Å better than a signal-to-noise ratio of 2 (in one pixel) are plotted with solid squares; those with lower signal-to-noise are plotted with open squares.

Aug 27 10:05:06 1997

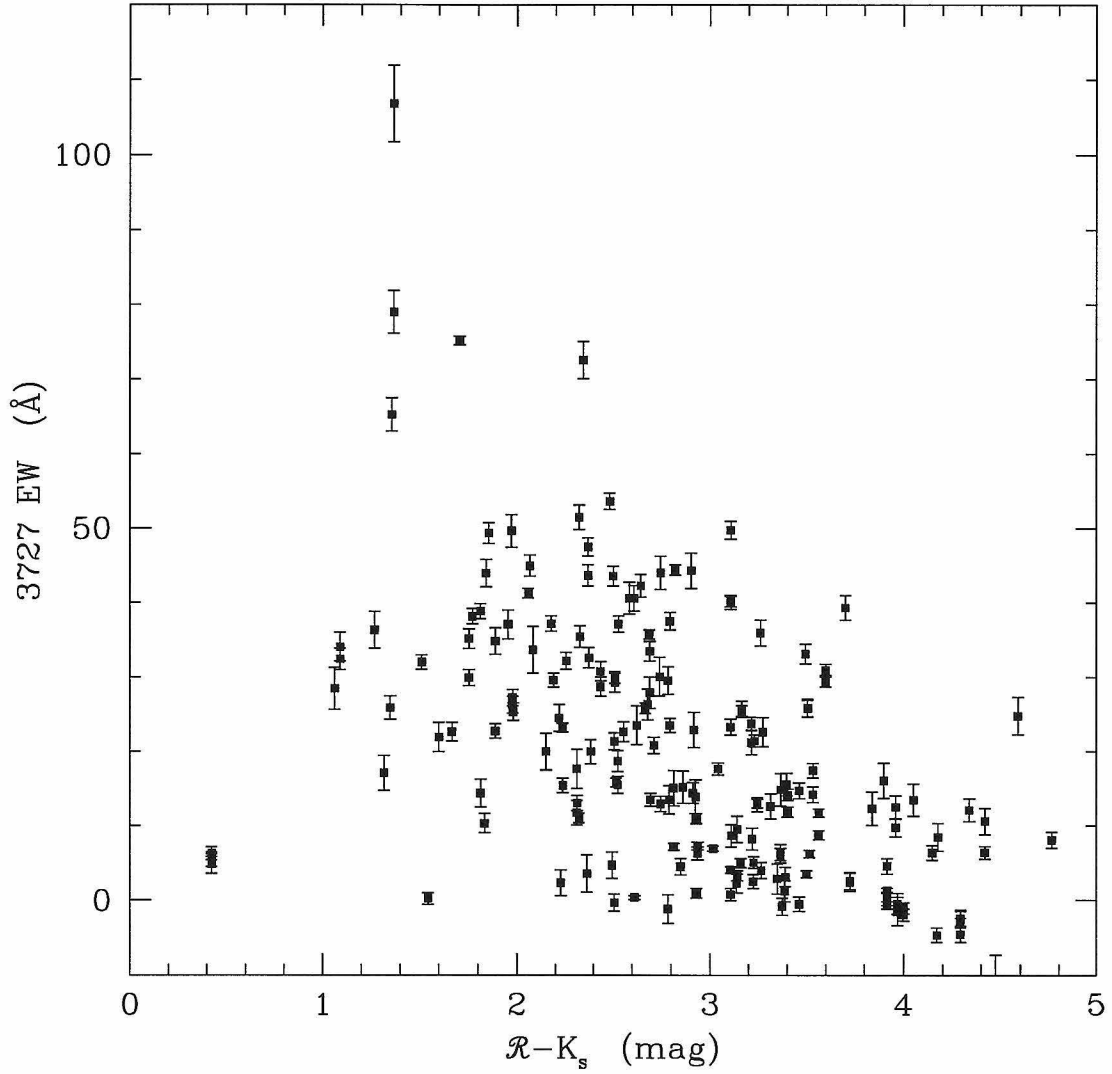


Figure 3.5: Rest-frame [O II] 3727 Å line equivalent widths plotted against $(\mathcal{R} - K_s)$ color. Only those spectra with continuum detections near rest-frame 3727 Å better than a signal-to-noise ratio of 2 (in one pixel) are plotted. Uncertainty estimates are described in Section 3.2.

Aug 27 10:06:59 1997

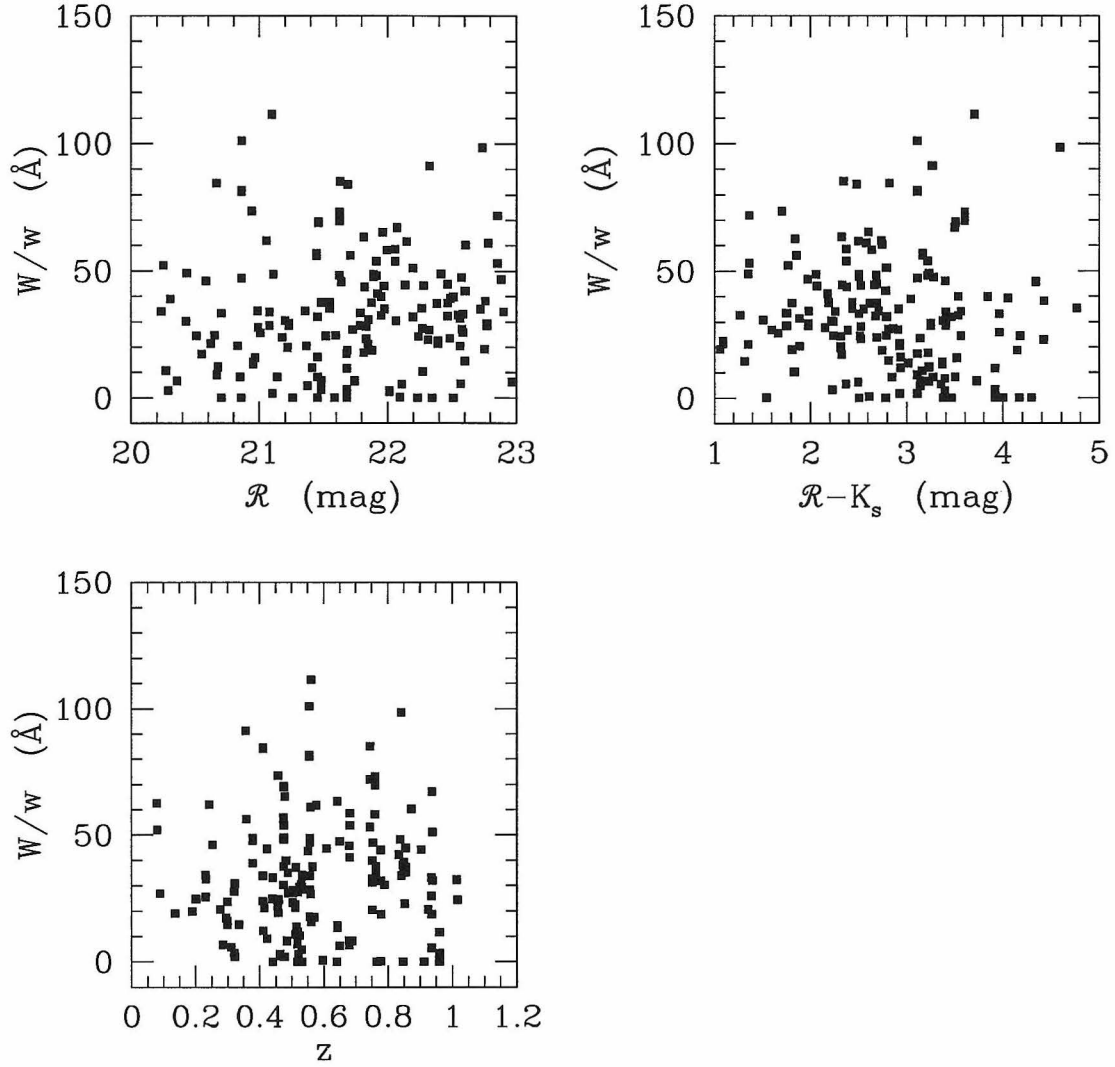


Figure 3.6: Scaled, rest-frame [O II] 3727\AA line equivalent widths W/w plotted against \mathcal{R} -band magnitude, $(\mathcal{R} - K_s)$ color, and redshift z . This demonstrates that the function w , defined in the text, with $a = 1$ and $b = 2$ does a reasonable job of removing correlations. Only those spectra with continuum detections near rest-frame 3727\AA better than a signal-to-noise ratio of 2 (in one pixel) are plotted.

Aug 28 21:40:04 1997

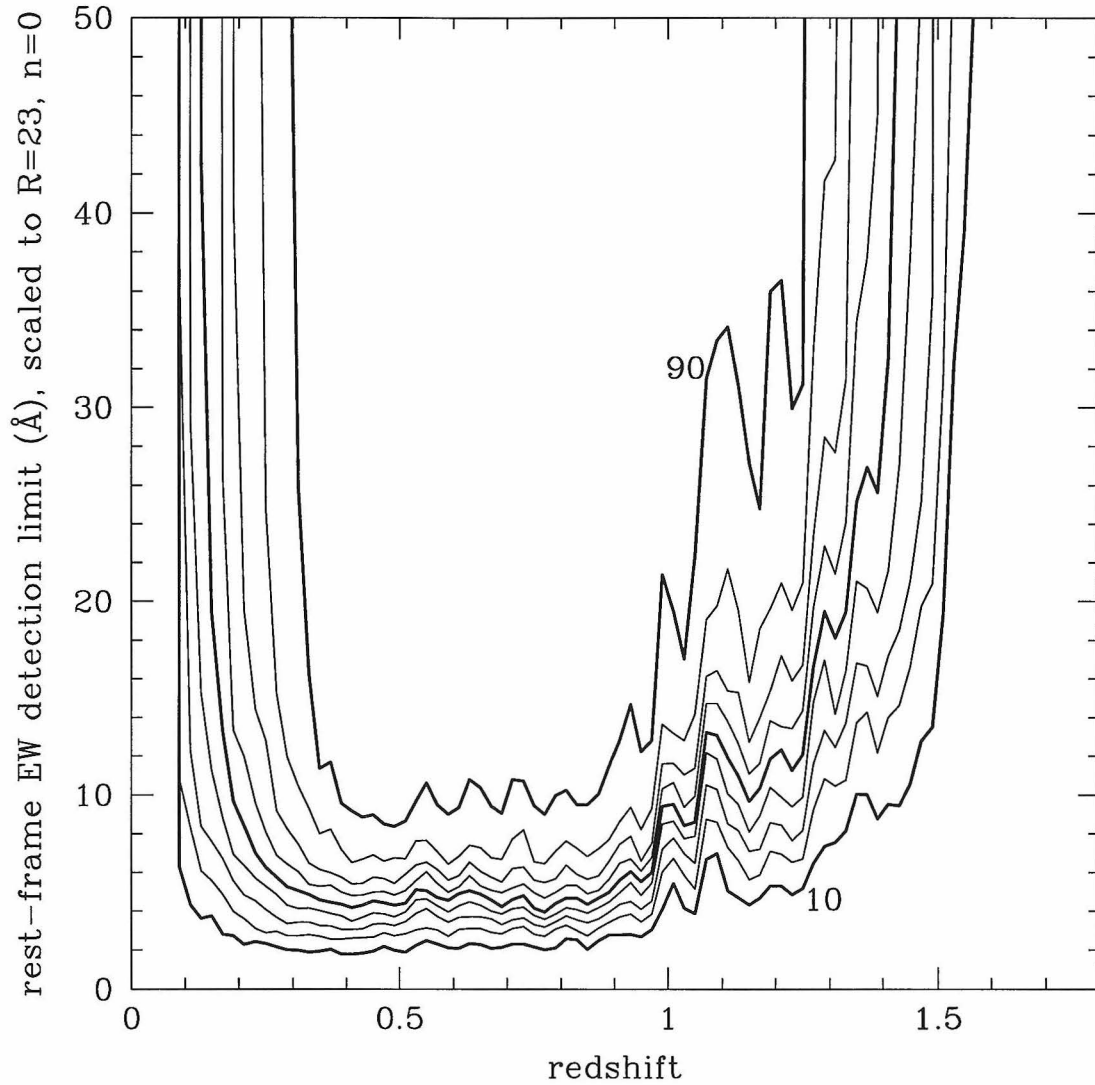


Figure 3.7: The cumulative distribution of scaled sensitivities to $[\text{O II}] 3727 \text{ \AA}$ emission, in terms of rest-frame equivalent width. The dark lines are the 10, 50, and 90 percent contours and the thin lines are spaced by 10 percent. The sensitivities are scaled to $\mathcal{R} = 23 \text{ mag}$ and $n = 0$ (flat spectrum in νf_ν) as described in the text.

Aug 28 21:49:10 1997

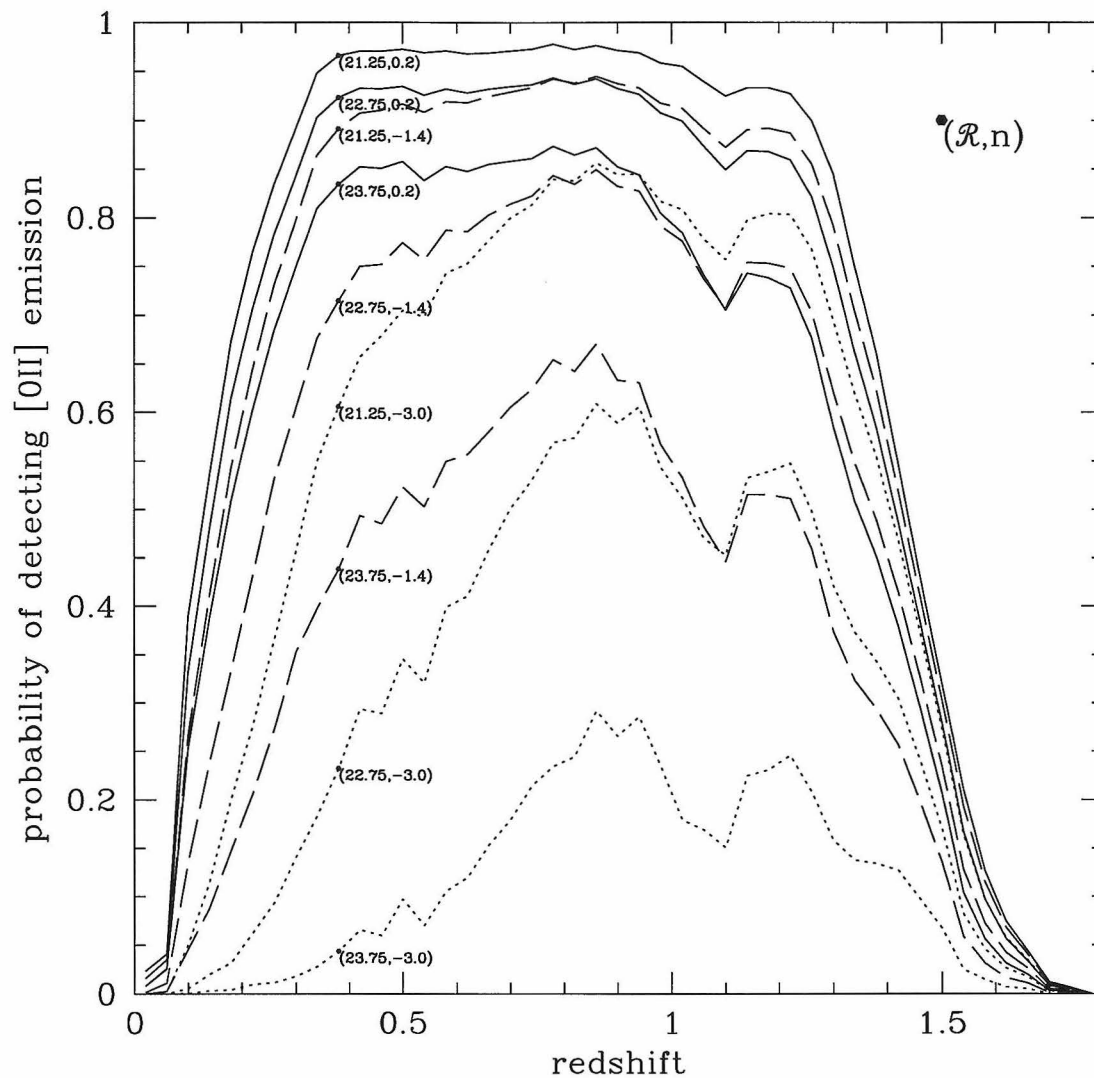


Figure 3.8: The probability of detecting [O II] 3727 Å emission, as a function of redshift, for a number of different magnitudes and spectral indices (colors). The three solid lines are for magnitudes $\mathcal{R} = 21.25, 22.75,$ and 23.75 mag (top to bottom) and spectral index $n = 0.2$, the three dashed lines are for the same magnitudes but $n = -1.4$ and the three dotted are for $n = -3.0$.

Sep 30 08:53:05 1997

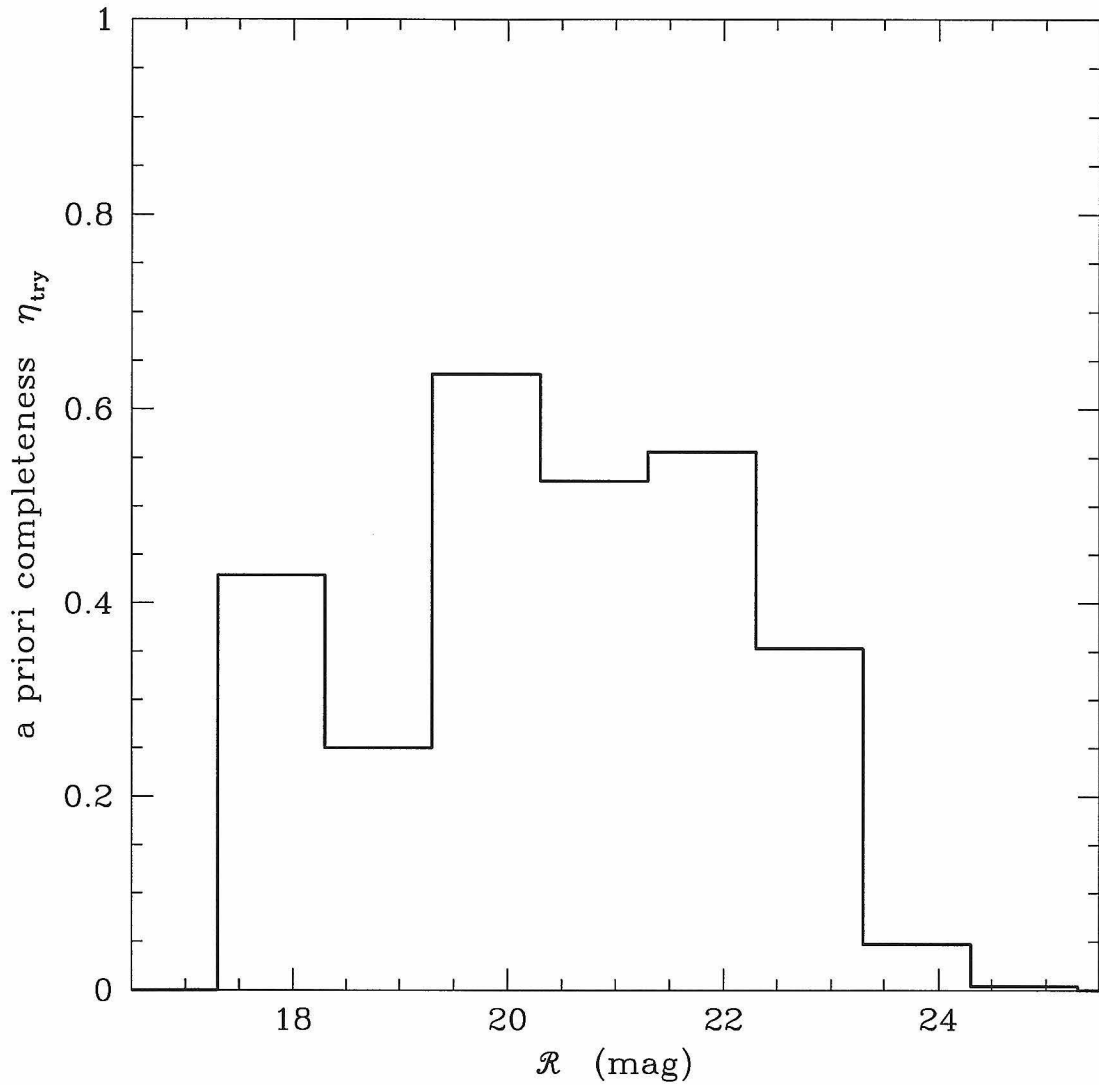
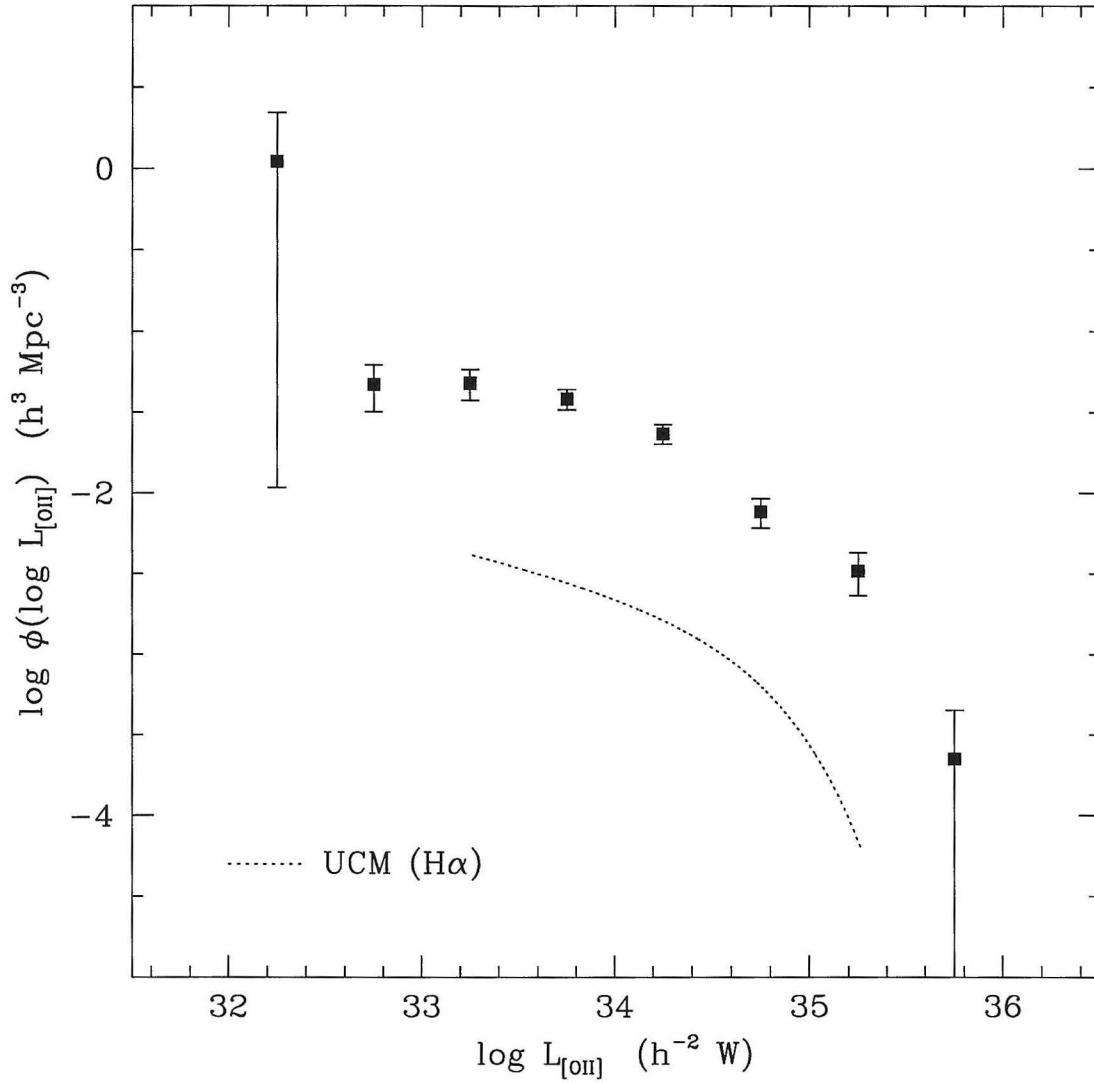
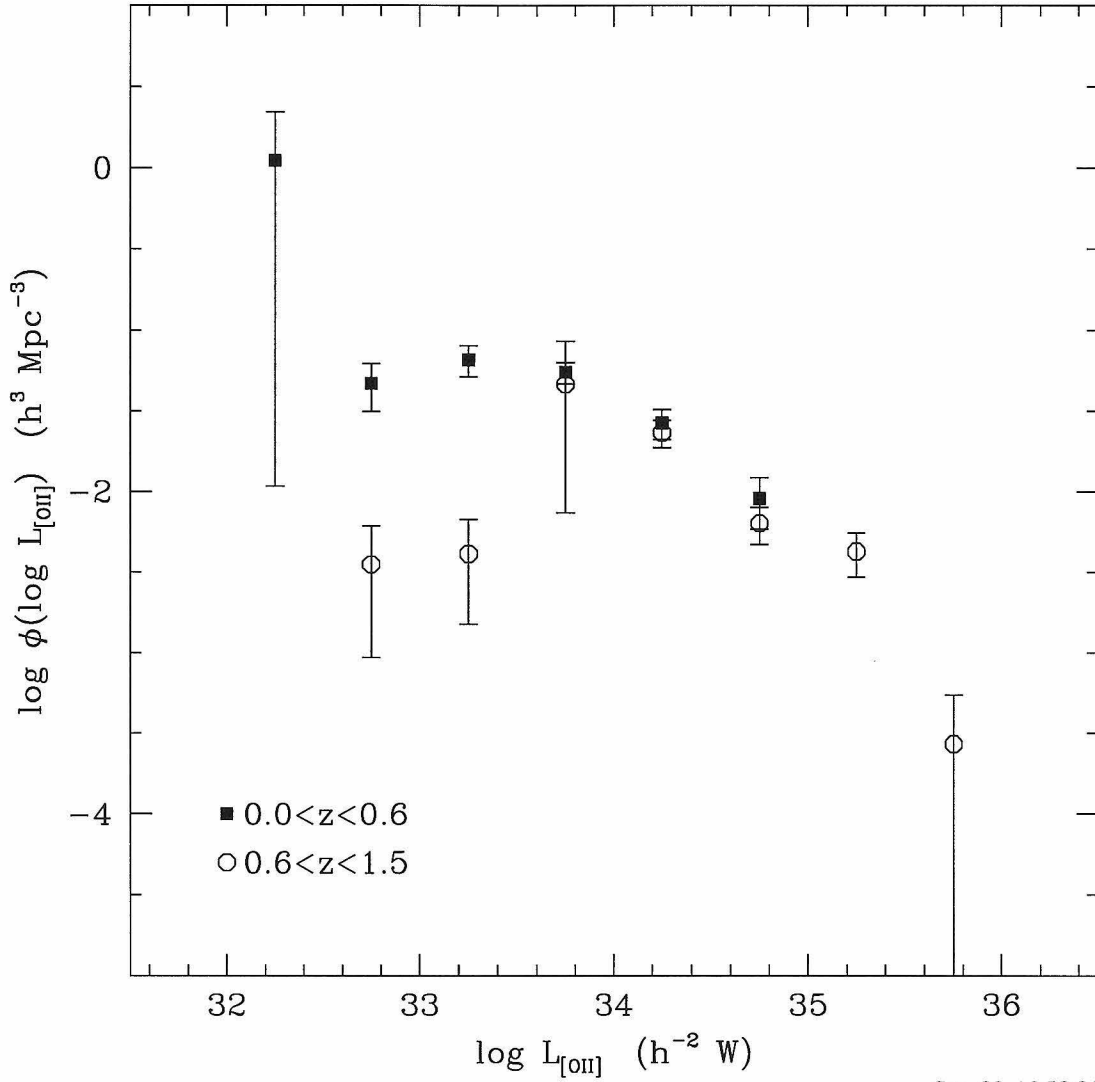


Figure 3.9: The probability, as a function of \mathcal{R} -band flux, that a source in the 8-arcmin diameter HDF sample was observed spectroscopically as part of the sample used in this Chapter for the [O II] line property studies. *I.e.*, this function is the fraction of sources in the field which were observed spectroscopically. The completeness is only around a half because it is only a subsample of the total sample used in, say, Chapter 5. The completeness drops rapidly at $\mathcal{R} = 23.3$ mag because observations fainter than this were only performed in the central, HST-imaged, 5 arcmin² of the field.



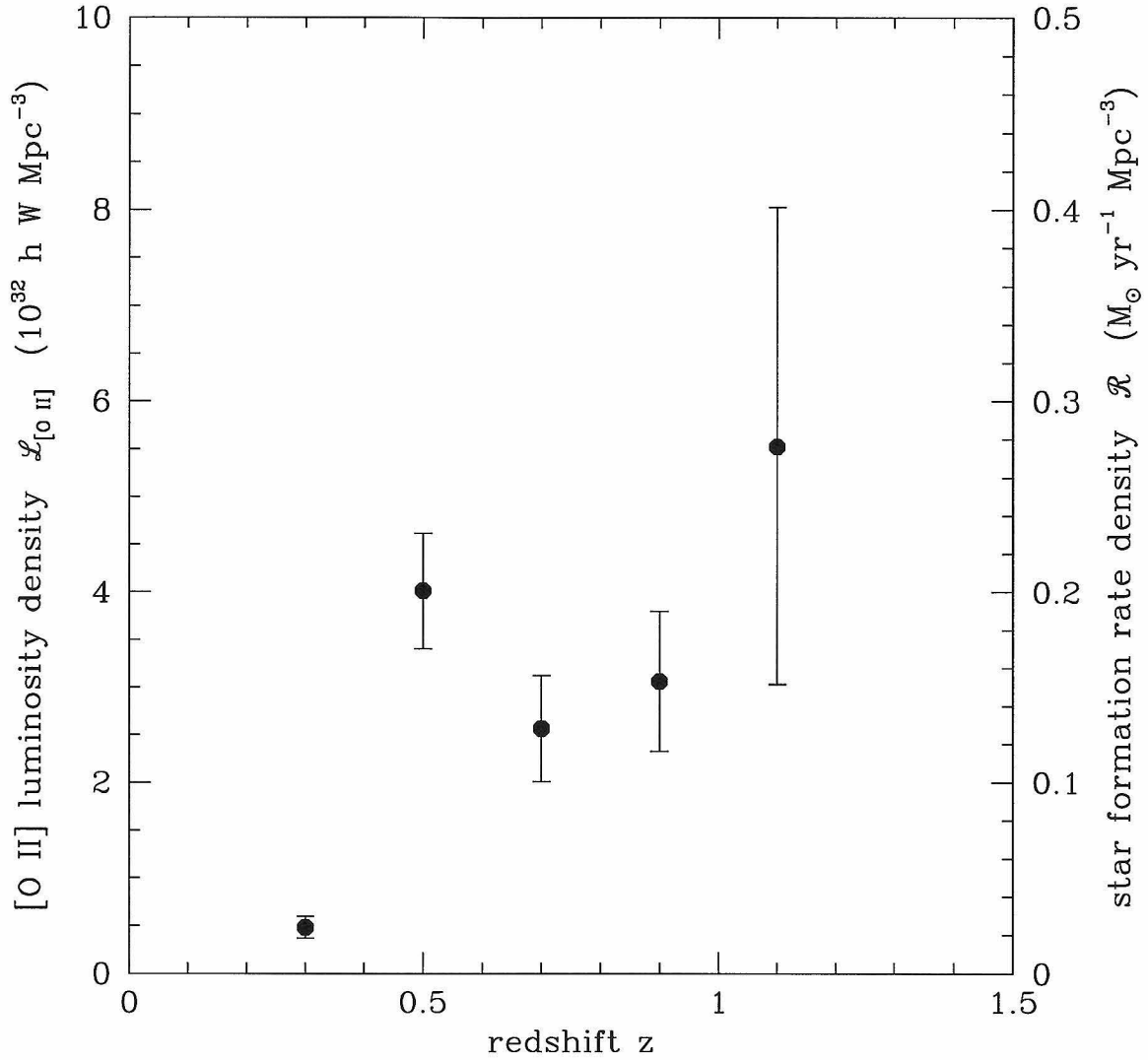
Oct 1 12:09:48 1997

Figure 3.10: The [O II] 3727 Å luminosity function, determined from the whole sample used in this Chapter. The luminosities, luminosity function points, and uncertainties are computed as described in the text. The dotted line shows the Schechter-function fit to the H α luminosity function from the UCM survey (Gallego *et al.* 1995), in the range in which it was determined, converted to the equivalent [O II] luminosity function with the conversion factor $L_{[\text{O II}]} / L_{\text{H}\alpha} = 0.46$, correct for the local Universe (Kennicutt 1992).



Sep 30 16:53:21 1997

Figure 3.11: The dependence of the [O II] 3727 Å luminosity function on redshift, derived from two subsamples of the sample used in this Chapter, split at redshift $z = 0.6$. The significance of the difference between the derived luminosity functions is discussed in the text.



Oct 2 12:46:49 1997

Figure 3.12: The [O II] 3727 Å luminosity and star formation rate densities as a function of redshift. The luminosity density is computed as described in the text and the star formation rate density is computed from it using the local calibration (Kennicutt 1992).

Chapter 4 Determination of the galaxy luminosity function from an incomplete redshift survey

4.1 Introduction

Although in principle it is straightforward to compute the luminosity function of galaxies, given a fairly complete sample of redshifts, there are large disagreements among the recent determinations. This is particularly strange because many of the surveys are selected, performed and analyzed in very similar ways. Of course, there are many difficulties with creating a large, uniform, complete galaxy catalog, especially if object detection or photometry is performed with photographic plate material, if there are strong surface-brightness selection effects, either in source detection or in spectroscopy, or if data are being combined which were taken under a wide range of conditions, with a number of very different instruments, or over a large fraction of the sky. Unfortunately, the calculation of the luminosity function is only trivial when a survey is complete, because only then is it easy to compute the effective volume of the Universe in which each survey object could lie and still make it into the survey criteria. Without completeness, the survey criteria become fuzzy or probabilistic, often depending on factors which are difficult to measure or quantify. The purpose of this Chapter is to develop and test methods for determining the luminosity function with incomplete surveys.

The standard parameterization of the galaxy luminosity function $\phi(L)$ (number of galaxies per unit luminosity per unit volume, as a function of luminosity L) is that

suggested by Schechter (1976), to wit

$$\phi(L) = \frac{\phi^*}{L^*} \left(\frac{L}{L^*} \right)^\alpha e^{-L/L^*} \quad (4.1)$$

where ϕ^* is a characteristic number density, L^* is a characteristic luminosity, and α is a “slope,” parameterizing the faint-end dependence as a power law. In terms of these parameters, the results of various recent luminosity function determinations are given in Table 4.1, including the wavelength of the determination and the mean redshift of the survey. The L^* values have been converted to νL_ν , power per decade in frequency, which can be justified by the fact that in all bands from B to K , the L^* values are similar in νL_ν ; or, bright galaxies have roughly constant νL_ν spectral energy distributions. An alternative to the Schechter function is the double power-law; *i.e.*, $\phi(L) \propto L^\alpha$ for luminosities fainter than a break luminosity \tilde{L} and $\phi(L) \propto L^\beta$ brighter. The double power-law does in fact fit most luminosity functions in the literature, and is the only type of function which fits the 60 μm luminosity function from the IRAS Bright Galaxy Survey (Soifer *et al.* 1985). Only the Schechter function is considered in this Chapter.

4.2 Luminosity estimation

Before luminosity function estimation comes luminosity estimation.

For the purposes of simplicity, in this Chapter, it is assumed that a galaxy’s properties are totally specified by a flux S defined to be energy per unit area per decade in frequency or $S \equiv \nu S_\nu$, measured through an aperture of fixed angular size (and possibly corrected with some kind of “aperture correction,” a spectral index n defined by $\nu S_\nu \propto \nu^n$ (this is a non-standard definition), and a redshift z . The inferred luminosity L of that object is then

$$\log L(S, n, z) = \log S + \log(4\pi) + 2 \log d_L(z) - n \log(1 + z) \quad (4.2)$$

where clearly we are using total luminosities, not luminosities per steradian, and d_L

is the luminosity distance, defined and computed in Appendix B. When numbers are given, they are given in SI units, so fluxes in W m^{-2} , luminosities in W, and distances in m. The Hubble constant is set to $100 h \text{ km s}^{-1} \text{ Mpc}^{-1}$ and, except where stated otherwise, an Einstein-de Sitter Universe ($\Omega_M = 1$ and $\Omega_\Lambda = 0$; Appendix B) is assumed.

This characterization of objects in terms of just (S, n, z) is clearly incomplete and incorrect at some level. After all, galaxies have different morphological types and central surface brightnesses, both of which come into completeness functions and photometric measurement schemes. In particular, when fluxes are measured out to a limiting isophote, the relationship between measured flux and true luminosity is non-trivial because there is a wide range of galaxy surface brightnesses and surface-brightness varies strongly with redshift. This can lead to biases in luminosity function determinations (Dalcanton, in preparation). When fluxes are aperture fluxes, the changing metric size with redshift of an aperture of fixed angular size can lead to similar problems, although they are generally not as acute.

Another problem with the simplistic (S, n, z) characterization is that galaxy spectra are by no means well-described by power-laws and more realistic spectral energy distributions, including spectral features and curvature, augmented by multi-band photometry, ought to be employed.

None of the simplifications employed in this Chapter are limitations in principle with the methods given below; it is easy to generalize the formula for $\log L(S, n, z)$ to include more complicated spectral energy distributions, and to include a model of the photometric measurement scheme, including aperture or isophotal corrections which vary with redshift. Furthermore, galaxies can be split up by morphological type, redshift range, environment, or any other characteristic, with only trivial modifications to the methods.

4.3 Completeness functions

In analyzing a redshift survey, there are two qualitatively distinct types of incompleteness which must be taken into account. The first is the *a priori* selection function η_{try} which describes the sample of galaxies by giving the fraction (< 1) of galaxies with certain photometric parameters (which can include flux, color, morphology, etc.) for which the observer attempted to obtain a redshift. Since in very faint work, where telescopes are being pushed to their limits, the surveys are not necessarily simply flux-limited, this can be a complicated function, which might depend on broadband color, morphological properties, central surface brightness, or position in the field, in addition to flux. Often not all these possibilities are considered in analyzing redshift surveys, so η_{try} is not usually known as accurately as it ought to be. However, since this *a priori* selection function is the method by which the observer (consciously or unconsciously) selects objects for spectroscopy, it cannot depend on galaxy redshift directly; it is based only on photometric observables, which are measured before the spectroscopy. For this reason, even in a sample which is substantially incomplete, η_{try} can be known very accurately because the survey selection procedure can be fully modeled or even simulated.

For example, η_{try} can be estimated for the Caltech faint galaxy redshift survey in the HDF (Cohen *et al.* 1996b; Cohen *et al.* in preparation) by comparing the full \mathcal{R} -selected galaxy sample to the subset which was spectroscopically observed. This calculation is done in Chapter 5.

The second and more difficult selection function describes, of the set of galaxies for which redshift determinations are attempted, what fraction will actually be successful. Unfortunately, in contrast to the *a priori* completeness function, this *a posteriori* completeness function η_{got} cannot be known exactly because it depends on the galaxy redshifts, and on the strengths of their spectral features, necessarily for those sources for which no spectral features or redshifts have been measured! With some assumptions about galaxy properties and an instrument model, however, it is possible to estimate this *a posteriori* completeness function by simulating or modeling

the procedure by which redshifts are obtained. This procedure does not necessarily involve wild speculation or extrapolation because unless the sample is tremendously incomplete, assumptions will only need to be made over a small part of the flux-redshift plane. Of course η_{got} may end up being a very complicated function which depends on color, morphology and surface brightness, not just flux and redshift.

One estimate of η_{got} is provided in part by the probability, computed in Chapter 3, of detecting the [O II] 3727 Å line as a function of galaxy flux, index and redshift. This probability function is relevant because most high-redshift ($z > 0.6$) galaxies have their redshift identifications based primarily or totally on this line. At lower redshifts, there are several lines, including the [O III] lines and H α and H β , along with the 4000 Å break, which can be used for redshift identification. For the purposes of this Chapter, we adopt the optimistic estimate of the *a posteriori* completeness function η_{got} that it is unity for $z < 0.6$ and simply the probability of detecting the [O II] line for $z > 0.6$. This probability function is shown in Figure 3.8 of Chapter 3.

4.4 Luminosity function determination methods

In this Section, the standard V-max and STY methods for estimating the galaxy luminosity function are reviewed and generalized to include the completeness functions described above. The ASF and BFR methods, new maximum-likelihood methods complementary to the STY method, are introduced. Their advantages and disadvantages relative to STY are mentioned, but the real analysis of the methods is left for later Sections.

4.4.1 Generalized V-max method

If one is blessed with a photometrically complete sample with perfect flux limits, the luminosity function $\phi(L_i)$ in luminosity bin i can be estimated by summing up the inverse “volumes” of all the objects in the sample which have inferred luminosities falling in bin i . This method owes its origins to the V/V-max test for evolution first applied to quasars (Schmidt 1968). The “volume” V_{max} associated with an object is

the total comoving volume of the Universe in which that object could lie such that it would still be included in the sample. The boundaries are set by the solid angular coverage of the survey, and the range of redshift such that the galaxy satisfies the flux limits of the survey. If the sample is incomplete, the quantity equivalent to V_{\max} is given by

$$V_{\max} = \int_0^{\infty} \eta_{\text{try}}(S(L, n, z'), n) \eta_{\text{got}}(S(L, n, z'), n, z') \frac{dV_{z'}}{d\Omega dz'} \Delta\Omega dz' \quad (4.3)$$

where z' is an integration variable, $S(L, n, z')$ is the flux expected for an object of that luminosity at redshift z' , $dV_z/(d\Omega dz')$ is the comoving volume element per unit solid angle per unit redshift, evaluated at redshift z' , and $\Delta\Omega$ is the solid angle of the survey. Usually, when the V-max method is described, the upper limit of the integral is set to the redshift at which the galaxy would no longer make it into the sample, but in this case, the function η_{try} in effect serves the purpose of setting the limits of the integral, as it vanishes when the object lies outside of the survey criteria.

The estimate of the number density of sources in a luminosity bin of width $\Delta(\log L)$ centered on luminosity $\log L_i$ is simply the sum of the inverse volumes $1/V_{\max}$ of all the sources with luminosities in the bin. The luminosity function value in that bin is just

$$\phi(\log L_i) = \frac{1}{\Delta(\log L)} \sum_{|\log L_j - \log L_i| < \Delta(\log L)} \frac{1}{V_{\max, j}} \quad (4.4)$$

where index i labels luminosity bins and index j labels galaxies. The variances are computed by summing the squares of the inverse volumes; the square roots of the variances can be used as one-sigma error bars.

Sometimes arbitrary redshift cutoffs are imposed in addition to the flux cutoffs in order to split a sample in search of evolution in the luminosity function (*e.g.*, Eales 1993). In this case, the equation for V_{\max} becomes

$$V_{\max} = \int_{z_{\min}}^{z_{\max}} \eta_{\text{try}}(S(L, n, z'), n) \eta_{\text{got}}(S(L, n, z'), n, z') \frac{dV_{z'}}{d\Omega dz'} \Delta\Omega dz' \quad (4.5)$$

4.4.2 Generalized STY method

Because usually the number of objects is small in studies of the luminosity function at high redshift and because it is important to understand the confidence with which conclusions are drawn, Bayesian or maximum likelihood methods are preferred over constructive methods such as the V-max method. The standard is the STY method (Sandage *et al.* 1979), which is based on estimating, for each object in the survey, the likelihood $f(\log S|z)$ that it would have its observed flux $\log S$ given its redshift z and the flux limit S_{\min} of the survey, within the context of an individual luminosity function model

$$f_{\vec{a}}(\log S|n, z) = A(n, z) \phi_{\vec{a}}(\log L(S, n, z)) \eta_{\text{try}}(S, n) \eta_{\text{got}}(S, n, z) \quad (4.6)$$

where $\phi(\log L)$ is the luminosity function (number per unit comoving volume per unit log luminosity), \vec{a} contains all the luminosity function parameters, and $A(n, z)$ is a normalization constant given by

$$\frac{1}{A(n, z)} = \int_{-\infty}^{\infty} d \log S \phi_{\vec{a}}(\log L(S, n, z)) \eta_{\text{try}}(S, n) \eta_{\text{got}}(S, n, z) \quad (4.7)$$

Note that $f_{\vec{a}}(\log S|n, z)$ has “dimensions” of inverse log flux.

The product of all the individual likelihoods $f_{\vec{a}}(\log S_i|n_i, z_i)$ for all objects i is treated as a likelihood $\mathcal{L}_{\vec{a}}$ for the model with parameters \vec{a} . Different models are compared on the basis of this total likelihood $\mathcal{L}_{\vec{a}}$. I call this method “generalized STY” (though hereafter simply “STY”) because the description here of the STY method does not depend on having a photometrically complete sample as the first descriptions of STY method did (Sandage *et al.* 1979; Efstathiou *et al.* 1988). Of course the method requires good estimates of the completeness functions η_{try} and η_{got} if the sample is significantly incomplete. Logarithmic quantities $\log S$ and $\log L$ are used rather than S and L ; this makes small differences to the inferred luminosity function parameters because it changes the “metric” of the data space (recall that all maximum-likelihood techniques are biased). However, the differences go to zero as

the number of galaxies in the sample increases.

One significant disadvantage of this and the following maximum-likelihood methods is that they use only the distribution of galaxies and not their total number. This means that one needs to look at the total galaxy counts (number per log flux per solid angle) in order to normalize the derived luminosity function $\phi(\log L)$.

The STY method is odd in that it treats the redshift as the primary observable, and the flux secondary, *i.e.*, one considers the probability of getting the flux given the redshift, while the objects in redshift surveys are selected on the basis of flux. Of course the reason for the popularity of the STY method is that it is insensitive to large-scale structure in the form of variations in the density in redshift space away from the homogeneous prediction that it ought to be proportional to the comoving volume element. However, this feature of the STY method is also in some cases a drawback. For example, the STY method is totally insensitive to density evolution models, in which the normalization (but not the shape) of the luminosity function varies with redshift. It is insensitive to this kind of evolution because it only considers the flux distribution at a given redshift, never comparing different redshifts. Since in some investigations density evolution is important, methods complementary to STY are necessary.

4.4.3 ASF method

For these reasons, I introduce a new technique to which I will refer as the “arbitrary selection function” (ASF) technique. This is similar to STY in that it is a maximum likelihood technique, except that it treats flux as the primary observable. Under the ASF method, for each object in the survey, the likelihood that it has redshift z given that it has flux S and index n is computed in the context of an individual luminosity function model. Actually, for technical and pedagogical reasons, the likelihood will be computed in terms not of the redshift z , but rather of the comoving volume V_z (Appendix B) corresponding to that redshift; *i.e.*, we are using V_z rather than z as the line-of-sight distance measure. (Do not confuse V_z with V_{\max} .) The ASF method

makes no reference to the limiting depth of the survey or even selection technique, so η_{try} factors out. This can be very useful if a survey has complicated selection criteria or if it is selected in a photometric band other than that in which the luminosity function is being computed.

The likelihood $f_{\vec{a}}(V_z|S, n)$ for an object to lie at comoving volume V_z given that it has flux S and spectral index n , in the context of a model parameterized by \vec{a} (the components of \vec{a} include all the luminosity function parameters) is given by

$$f_{\vec{a}}(V_z|S, n) = A(S, n) \phi_{\vec{a}}(\log L(S, n, z)) \eta_{\text{got}}(S, n, z) \quad (4.8)$$

where $A(S, n)$ is a normalization constant given by

$$\frac{1}{A(S, n)} = \int_0^\infty dz' \frac{dV_{z'}}{dz'} \phi_{\vec{a}}(\log L(S, n, z)) \eta_{\text{got}}(S, n, z) \quad (4.9)$$

where $dV_{z'}/dz'$ is the comoving volume element evaluated at z' . Note that $f_{\vec{a}}(V_z|S, n)$ has “dimensions” of inverse volume, which is why, as mentioned above, this is a likelihood of getting comoving volume V_z , rather than z itself.

It is emphasized that the ASF method, as stated, does not depend on having a photometrically complete sample, because the conscious selection function η_{try} cannot depend on redshift (see above) and therefore does not enter into the likelihood function $f(V_z|S, n)$. This makes the ASF method ideal for determining constraints on luminosity function parameters with a small, oddly selected sample (*e.g.*, a dozen high redshift ellipticals selected on the basis of some complicated combination of radio flux, optical color and morphology). However, like the STY method, the ASF method does depend on having very little *a posteriori* incompleteness, or an *a posteriori* incompleteness function $\eta_{\text{got}}(S, n, z)$ which is very well understood.

Unfortunately, because it uses the comoving volume formulae, the ASF method is sensitive to strong redshift-space structures. On the other hand, this bug is also a feature because unlike STY, ASF can be used to measure density evolution if density evolution parameters are put into the luminosity function parameter set.

4.4.4 BFR method

Perhaps the strangest thing about the STY and ASF methods is that they hold one of the two crucial quantities, flux and redshift, fixed and ask what is the probability of getting the other. This means that a luminosity function determined by, say, STY method, which fits the distribution of fluxes at every redshift perfectly, will not necessarily fit the bivariate distribution of flux *and* redshift at all well. That is, an optimal methods ought really to use all of the information available. These considerations lead to another method, the “bivariate flux–redshift” (hereafter BFR) method which considers the joint probability $f(\log S, V_z|n)$ of getting the observed logarithmic flux and comoving volume (which is being used as the distance measure rather than redshift z), given its index n ,

$$f_{\bar{\alpha}}(\log S, V_z|n) = A(n) \phi_{\bar{\alpha}}(\log L(S, n, z)) \eta_{\text{try}}(S, n) \eta_{\text{got}}(S, n, z) \quad (4.10)$$

where $A(n)$ is a normalization constant given by

$$\frac{1}{A(n)} = \int_{-\infty}^{\infty} d \log S \int_0^{\infty} dz' \frac{dV_{z'}}{dz'} \phi_{\bar{\alpha}}(\log L(S, n, z)) \eta_{\text{try}}(S, n) \eta_{\text{got}}(S, n, z) \quad (4.11)$$

Note that $f(\log S, V_z|n)$ has dimensions of inverse log flux times inverse volume, which is the sense in which it is $f(\log S, V_z|n)$ rather than $f(\log S, z|n)$.

The BFR method is the most sensible in that it uses the flux and redshift distributions simultaneously. On the other hand, because a double integral is required to compute the normalization constant $A(n)$ for every source for every possible luminosity function model, the BFR method tends to be the most computationally intensive of the maximum-likelihood methods.

4.5 Simulated redshift surveys

In general, maximum likelihood estimators, such as the ASF, STY and BFR methods, are biased; the most secure method for determining bias is to simulate the data

and attempt to recover the input parameters to the simulation. Furthermore, it is claimed above that the ASF method does not depend on the existence of a photometrically complete sample. This claim, although not remarkable, will be treated with skepticism if not shown to be true in simulations.

Simulated galaxy catalogs were produced as follows: Because many of the objects in the observed sample are found to be in walls or peaks in the redshift distribution, the simulation of a single-field redshift survey begins with the choosing of a set of peak redshifts, separated by mean comoving distances of $0.09 D_H$ (Hubble distances; Appendix B). The peaks are chosen from the comoving distance distribution by acceptance-rejection method (*e.g.*, Press *et al.* 1992; see also the code in Appendix C). For each object, a redshift is either chosen at random from the comoving volume distribution or else one of the peak redshifts is chosen, with the probability of being in each peak weighted by its comoving area per unit solid angle. To emulate the true data, half the objects are assigned peak redshifts.

A luminosity L in the \mathcal{R} band is chosen from a Schechter function with $\log L^* = 37$ (in W m^{-2}), α ranging from 0.0 to -2.0 , and a low luminosity cutoff of $10^{-3} L^*$. These random distributions are produced with the “acceptance-rejection method.” An index n is chosen from a Gaussian distribution with mean $n = -1.6$ and variance $\sigma_n^2 = 0.83$. That this is a reasonable approximation to the color distribution in the HDF \mathcal{R} -selected sample is demonstrated in Figure 4.1. The redshift, luminosity and index are used to compute the flux S . Each galaxy is included in the catalog if $S_{\min} < S < S_{\max}$ and $z < 2$. The process is repeated until N_{gal} galaxies are in the catalog.

The *a priori* completeness function η_{try} is evaluated for each fake galaxy to find the probability it is observed spectroscopically. The function η_{try} is set to unity at $\mathcal{R} < 22$ mag, 0.8 at $22 < \mathcal{R} < 23$ mag, 0.1 at $23 < \mathcal{R} < 24$ mag, and zero fainter. This completeness function approximates the spectroscopic coverage of the Hubble Deep Field. For each galaxy a random number is drawn and used, along with the η_{try} value, to determine whether or not the galaxy is observed spectroscopically. The *a posteriori* completeness function η_{got} is evaluated for each fake galaxy to find the

probability, if it is observed, that its redshift is determined. The function η_{got} is assumed to be unity for sources at $z < 0.6$ and the probability, computed in the previous Chapter, of detecting [O II] 3727 emission for sources at $z > 0.6$, since most redshifts in this redshift range are based on this line. For each galaxy which is observed spectroscopically, a random number is drawn and used, along with the η_{got} value, to determine whether or not the galaxy redshift was successfully determined.

Two typical single-field simulations with $\alpha = -1.5$ are shown in Figures 4.2 and 4.3.

4.6 Tests

The generalized V-max method is used to infer the luminosity function from sets of 100 catalogs of 300 galaxies each, observed in the range $17 < \mathcal{R} < 23$ mag, drawn from luminosity functions with $L^* = 36.4$ and two different values of α . Both completeness functions described in Section 4.3 are used in both the simulations and analysis. The results are shown in Figure 4.4.

Several biases in the V-max method are noticeable. The steep luminosity function is underestimated at the faint end; *i.e.*, the V-max method returns a luminosity function less steep than the true function when the true function is in fact steep. On the other hand, the faintest points in the flat function tend to be overestimated. These points have no data in many of the analyses, because in many simulations there are no very low-redshift galaxies. For this reason, when there are low-redshift galaxies, the points tend to lie above the true luminosity function curve. This is a type of selection bias, which can lead to an artificial “upturn” at the faint end of the luminosity function if the true function is flat. Also noticeable on the diagram is the much greater constraints on the faint end of the luminosity function when it is steep. This is of course because a steep luminosity function contains far more faint galaxies! At the bright end, it appears that the inferred luminosity function drops more rapidly than the true function, when the true function is flat.

The STY, ASF and BFR methods are used to infer the luminosity function pa-

rameters $\log L^*$ and α from simulated catalogs, created as described in Section 4.5. The results of the tests are given in Tables 4.2 through 4.4 and the detailed results of one test are shown in Figures 4.5 and 4.6.

Table 4.2 shows the dependence of the maximum likelihood results as a function of the number N_{gal} of galaxies in the sample, for a luminosity function with $\log L^* = 37$ and $\alpha = -1.5$. All methods find a mean $\alpha \approx -1.4$, *i.e.*, they are biased, and interestingly the bias does not seem to depend on the number N_{gal} of galaxies in the sample. The scatter in inferred quantities does decrease as N_{gal} increases, although more for the STY method than the others. It appears that BFR is the best method when the number N_{gal} is small (< 300) and STY is best for larger N_{gal} .

Table 4.3 shows the dependence of the results on input faint-end slope α . At $\alpha < -1.25$, all the methods are similarly biased towards flatter α , and also correspondingly lower L^* . This Table thus provides corrections which can be applied to luminosity function results with steep faint-end slope. All the methods work well at $\alpha \geq -1.25$. It has been claimed that the STY method has no important biases (Efstathiou *et al.* 1988) but that work did not consider $\alpha < -1$; the other study which considers $\alpha < -1$ does find this bias (Willmer 1997).

Table 4.4 demonstrates that the methods can all be used to look for evolution in the luminosity function by splitting a sample in redshift. When there is a difference in luminosity function, the methods find it and when there isn't, they do not provide a false positive. This is true even if the sample is analyzed with an incorrect world model, as Table 4.4 shows, in the sense that the faint-end slope is not mis-estimated simply because the world model is incorrect. Of course the inferred L^* is slightly affected by changing world model, because sources get closer or further away as the world model is changed. The high-redshift samples have poorly determined faint-end slopes α (in the sense of large scatter) because at high redshift low-luminosity sources fall below the flux limits of the survey.

Note that ASF method works comparably with the others despite the fact that it makes no use of the *a priori* completeness function η_{try} .

References

- Cohen J. G., Hogg D. W., Pahre M. A. & Blandford R., 1996, Strong redshift clustering of distant galaxies, *ApJ* 462 L9
- Eales S., 1993, Direct construction of the galaxy luminosity function as a function of redshift, *ApJ* 404 51
- Efstathiou G., Ellis R. S. & Peterson B. A., 1988, Analysis of a complete galaxy redshift survey II: The field-galaxy luminosity function, *MNRAS* 232 431
- Ellis R. S., Colless M., Broadhurst T., Heyl J. & Glazebrook K., 1996, Autofib Redshift Survey I: Evolution of the galaxy luminosity function, *MNRAS* 280 235
- Gardner J. P., Sharples R. M., Frenk C. S., Carrasco B. E., 1997, A wide-field K-band survey: The luminosity function of galaxies, *ApJ* 480 L99
- Glazebrook K., Ellis R., Colless M., Broadhurst T., Allington-Smith J. & Tanvir N., 1995b, A faint galaxy redshift survey to $B = 24$, *MNRAS* 273 157
- Lin H., Kirshner R. P., Shectman S. A., Landy S. D., Oemler A., Tucker D. L. & Schechter P. L., 1996, The luminosity function of galaxies in the Las Campanas Redshift Survey, *ApJ* 464 60
- Lin H., Yee H. K. C., Carlberg R. G. & Ellingson E. E., 1997, The luminosity function of field galaxies in the CNOC1 redshift survey, *ApJ* 475 494
- Loveday J., Peterson B. A., Efstathiou G. & Maddox S. J., 1992, The Stromlo-APM Redshift Survey I: The luminosity function and space density of galaxies, *ApJ* 390 338
- Marzke R. O., Huchra J. P. & Geller M. J., 1994, The luminosity function of the CfA redshift survey, *ApJ* 428 43
- Oke J. B. *et al.*, 1995, The Keck Low-Resolution Imaging Spectrometer, *PASP* 107 375
- Press W. H., Teukolsky S. A., Vetterling W. T. & Flannery B. P., 1992, *Numerical Recipes in C*, 2ed, Cambridge University Press, Cambridge UK
- Ratcliffe A., Shanks T., Parker Q. A. & Fong R., 1997, The Durham/UKST Galaxy Redshift Survey II: The field galaxy luminosity function, *MNRAS* in press
- Sandage A., Tammann G. A. & Yahil A., 1979, *ApJ* 232 352
- Schechter P., 1976, An analytic expression for the luminosity function for galaxies, *ApJ* 203 297
- Schmidt M., 1968, Space distribution and luminosity function of quasi-stellar radio sources, *ApJ* 151 393
- Willmer C. N. A., 1997, Estimating galaxy luminosity functions, *AJ* in press

paper	band ($\log \nu$) — (s^{-1})	$\langle z \rangle$ —	ϕ^* ($10^8 [c/H_0]^{-3}$)	$\log L^*$ ($h^{-2} \text{W}$)	α —
Efstathiou <i>et al.</i> 1988	B_T (14.83)	0.06	4.2 ± 0.9	36.43 ± 0.04	-1.07 ± 0.05
Loveday <i>et al.</i> 1992	B_J (14.83)	0.1	3.8 ± 0.5	36.32 ± 0.05	-0.97 ± 0.15
Mobasher <i>et al.</i> 1993	K (14.13)	?	3.0 ± 0.4	36.48 ± 0.12	-1.0 ± 0.3
Marzke <i>et al.</i> 1994	Z (14.83)	?	10.8 ± 2.7	36.04 ± 0.12	-1.0 ± 0.2
Lin <i>et al.</i> 1996	r (14.66)	0.1	5.1 ± 0.3	36.34 ± 0.01	-0.70 ± 0.05
Lin <i>et al.</i> 1997	r (14.66)	0.4	?	36.54 ± 0.16	-1.3 ± 0.2
Lin <i>et al.</i> 1997	B_{AB} (14.83)	0.4	?	36.31 ± 0.12	-0.9 ± 0.2
Gardner <i>et al.</i> 1997	K (14.13)	?	$4.5 \pm ?$	36.29 ± 0.07	-0.91 ± 0.2
Ratcliffe <i>et al.</i> 1997	B_J (14.83)	0.05	4.6 ± 0.8	36.39 ± 0.04	-1.04 ± 0.08

Table 4.1: A comparison of recent luminosity function determinations, including wavelength bands (and corresponding frequencies $\log \nu$) of the determinations and the approximate mean redshifts $\langle z \rangle$ of the surveys. The luminosity function parameters ϕ^* , L^* and α are the standard Schechter (1976) parameters (see text). Number densities ϕ^* have been converted from what is usually Mpc^{-3} to $10^8 (c/H_0)^{-3}$, *i.e.*, 10^8 “inverse Hubble Volumes” (Appendix B) so as to be free of Hubble constant uncertainties. What are usually given as absolute magnitudes M^* have been converted into luminosities $L^* \equiv \nu L_\nu^*$ in W with Hubble constant $100 h^{-1} \text{ km s}^{-1} \text{ Mpc}^{-1}$ by the conversions given in Appendix A. In the absense of better calibration, it has been assumed that $B_T = B$, $Z = B_J$, and the strange photometry described in Lin *et al.* 1996 corresponds to r . Question marks indicate that the quantity is not clearly reported.

run	simulations			$(\Omega_M, \Omega_\Lambda)$	analyses		α
	N_{try} N_{gal}	$(\Omega_M, \Omega_\Lambda)$ $(z_{\text{min}}, z_{\text{max}})$	$\log L^*$ α		method	$\log L^*$	
0820	200	(1.0,0.0)	37.00	(1.0,0.0)	STY	36.96 ± 0.16	-1.45 ± 0.11
	150	(0.0,1.5)	-1.50		ASF	36.91 ± 0.15	-1.42 ± 0.09
					BFR	36.91 ± 0.15	-1.42 ± 0.08
0818	100	(1.0,0.0)	37.00	(1.0,0.0)	STY	36.97 ± 0.12	-1.47 ± 0.08
	300	(0.0,1.5)	-1.50		ASF	36.93 ± 0.10	-1.43 ± 0.07
					BFR	36.92 ± 0.10	-1.43 ± 0.07
0819	50	(1.0,0.0)	37.00	(1.0,0.0)	STY	36.96 ± 0.09	-1.45 ± 0.06
	600	(0.0,1.5)	-1.50		ASF	36.92 ± 0.10	-1.43 ± 0.06
					BFR	36.92 ± 0.10	-1.43 ± 0.06
0911	25	(1.0,0.0)	37.00	(1.0,0.0)	STY	36.96 ± 0.07	-1.45 ± 0.04
	1200	(0.0,1.5)	-1.50		ASF	36.92 ± 0.09	-1.41 ± 0.08
					BFR	36.92 ± 0.09	-1.41 ± 0.07

Table 4.2: A comparison of luminosity function determination methods, as applied to sets of simulated galaxy redshift survey catalogs with different numbers of galaxies N_{gal} . The number of simulated catalogs created in the run is symbolized by N_{try} , and all other simulation parameters are given in the text.

run	simulations			$(\Omega_M, \Omega_\Lambda)$	analyses		
	N_{try} N_{gal}	$(\Omega_M, \Omega_\Lambda)$ $(z_{\text{min}}, z_{\text{max}})$	$\log L^*$ α		method	$\log L^*$	α
0823	100	(0.3,0.0)	37.00	(0.3,0.0)	STY	37.01 ± 0.06	-0.51 ± 0.12
	300	(0.0,1.5)	-0.50		ASF	37.00 ± 0.06	-0.50 ± 0.13
					BFR	37.01 ± 0.06	-0.51 ± 0.13
0824	100	(0.3,0.0)	37.00	(0.3,0.0)	STY	37.00 ± 0.08	-0.74 ± 0.11
	300	(0.0,1.5)	-0.75		ASF	37.00 ± 0.07	-0.74 ± 0.13
					BFR	37.00 ± 0.07	-0.74 ± 0.12
0822	100	(0.3,0.0)	37.00	(0.3,0.0)	STY	37.00 ± 0.08	-0.98 ± 0.11
	300	(0.0,1.5)	-1.00		ASF	36.98 ± 0.08	-0.98 ± 0.10
					BFR	36.98 ± 0.08	-0.98 ± 0.10
0828	100	(0.3,0.0)	37.00	(0.3,0.0)	STY	36.98 ± 0.09	-1.22 ± 0.08
	300	(0.0,1.5)	-1.25		ASF	36.96 ± 0.08	-1.21 ± 0.08
					BFR	36.96 ± 0.08	-1.21 ± 0.07
0821	100	(0.3,0.0)	37.00	(0.3,0.0)	STY	36.98 ± 0.11	-1.46 ± 0.08
	300	(0.0,1.5)	-1.50		ASF	36.93 ± 0.10	-1.44 ± 0.07
					BFR	36.93 ± 0.11	-1.44 ± 0.07
0829	100	(0.3,0.0)	37.00	(0.3,0.0)	STY	36.90 ± 0.15	-1.65 ± 0.08
	300	(0.0,1.5)	-1.75		ASF	36.81 ± 0.11	-1.60 ± 0.06
					BFR	36.81 ± 0.11	-1.60 ± 0.06

Table 4.3: A comparison of luminosity function determination methods, as applied to sets of simulated galaxy redshift survey catalogs with different input faint end slopes α . Formatting as in Table 4.2.

run	N_{try} N_{gal}	simulations		$(\Omega_M, \Omega_\Lambda)$	method	analyses	
		$(\Omega_M, \Omega_\Lambda)$ $(z_{\text{min}}, z_{\text{max}})$	$\log L^*$ α			$\log L^*$	α
0831	100	(0.3,0.0)	36.40	(0.3,0.0)	STY	36.41 ± 0.09	-1.01 ± 0.12
	300	(0.0,0.6)	-1.00		ASF	36.39 ± 0.09	-0.98 ± 0.12
					BFR	36.40 ± 0.09	-1.00 ± 0.11
0907	100	(0.3,0.0)	36.40	(0.3,0.0)	STY	36.40 ± 0.16	-0.98 ± 0.56
	300	(0.6,1.5)	-1.00		ASF	36.38 ± 0.16	-0.99 ± 0.62
					BFR	36.39 ± 0.14	-0.98 ± 0.52
0910	100	(0.3,0.0)	36.40	(0.3,0.0)	STY	36.44 ± 0.41	-1.65 ± 1.00
	300	(0.6,1.5)	-1.75		ASF	36.40 ± 0.40	-1.46 ± 1.06
					BFR	36.40 ± 0.30	-1.57 ± 0.82
0912	100	(1.0,0.0)	36.40	(0.3,0.0)	STY	36.53 ± 0.16	-0.96 ± 0.52
	300	(0.6,1.5)	-1.00		ASF	36.56 ± 0.16	-1.10 ± 0.60
					BFR	36.55 ± 0.15	-1.03 ± 0.50
0912a	100	(0.3,0.7)	36.40	(0.3,0.0)	STY	36.30 ± 0.18	-0.99 ± 0.63
	300	(0.6,1.5)	-1.00		ASF	36.30 ± 0.19	-0.91 ± 0.72
					BFR	36.31 ± 0.17	-0.97 ± 0.61
0926	100	(1.0,0.0)	36.40	(0.3,0.0)	STY	36.48 ± 0.31	-1.57 ± 0.75
	300	(0.6,1.5)	-1.75		ASF	36.48 ± 0.28	-1.58 ± 0.78
					BFR	36.48 ± 0.28	-1.55 ± 0.68
0926a	100	(0.3,0.7)	36.40	(0.3,0.0)	STY	36.27 ± 0.28	-1.62 ± 0.76
	300	(0.6,1.5)	-1.75		ASF	36.28 ± 0.28	-1.64 ± 0.85
					BFR	36.30 ± 0.26	-1.66 ± 0.77

Table 4.4: A comparison of luminosity function determination methods, as applied to sets of simulated galaxy redshift survey catalogs in (upper) two different wide redshift bins ($0 < z < 0.6$ and $0.6 < z < 1.5$) and (lower) the high-redshift bin, but analyzed in the wrong world model. Formatting as in Table 4.2.

Aug 7 17:33:51 1997

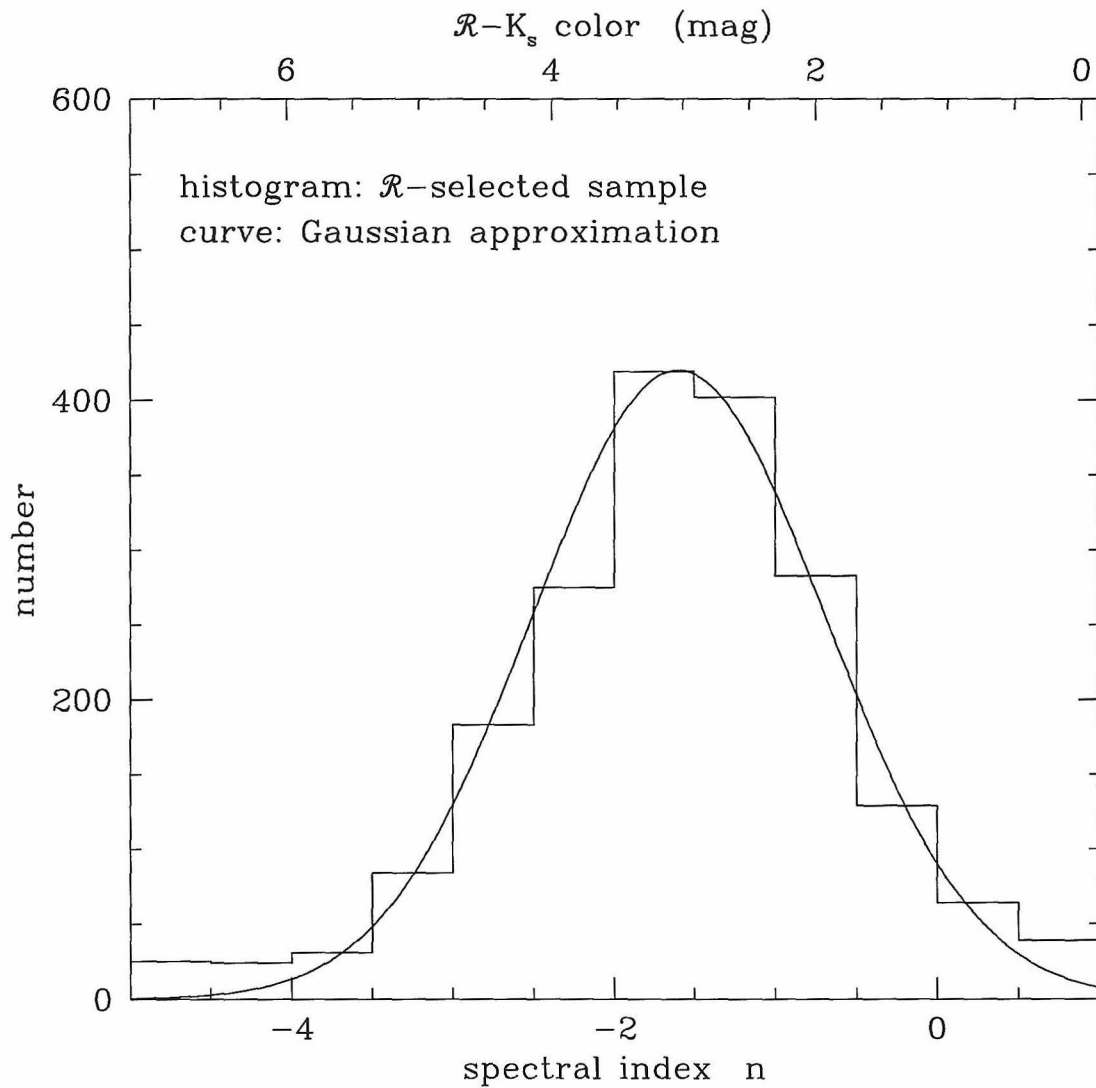
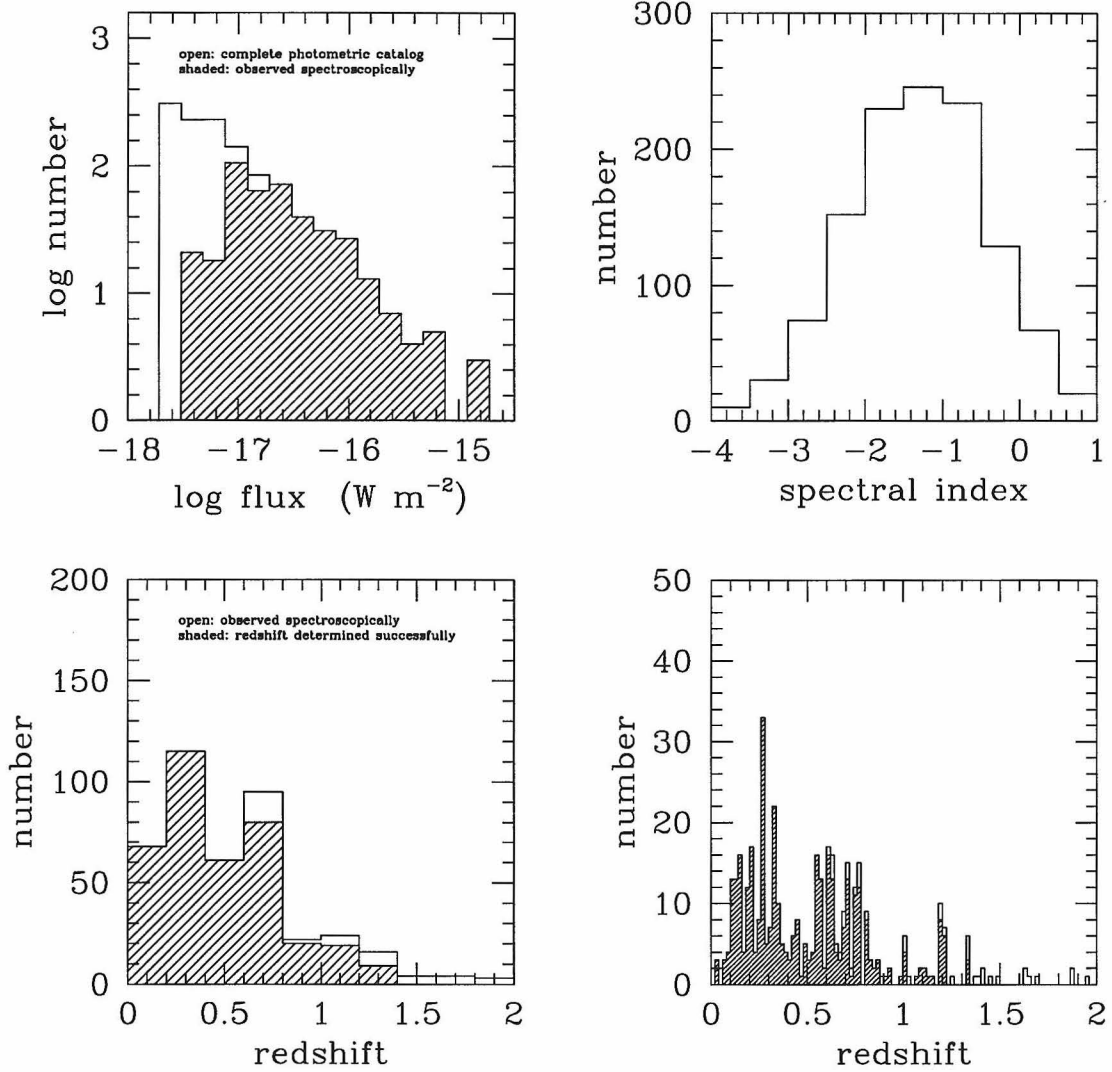
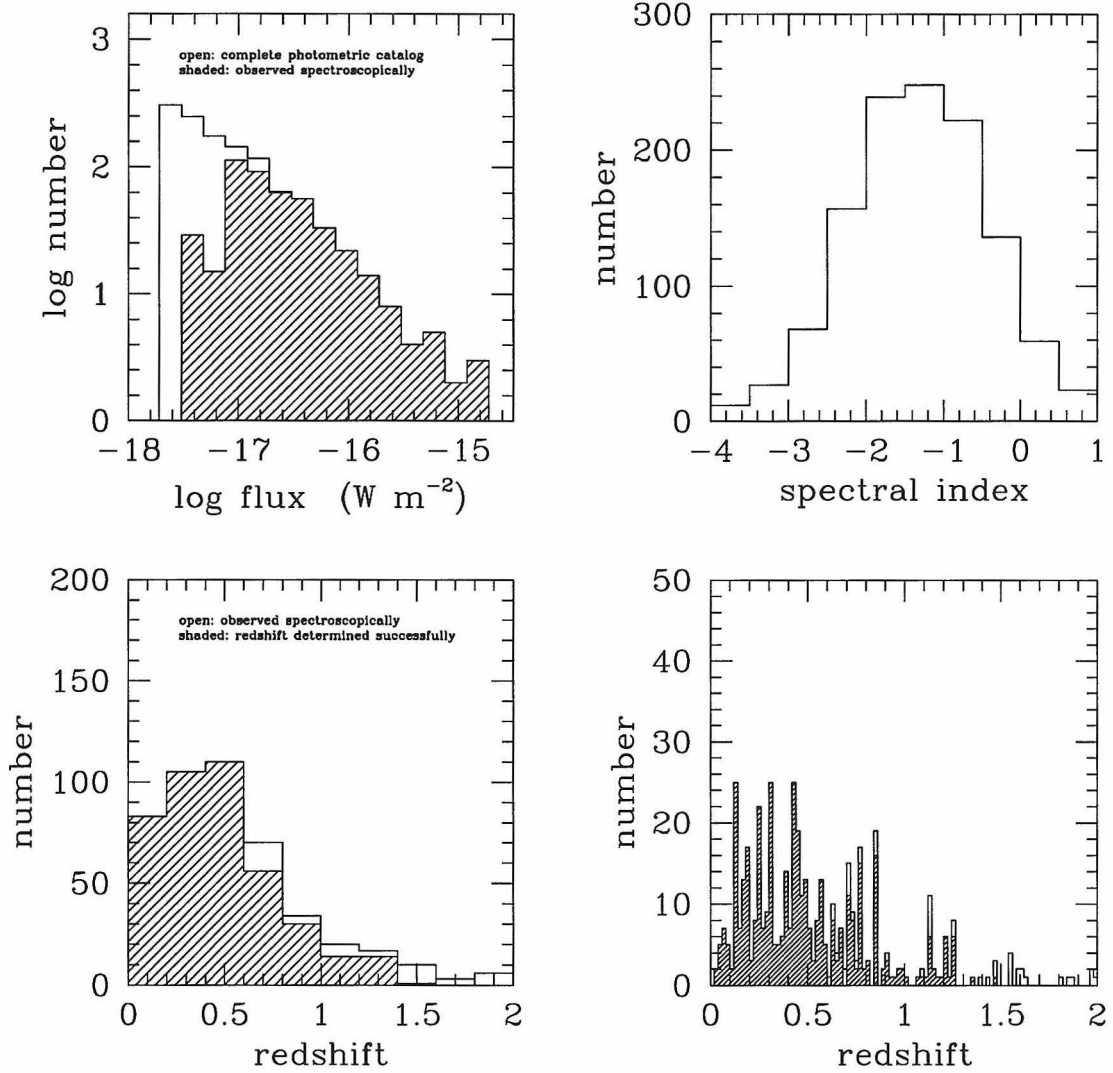


Figure 4.1: The spectral index n distribution function for the galaxies in the \mathcal{R} -selected sample in the HDF. The distribution is fit fairly well by a Gaussian with mean $n = -1.6$ and variance $\sigma_n^2 = 0.83$ except in the extreme high- and low-index tails, but these extreme sources are not a significant contribution to the sample, and some of them have erroneous colors because they are blended or confused sources at the faint end of the survey.



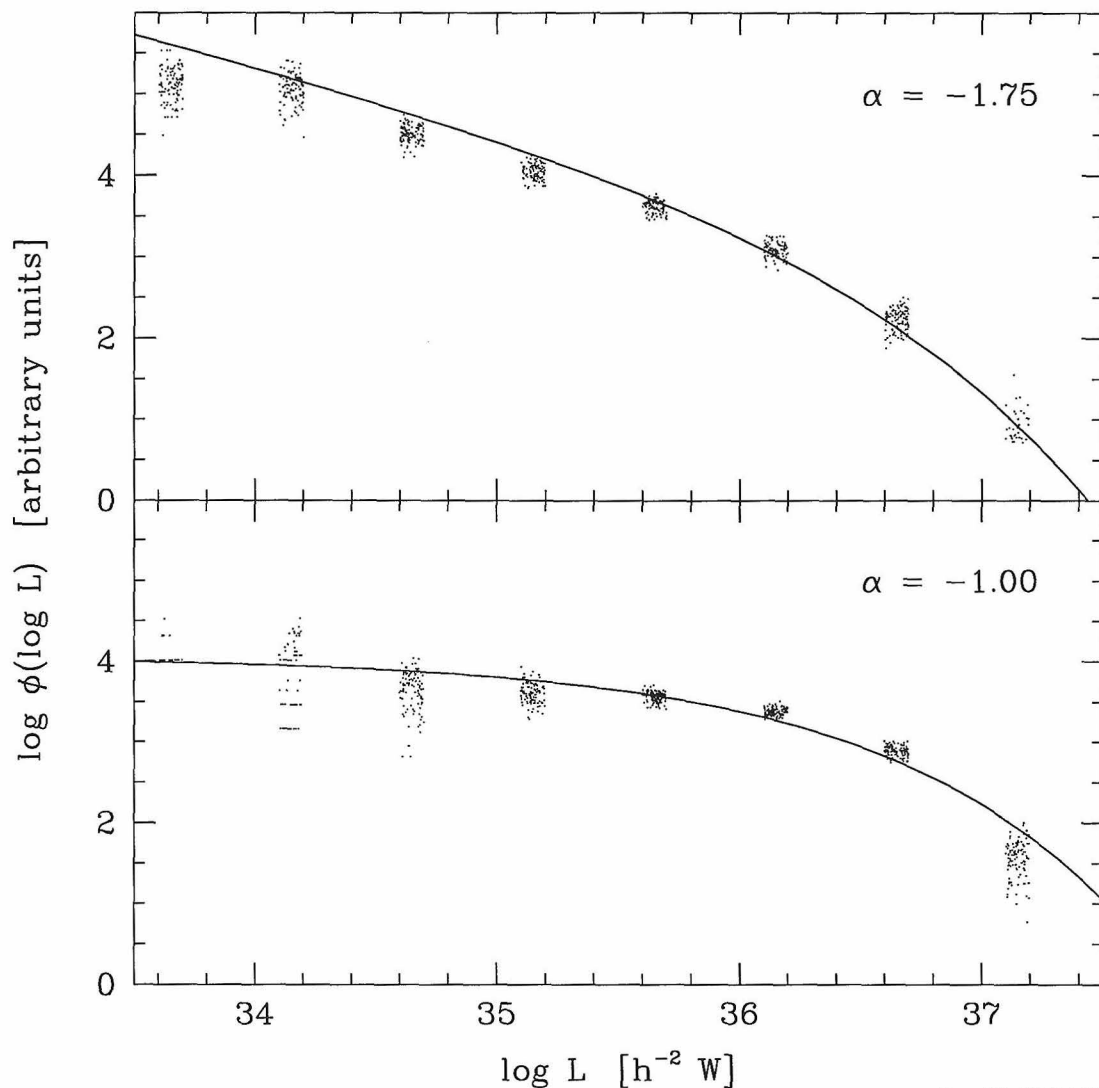
Aug 13 10:02:09 1997

Figure 4.2: Example single-field redshift-survey simulation, with 500 galaxies at $z < 2$, a luminosity function with $\alpha = -1.5$, and a redshift peak every 0.09 Hubble distances, constructed as described in the text. The number-flux relation is shown with all sources in the photometric catalog unshaded and those which were observed spectroscopically shaded. The completeness drops off sharply fainter than $\mathcal{R} = 23$ mag. The redshift histogram is shown at two different resolutions, with spectroscopically identified sources shaded and those tried but not successfully identified unshaded.



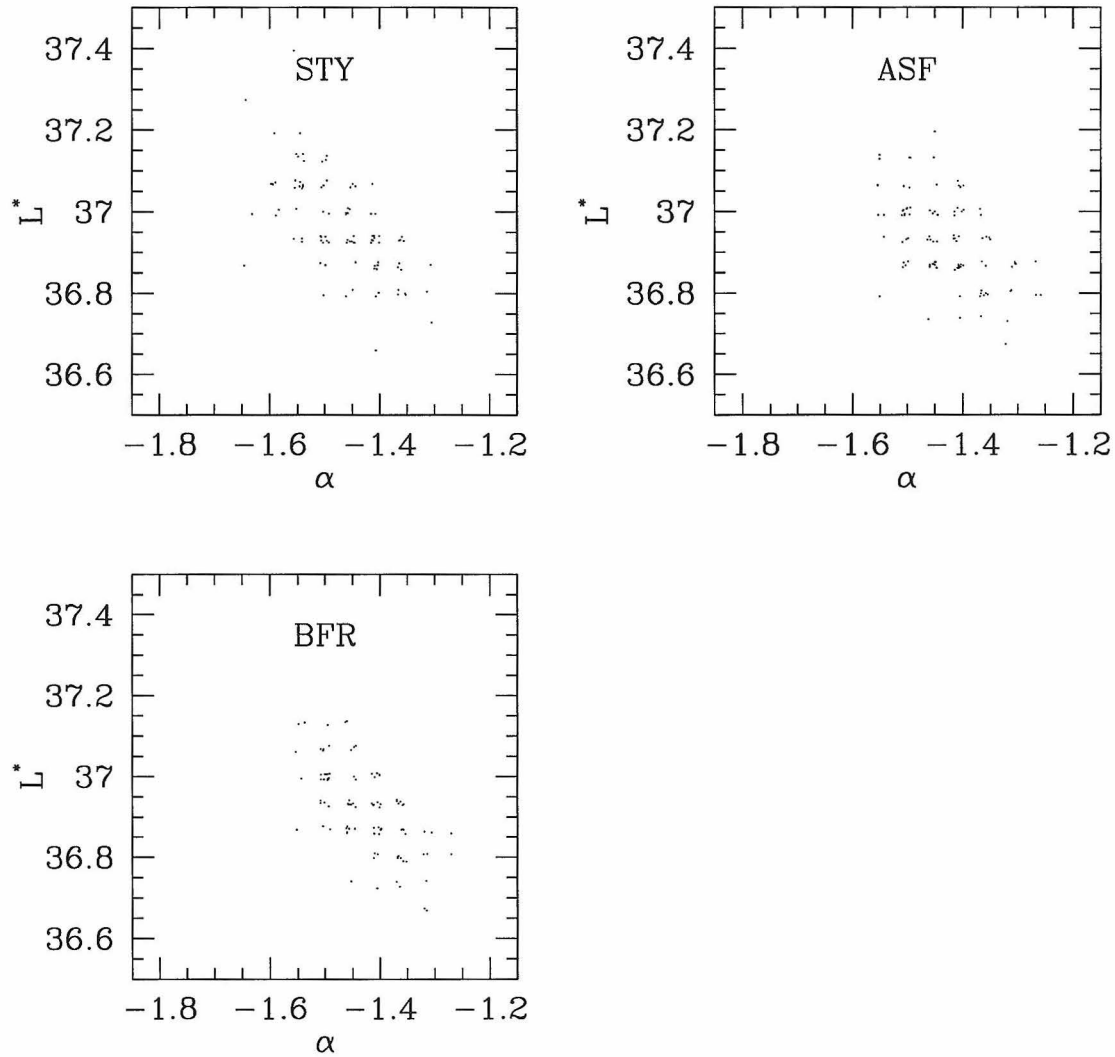
Aug 13 10:02:19 1997

Figure 4.3: Another example single-field redshift-survey simulation, same as Figure 4.2 but with a different random number sequence.



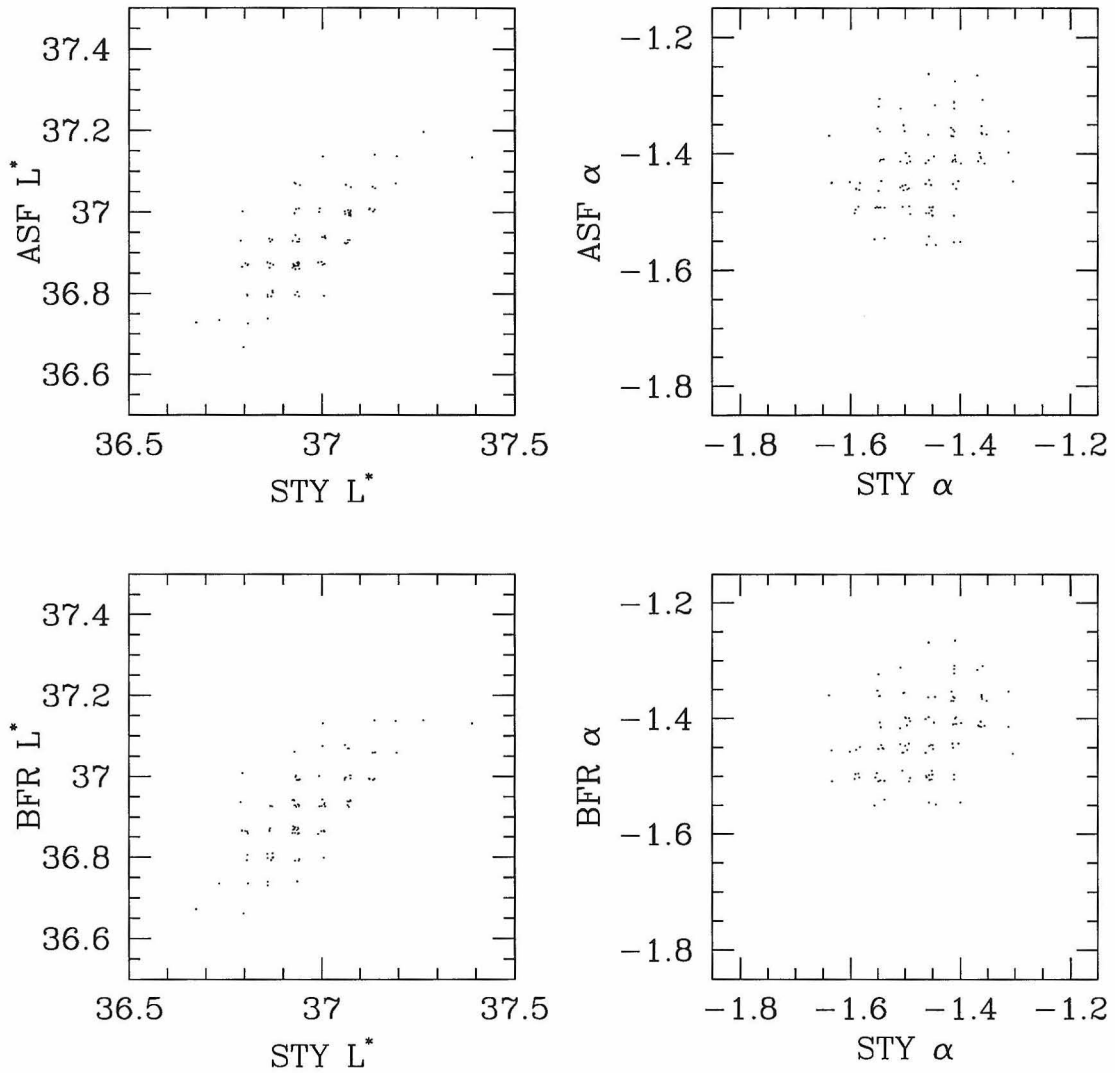
Sep 30 09:50:32 1997

Figure 4.4: Results of two tests of the generalized V-max method. In each case, the method is applied to 100 catalogs of 300 galaxies each, observed in the range $17 < \mathcal{R} < 23$ mag. The catalogs are made with $L^* = 36.4$ and $\alpha = -1.00$ and -1.75 and in a world model with $(\Omega_M, \Omega_\Lambda) = (0.3, 0.0)$. Both completeness functions described in Section 4.3 are used in both the simulations and analysis. The output luminosity functions are computed on a standard grid, but the points have been shifted horizontally by random offsets in order to make their true scatter visible. The true (input) luminosity functions are shown with solid lines. Several biases are noticeable; they are discussed in the text.



Aug 19 15:06:09 1997

Figure 4.5: Results of the STY, ASF and BFR methods, applied to 100 simulated catalogs of 300 galaxies each in the flux range corresponding to $17 < \mathcal{R} < 23$ mag, constructed as described in the text. For each catalog, the maximum-likelihood $\log L^*$ and α values are marked with a dot. Luminosity function models are tested on a grid; the points have been given small random offsets so they will not all appear exactly on top of one another.



Aug 19 15:06:21 1997

Figure 4.6: Relationships between the $\log L^*$ and α values inferred by the STY, ASF and BFR methods for the same simulated catalogs as those used in Figure 4.5. The inferred $\log L^*$ values are clearly correlated.

Chapter 5 The luminosity function of field galaxies and its evolution at redshifts $z < 1.5$

5.1 Introduction

As discussed in Chapter 1, there is a discrepancy between the number of very faint sources visible in deep images (*e.g.*, Williams et al 1996; Hogg *et al.* 1997b) and the local number density of luminous galaxies as measured by the local luminosity function. Locally the luminosity function $\phi(L)$ (number density per unit luminosity) is well fitted by a Schechter (1976) function

$$\phi(L) = \frac{\phi^*}{L^*} \left(\frac{L}{L^*} \right)^\alpha e^{-L/L^*} \quad (5.1)$$

with characteristic number density ϕ^* around $10^{8.5}$ per Hubble Volume ($10^{-1.9} h^3 \text{ Mpc}^{-3}$; see Appendix B), characteristic luminosity L^* around $\nu L_\nu \approx 10^{36.4}$ W, “flat” faint-end slope $\alpha \approx -1$, which corresponds to constant number density per log luminosity at the faint end. Table 4.1 in Chapter 4 summarizes the local measurements, which show a remarkable similarity in shape and characteristic luminosity, but a remarkable diversity in characteristic number density.

The discrepancy between the local luminosity function results and the faint source counts is twofold. First, for most of the local determinations, the total number density of galaxies is too small for the number of faint sources to be drawn from a similar population at all redshifts. Furthermore, a simple convolution of the local luminosity function with the comoving volume element in standard cosmological world models (Appendix B) leads to galaxy number counts which flatten out at the very

faint end to a relatively constant number per log flux interval, whereas the observed counts steadily increase at the faint end by roughly a factor of two per magnitude of survey depth (Williams *et al.* 1996; Hogg *et al.* 1997b). This latter discrepancy means that the “number problem” gets worse the longer one integrates on an empty field! The discrepancies have many possible resolutions: observational or technical “errors,” biases or misconceptions may plague our understanding of the local Universe; cosmological theory may be incorrect; or, most likely, the luminosity function of galaxies may have evolved significantly.

Several large surveys have been undertaken to measure the evolution in the galaxy luminosity function. Recently, two many-hundred-galaxy surveys have been completed, the CFRS (Lilly *et al.* 1995) and Autofib (Ellis *et al.* 1996). Both of these surveys find luminosity functions with normalizations (*i.e.*, total galaxy number density) higher than the bulk of local determinations (*e.g.*, the APM survey; Loveday *et al.* 1992) and both find at least tantalizing hints of a “steepening” of the luminosity function with redshift. That is, both find evidence that the luminosity function contained a higher fraction of low-luminosity galaxies in the past ($\alpha \approx -1.5$ or -1.75 rather than -1). At the same time, these surveys do not find evidence of strong evolution in the characteristic luminosity L^* at which the luminosity function cuts off, nor do they find evidence for a change in the number density of sources with luminosities around L^* (Lilly *et al.* 1995; Ellis *et al.* 1996). Such evolution in the shape of the function, rather than in the total number density or characteristic luminosity, was hinted at before these surveys, because it is a natural way to reconcile the galaxy counts, which rise steadily at faint magnitudes, with the redshift distributions, which seem to have a median redshift which is not a strong function of survey magnitude limit (Broadhurst *et al.* 1988). The evidence for this steepening of the luminosity function remains weak, however, and one of the purposes of this Chapter is to test whether the deeper, more complete Caltech survey can confirm or deny this result.

The Hubble Space Telescope (HST) images of the Hubble Deep Field (HDF) are the most sensitive visual images ever taken of the sky (Williams *et al.* 1996). They reveal huge numbers of faint diffuse (*i.e.*, non-pointlike) sources, presumably distant

galaxies, at extremely high angular resolution in four bandpasses from 0.3 to 0.8 μm . The HDF has become a standard field for deep, “blank-sky” work, inspiring large numbers of radio (Fomalont *et al.* 1997), millimeter (Wilner & Wright 1997), infrared (Serjeant *et al.* 1997), near-infrared (Hogg *et al.* 1997; Chapter 2; Dickinson *et al.* in preparation), and spectroscopic (Cohen *et al.* 1996b, and in preparation; Steidel *et al.* 1996; Lowenthal *et al.* 1997) follow-up observations, all aimed at identifying the important physical properties of the excess faint sources. As part of the Caltech faint field galaxy surveys, visual spectroscopy (Cohen *et al.* 1996b, and in preparation) and near-infrared K_s -band imaging (Hogg *et al.* 1997; Chapter 2) have been taken in the HDF. In this Chapter, the Caltech HDF data, along with the HST data and some data from the Hawaii (*e.g.*, Cowie *et al.* 1996) and the University of California DEEP collaboration (*e.g.*, Koo *et al.* 1996) groups, are used to measure the galaxy luminosity function and its dependence on redshift, color and environment.

In what follows, physical quantities are quoted in SI units, with Hubble constant $H_0 = 100 h \text{ km s}^{-1} \text{ Mpc}^{-1}$, in world model $(\Omega_M, \Omega_\Lambda) = (0.3, 0)$ (Appendix B). The only exception are number densities, which are given in $h^3 \text{ Mpc}^{-3}$. Fluxes and luminosities are given as flux and luminosity densities per logarithmic frequency interval, *i.e.*, νS_ν or λS_λ and νL_ν or λL_λ , in W m^{-2} and W . Luminosities are all-sphere (not per-steradian). Conversions to astronomical magnitudes are given below and in detail in Appendix A.

5.2 Sample

The sample is the Caltech Faint Field Galaxy Redshift Survey (Cohen *et al.* 1996a; Cohen *et al.* 1996b; Cohen *et al.* in preparation) in the HDF. The source selection and photometry for this sample are described in Chapter 2. Briefly, the sample is selected in a eight-arcmin-diameter circular region centered on the HDF in the \mathcal{R} band, down to $\mathcal{R} = 23.3$ mag everywhere and down to $\mathcal{R} = 24.8$ mag in the central, HST-imaged portion of the field ($\approx 5 \text{ arcmin}^2$). It contains 631 sources. The vast majority of the sources have U_n , G , \mathcal{R} and K_s photometry, and those in the HST image of the central

region have in addition $F300W$, $F450W$, $F606W$ and $F814W$ photometry.

Spectroscopy was performed with the LRIS instrument (Oke *et al.* 1995) on the 10-m Keck Telescopes during a series of runs in 1996 and 1997. Typically the spectra cover the wavelength range $4000 < \lambda < 8500 \text{ \AA}$ with 2.5 \AA per pixel, and a resolution of about 700. Spectra showing only a single emission line were assumed to be showing the [O II] 3727 \AA line and spectra showing only a single spectral break were assumed to be showing the 4000 \AA break. Details of the observing, reduction and redshift identification procedures are published elsewhere (Cohen *et al.* in preparation). The sample is not complete, neither in the sense of having spectroscopic data for all sources in the sample, nor in the sense of having obtained a redshift for every source for which spectroscopic data exist. Of the 631 sources in the sample, 483 are galaxies with measured redshifts, 37 are stars, leaving 111 unidentified. The completeness is described in detail in Section 5.4.

The analyses below use only those 422 sources with determined redshifts less than $z = 1.5$ and fluxes brighter than $\mathcal{R} = 24.5 \text{ mag}$.

5.3 Methods

Each galaxy in the survey is assigned three numbers (S, n, z) : The *flux* S is the flux νS_ν in SI units (W m^{-2}) as derived from the \mathcal{R} total magnitude measured as described in Chapter 2 and the zeropoint given in Appendix A:

$$\log S \equiv -7.92 - 0.4 \mathcal{R} \quad (5.2)$$

The *index* n is the slope of the power-law approximation to the galaxy's spectral energy distribution $\nu S_\nu \propto \nu^n$ in the vicinity of the rest (emitted) B band. This is estimated with the $G - \mathcal{R}$ color or the $\mathcal{R} - K_s$ color, depending on redshift z :

$$n \equiv \begin{cases} 1.97 - 2.54(G - \mathcal{R}) & \text{for } z < 0.57 \\ 0.89 - 0.82(\mathcal{R} - K_s) & \text{for } z > 0.57 \end{cases} \quad (5.3)$$

These equations are found with a simple power-law approximation to the spectral energy distribution given the apparent magnitudes:

$$n \equiv \frac{\mathcal{R} - K_s}{2.5 \log[\nu_{K_s}/\nu_{\mathcal{R}}]} + \frac{Z_{K_s} - Z_{\mathcal{R}}}{\log[\nu_{K_s}/\nu_{\mathcal{R}}]} \quad (5.4)$$

(and the corresponding equation for G and \mathcal{R}), where ν_{K_s} and $\nu_{\mathcal{R}}$ are the effective frequencies and Z_{K_s} and $Z_{\mathcal{R}}$ are the logarithmic absolute calibrations $\log[\nu f_{\nu}^{(0)}]$ for the K_s and \mathcal{R} bands, given in Appendix A. Finally, each object has a *redshift* z , defined to be the ratio of observed to emitted wavelengths (see Appendix B). Redshifts are determined by spectroscopy, described above and in Cohen *et al.* (in preparation).

The flux S and index n are both very crude measures of galaxy photometry. The first, flux S , is crude because in the HDF sample used here, fluxes are measured through isophotal apertures, at least at the brighter end (see Chapter 2 for details). Such fluxes depend on the quality of the imaging data, in that lower isophotal thresholds can be used with better data. Also, the true radius of the isophote around each galaxy depends strongly on redshift because surface brightness decreases with increasing redshift. This problem alone can lead to biases in luminosity function determination (Dalcanton, in preparation). The index n is a crude measure because of course galaxy spectra are not well described by power-laws. However, with the small number of galaxies used in this study, luminosity function features (such as L^*) cannot be determined to better than tens of percent in luminosity, at which accuracy these crude measures are acceptable.

Because the median redshift is around $z = 0.6$ and the sample is selected in the \mathcal{R} band at 6900 \AA , the natural rest-frame bandpass for measuring the luminosity function is the B band at 4400 \AA . Conveniently this is also the traditional bandpass for luminosity function measurement in the astronomical literature. The B -band luminosity $L \equiv \nu L_{\nu}$ is estimated with

$$\log L = \log S + \log[4 \pi] + 2 \log D_L(z) - n \log \left[(1+z) \frac{\nu_{\mathcal{R}}}{\nu_B} \right] \quad (5.5)$$

where $D_L(z)$ is the luminosity distance (Appendix B) and $\nu_{\mathcal{R}}$ and ν_B are the effective frequencies of the \mathcal{R} and B bands. In this case $\nu_B/\nu_{\mathcal{R}} \approx 1.57$, or $z = 0.57$ is the redshift at which the observed \mathcal{R} band is the rest-frame B . Note that this luminosity is all-sphere, not per-steradian.

The four methods used to estimate the luminosity function are V-max, STY, ASF and BFR, all described in Chapter 4. Briefly, the V-max method is based on Schmidt’s (1968) V/V-max method for demonstrating evolution among members of a flux-limited sample of quasars. For each galaxy there is a volume V_{\max} of the Universe in which it could lie and still remain inside the sample; this volume is computed and its inverse represents that galaxy’s contribution to the number density. The method used here includes the trivial modification of explicit redshift limits z_{\min} and z_{\max} which can be varied to measure (rather than simply constrain) the evolution in the sample (similar to the method of Eales 1993). The remaining methods are maximum-likelihood methods. The STY method estimates, for each object, the likelihood that it has its measured flux, given its redshift and each of a set of luminosity function models. The individual likelihoods for all the galaxies are multiplied together to get a total likelihood for each luminosity function model. The ASF method is similar to STY except that each individual likelihood is that of it having its measured redshift given its flux. The BFR method is similar except it treats redshift and flux on an equal footing. The different methods have different drawbacks, discussed in Chapter 4 and touched-upon below; they are used in different circumstances accordingly. The BFR method is underutilized here because it is extremely computationally expensive.

5.4 Completeness functions

As described in Chapter 4, the methods depend on two completeness functions, the *a priori* completeness $\eta_{\text{try}}(S, n)$ and the *a posteriori* completeness $\eta_{\text{got}}(S, n, z)$ (except ASF which only depends on the latter). The *a priori* is easy to measure from the sample by comparing the number-flux relation of spectroscopically observed sources to the total number-flux relation. This comparison is shown in Figure 5.1, and the

derived *a priori* completeness function $\eta_{\text{try}}(S, n)$ is shown in Figure 5.2. The completeness function is not computed by comparing the observed sources to the total number in the sample, because the field area of the sample depends on magnitude, with the field size dropping rapidly at $\mathcal{R} > 23$ mag where the sample is only inside the smaller, central, HST-imaged portion of the field. To compute the completeness function, the number-flux relation at $\mathcal{R} > 23$ mag is computed by extrapolating with $d \log N/d\mathcal{R} = 0.3 \text{ mag}^{-1}$, which is appropriate in this band (Hogg *et al.* 1997). See Figure 5.1 for more information. After using this extrapolation, the *a priori* completeness function drops off rapidly at the large-field magnitude limit of $\mathcal{R} = 23$ mag and then has a small contribution at $\mathcal{R} > 23$ mag where the field is smaller. Because the sample was selected in the \mathcal{R} image, this procedure for computing the *a priori* completeness function is acceptable. It would not be acceptable to perform the analysis with a completeness function determined in the same way but, say, in the U_n image, because there would then be a color bias to the selected sources.

The *a posteriori* completeness function $\eta_{\text{got}}(S, n, z)$ is harder to estimate because it represents the probability that a galaxy redshift is successfully identified, which depends on the spectral properties of exactly those galaxies for which there are no measured spectral features. However, the majority of galaxies at redshifts $z > 0.6$ are identified on the basis of the [O II] 3727 Å emission line, which is studied for this sample in Chapter 3. Galaxies at redshifts $z < 0.6$ are often identified on the basis of several emission features, or sometimes simply a 4000 Å break. Redshift $z = 0.6$ is the dividing line because at this redshift and below, the [O III] 5007 Å emission line enters the spectroscopic window, along with other features such as the G band, [O III] 4959 Å, and H β . Furthermore, pure 4000 Å break spectra are very rare at redshifts $z > 0.5$. For these reasons, the assumption is made that the probability $\eta_{\text{got}}(S, n, z)$ of successfully identifying a redshift for any spectroscopically observed galaxy in the sample is unity if $z < 0.6$ and the probability $p(S, n, z)$ of detecting [O II] 3727 Å if $z > 0.6$. This probability function is computed in Chapter 3 under a number of assumptions of regularity and simplicity in the distribution of [O II] 3727 Å equivalent widths with magnitude, color and redshift. The function $p(S, n, z)$ is shown

graphically in Figure 3.8.

Unfortunately, the luminosity function results will depend on this choice for the *a posteriori* completeness function $\eta_{\text{got}}(S, n, z)$, despite the fact that the function is not directly measurable. On the other hand, there is a simple *ex post facto* check that the function is a reasonable approximation. The inferred luminosity function can be used to predict, as a function of magnitude, the fraction of spectroscopically observed galaxies which ought not have successful redshift identifications. If this is not consistent with the observed fraction, the *a posteriori* completeness function can be adjusted. Unfortunately, this test only tells that it should be adjusted, not in detail how to adjust it.

5.5 Luminosity function results

In this Section, luminosity functions are computed for the \mathcal{R} -selected galaxy sample in the HDF, and subsamples thereof. This involves cutting the sample in various ways, measuring the luminosity functions, and looking for discrepancies and differences. This work is somewhat dangerous, because, for instance, if one cuts a sample in half twenty different ways, one expects, purely by chance, to find on the order of one two-sigma difference (*i.e.*, an effect at 95 percent confidence) between some pair of halves. For this reason, the significance of any result can only be assessed if all trials are listed. In this Section, all trials are plotted in the Figures; there are no discarded trials, or adjusted subsample sample cutoffs to maximize result significance.

5.5.1 Whole sample results

The basic V-max results are shown in Figure 5.3, for the whole sample, and for the sample split at roughly the median index, $n = -1.5$. The result is compared to the local luminosity function from the Stromlo-APM survey (Loveday *et al.* 1992) and is in remarkably good agreement. As with the local measurement, the luminosity function derived here is “flat” at the faint end ($\alpha \approx -1$); *i.e.*, there are a constant number density per unit log luminosity fainter than the characteristic luminosity L^* . The

characteristic luminosity L^* setting the point of the exponential cutoff at the bright end is also close to the local value found by the APM group, although it does appear to be significantly brighter. Finally, the results are in remarkable agreement with the Stromlo-APM results in amplitude or number density. This V-max calculation implicitly assumes that there is no evolution with redshift, a reasonable assumption as will be demonstrated below. Figure 5.3 also shows luminosity functions for the red and blue halves, which are discussed below.

Figure 5.4 shows the maximum-likelihood results for the entire sample, again compared with the Stromlo-APM result. Indeed, the faint-end slope α is consistent while the characteristic luminosity L^* appears to disagree at at least the two-sigma level. Again, these calculations implicitly assume no evolution.

5.5.2 Division by redshift

Redshift $z = 0.6$ was chosen as the dividing point for making low and high-redshift subsamples because it is close to the median redshift. V-max results for these two subsamples are shown in Figure 5.5 and maximum-likelihood results are shown in Figure 5.6. At the two-sigma level there is no significant difference between the low and high-redshift luminosity functions, in shape or amplitude. The results are consistent with a steepening of the faint end with increasing redshift but they certainly do not require it.

This conclusion is not sensitive to the world model in which the analysis is done. Figure 5.7 shows that there is no significant difference between the luminosity function shapes in the low and high-redshift subsamples in any reasonable world model. The STY method was used here because it is insensitive to redshift-space structure, which is emphasized in the redshift-divided subsamples because each contains fewer redshift peaks than the whole sample.

5.5.3 Division by color

Index $n = -1.5$ was chosen as the dividing point for making red and blue subsamples because it is close to the median index. Figure 5.3 shows the V-max results and Figure 5.8 shows the maximum-likelihood results for these samples. The ASF method was used here because it does not depend on the *a priori* selection function. It is difficult to precisely describe the *a priori* selection function for the color-selected samples because the sources do not have perfect power-law spectral energy distributions and therefore the measured color and therefore assigned index is not an invariant with redshift. Of course this problem is not tremendously severe given the crudeness of the results, and it does affect the V-max calculation anyway. Both the V-max and ASF methods show a highly significant difference between the luminosity functions of the red and blue subsamples. This difference is known locally: bluer galaxies lie in a steeper luminosity function, redder galaxies in a luminosity function which actually decreases at the faint end; it is only the sum of the two luminosity functions which is flat (Sandage *et al.* 1985; Marzke *et al.* 1994b; Marzke & da Costa 1997).

Figure 5.8 also shows the red and blue subsamples each split at redshift $z = 0.6$. Again, no significant evolution is found between these “quartiles,” although the results are consistent with a steepening of the faint end of both the red and blue populations.

5.5.4 Division by environment

The striking feature of the redshift distribution in the HDF and other deep fields surveyed is that of order half of the galaxies lie in narrow features or “peaks” in redshift space (Cohen *et al.* 1996a, 1996b). The natural interpretation is that these peaks represent groups of physically associated galaxies. In-peak and out-of-peak subsamples were constructed by taking, for the in-peak, all galaxies for which there are at least two others within a line-of-sight velocity difference of $\Delta v \leq 1000 \text{ km s}^{-1}$. The out-of-peak subsample is composed of all other galaxies. There are 174 and 248 galaxies in the in and out subsamples respectively. Figure 5.9 shows the maximum-likelihood luminosity function results for these two samples. The STY method was

used here because of course this subsample construction emphasizes redshift structure, to which STY is insensitive. At the two-sigma level the out-of-peak galaxies lie in a steeper luminosity function but the effect is not tremendously significant. No evolution with redshift is detected, as Figure 5.9 also shows.

5.6 Discussion

The luminosity function presented in Figure 5.3 is similar to the Stromlo–APM survey function (Loveday *et al.* 1992) in shape and characteristic luminosity but has a normalization which is higher by a factor of about two. This is similar to the recent results from other large, deep surveys, such as CFRS (Lilly *et al.* 1995) and Autofib (Ellis *et al.* 1996) which also find normalizations higher than most local determinations, except the CfA survey determination (Marzke *et al.* 1994a) which finds an unusually high normalization (Table 4.1 in Chapter 4). This normalization discrepancy is related to the number count problem discussed in Chapter 1 and Section 5.1 and it remains unresolved. It is possible that the effect is from a rapid evolution in the galaxy number density since $z \approx 0.2$. There is a growing consensus that some of the discrepancy is due to a failure of large, local surveys to detect low surface-brightness galaxies (*e.g.*, McGaugh 1994) and there is suspicion about the completeness and photometry of samples selected from photographic plate material, which most of the local samples are. The characteristic luminosity L^* determined from this survey is slightly brighter than the Stromlo–APM value, although only at two-sigma. This may indicate some fading of galaxies with time (*i.e.*, they were brighter in the past) or else it may be a technical issue of photometry. After all, we are measuring galaxies at high redshifts (so they appear small in angular size) with digital detectors while the Stromlo–APM survey measures nearby galaxies on photographic plates. The systematics in photographic photometry alone could account for the differences.

The variation of the luminosity function with color is completely consistent with local determinations (Marzke *et al.* 1994b; Marzke & da Costa 1997). It is also consistent with the Autofib survey results for the luminosity function as a function

of spectral type and redshift (Heyl *et al.* 1997).

No evidence is found here for evolution in the luminosity function with redshift. Several groups have attempted measurements of evolution in the galaxy luminosity function with deep surveys similar to this survey. Few have had as many sources or as much depth, and none has had both. The CFRS survey finds a steepening in the galaxy luminosity function with increasing redshift, but only in the blue half, when the sample is split red-blue (Lilly *et al.* 1995). The results presented here are consistent with this picture, although do not require it. It is surprising that the CFRS survey finds a significant change where this survey does not, given that the numbers of sources are similar, and that this survey goes to a fainter flux level and higher median redshift. However, the CFRS survey has several fields and therefore is less sensitive to field-to-field variations in the luminosity function. It is also possible that the CFRS survey assesses significance differently. Several other groups have found evidence for a steepening of the luminosity function with redshift (Broadhurst *et al.* 1988; Eales 1993; Ellis *et al.* 1996) so it seems most likely that the lack of evidence in this survey is simply a consequence of having only a small number of galaxies in a single field. The HDS survey finds an increase in the normalization of the luminosity function with increasing redshift (Cowie *et al.* 1996) which is at least marginally inconsistent with the results presented here (and the other results cited above), probably because the HDS did not have a large number of sources at high redshifts.

There is also no difference between the luminosity function in the redshift peaks and out; both show a fairly flat faint end. This is consistent with results in the local Universe for compact groups (Zepf *et al.* 1997). Combined with the knowledge that the local field galaxy luminosity function is flat, it is also consistent with the view that the peaks are generic locations for galaxy formation (Cohen *et al.* 1996b).

References

Broadhurst T. J., Ellis R. S. & Shanks T., 1988, The Durham Anglo-Australian Telescope faint galaxy redshift survey, MNRAS 235 827

- Cohen J. G., Hogg D. W., Pahre M. A. & Blandford R., 1996a, Strong redshift clustering of distant galaxies, *ApJ* 462 L9
- Cohen J. G., Cowie L. L., Hogg D. W., Songaila A., Blandford R., Hu E. M. & Shopbell P., 1996b, Redshift clustering in the Hubble Deep Field, *ApJ* 471 L5
- Cowie L. L., Songaila A., Hu E. M. & Cohen J. G., 1996, New insight on galaxy formation and evolution from Keck spectroscopy of the Hawaii Deep Fields, *AJ* 112 839
- Eales S., 1993, Direct construction of the galaxy luminosity function as a function of redshift, *ApJ* 404 51
- Ellis R. S., Colless M., Broadhurst T., Heyl J. & Glazebrook K., 1996, Autofib Redshift Survey I: Evolution of the galaxy luminosity function, *MNRAS* 280 235
- Fomalont E. B., Kellermann K. I., Richards E. A., Windhorst R. A. & Partridge R. B., 1997, Radio emission from objects in the Hubble Deep Field, *ApJ* 475 L5
- Heyl J., Colless M., Ellis R. S. & Broadhurst T., 1997, Autofib Redshift Survey II: The evolution of the galaxy luminosity function by spectral type, *MNRAS* 285 613
- Hogg D. W., Neugebauer G., Armus L., Matthews K., Pahre M. A., Soifer B. T. & Weinberger A. J., 1997a, Near infrared imaging of the Hubble Deep Field with the Keck Telescope, *AJ* 113 474
- Hogg D. W., Pahre M. A., McCarthy J. K., Cohen J. G., Blandford R., Smail I. & Soifer B. T., 1997b, Counts and colors of faint galaxies in the U and R bands, *MNRAS* 288 404
- Koo D. C. *et al.*, 1996, Redshift $z \sim 1$ field galaxies observed with the Keck Telescope and the Hubble Space Telescope, *ApJ* 469 535
- Lilly S. J., Tresse L., Hammer F., Crampton D. & Le Fevre O., 1995, The Canada-France redshift survey VI: Evolution of the galaxy luminosity function to $z \sim 1$, *ApJ* 455 108
- Lin H., Yee H. K. C., Carlberg R. G. & Ellingson E. E., 1997, The luminosity function of field galaxies in the CNOC1 redshift survey, *ApJ* 475 494
- Loveday J., Peterson B. A., Efstathiou G. & Maddox S. J., 1992, The Stromlo-APM redshift survey I: The luminosity function and space density of galaxies, *ApJ* 390 338
- Lowenthal J. D., Koo D. C., Guzman R., Gallego J., Phillips A. C., Faber S. M., Vogt N. P., Illingworth G. D. & Gronwall C., 1997, Keck spectroscopy of redshift $z \approx 3$ galaxies in the Hubble Deep Field, *ApJ* 481 673
- Marzke R. O., Huchra J. P. & Geller M. J., 1994a, The luminosity function of the CfA redshift survey, *ApJ* 428 43
- Marzke R. O., Geller M. J., Huchra J. P. & Corwin H. G., 1994b, The luminosity function for different morphological types in the CfA redshift survey, *AJ* 108 437
- Marzke R. O. & da Costa L. N., 1997, The galaxy luminosity function at $z \leq 0.05$: Dependence on color, *AJ* 113 185
- McGaugh S. S., 1994, A possible local counterpart to the excess population of faint blue galaxies, *Nature* 367 538
- Sandage A., Binggeli B. & Tammann G. A., 1985, Studies of the Virgo Cluster V: Luminosity functions of Virgo Cluster galaxies, *AJ* 90 1759

- Schechter P., 1976, An analytic expression for the luminosity function for galaxies, ApJ 203 297
- Schmidt M., 1968, Space distribution and luminosity function of quasi-stellar radio sources, ApJ 151 393
- Steidel C. C., Giavalisco M., Dickinson M. & Adelberger K. L., 1996, Spectroscopy of Lyman break galaxies in the Hubble Deep Field, AJ 112 352
- Williams R. E. *et al.*, 1996, The Hubble Deep Field: Observations, data reduction and galaxy photometry, AJ 112 1335
- Wilner D. J. & Wright M. C. H., 1997, A 2.8 millimeter survey of the Hubble Deep Field, ApJ 488 L67
- Zepf S. E., de Carvalho R. R. & Ribeiro A. L. B., 1997, The faint end of the luminosity function of galaxies in Hickson groups, ApJ 488 L11

Sep 25 07:56:11 1997

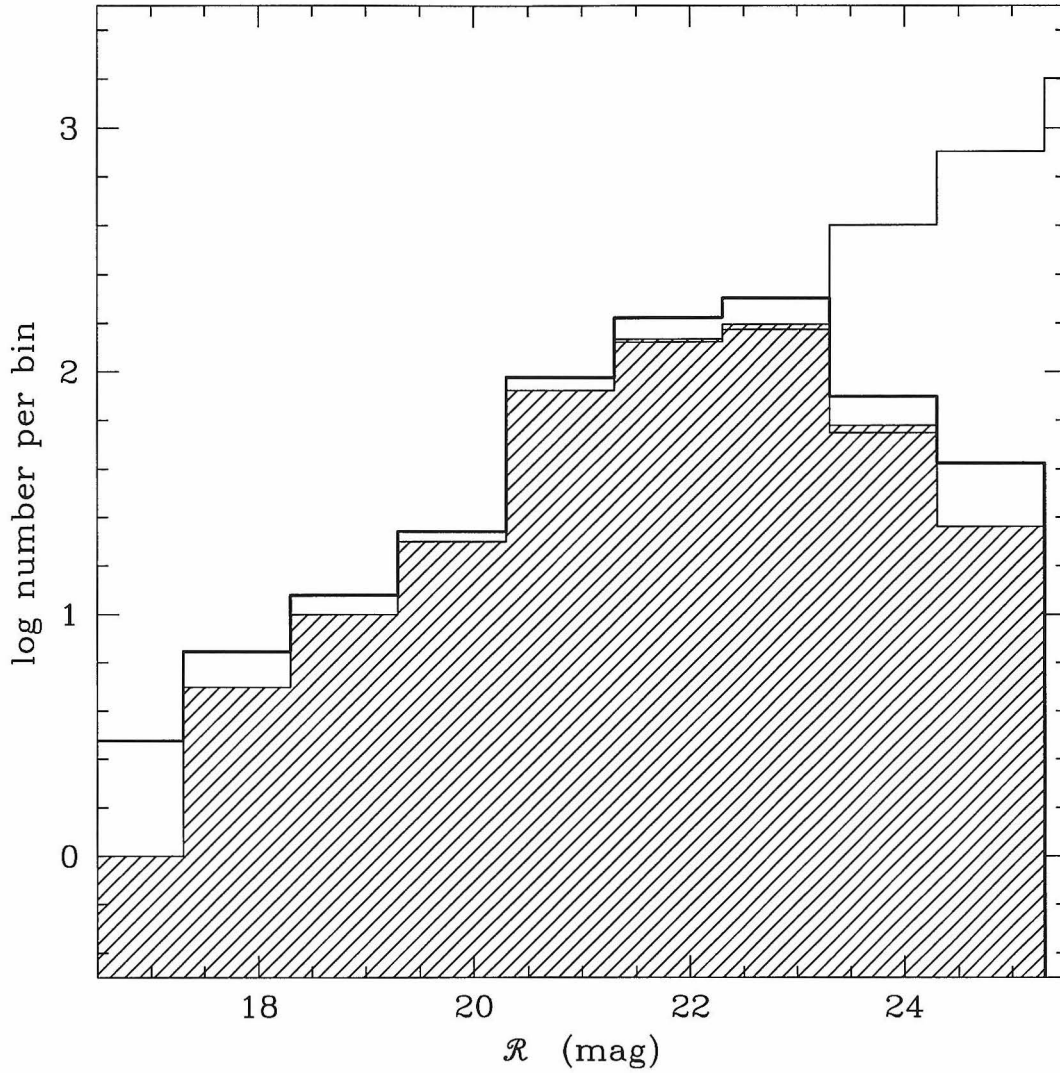


Figure 5.1: The comparison of the total number counts in the \mathcal{R} -selected sample in the HDF (heavy line) with the total number observed (shaded histogram) and those which have successful redshift identifications (line inside shaded histogram). The upper thin line shows an extrapolation of the $22.3 < \mathcal{R} < 23.3$ mag point according to $d \log N/d\mathcal{R} = 0.3 \text{ mag}^{-1}$, the expected number-flux relation if the field size did not depend on magnitude. The sample size drops rapidly at $\mathcal{R} > 23.3$ mag because the considered field area reduces from the 8-arcmin diameter circle to merely the HST image field of view.

Sep 25 07:56:26 1997

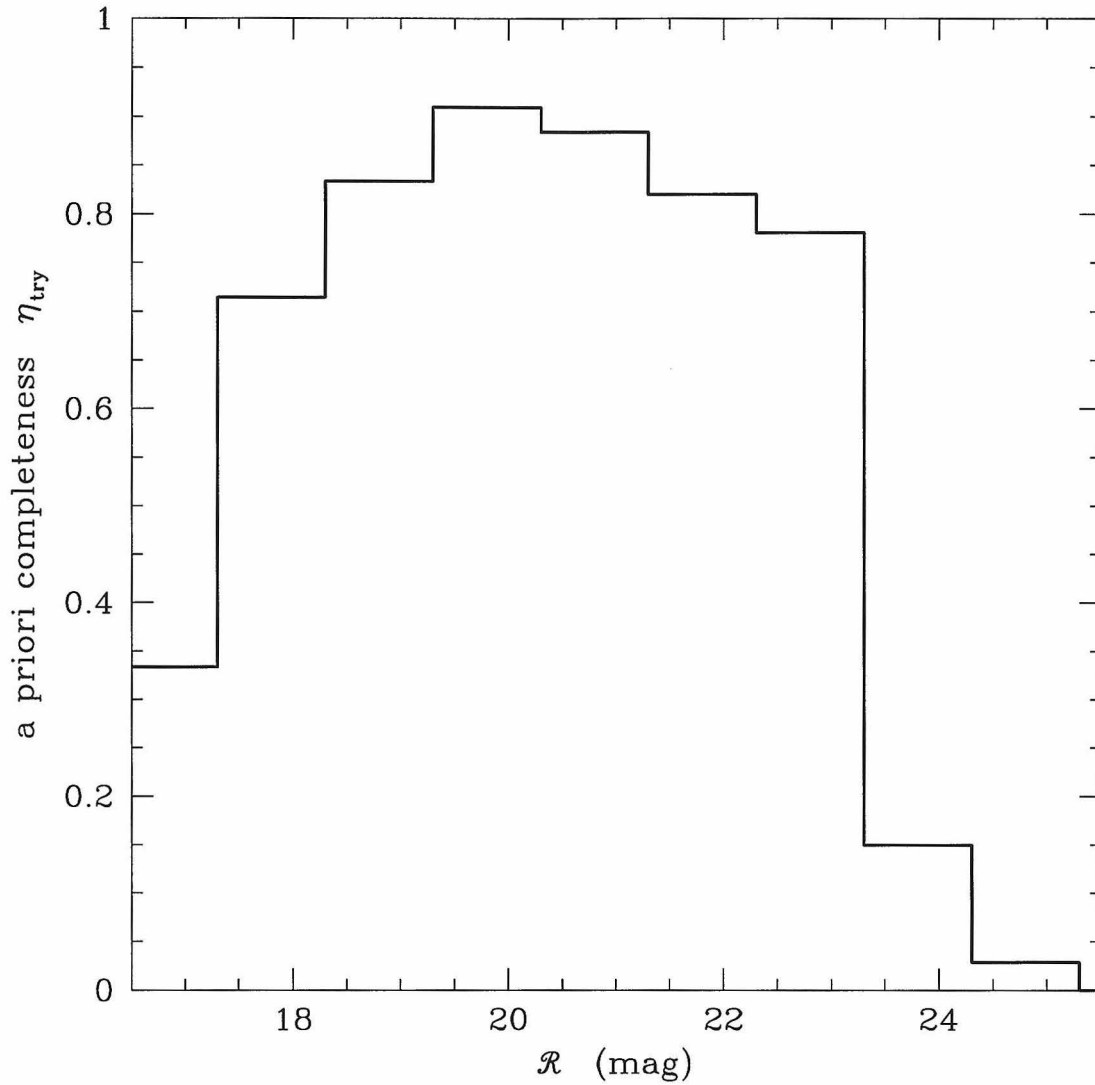
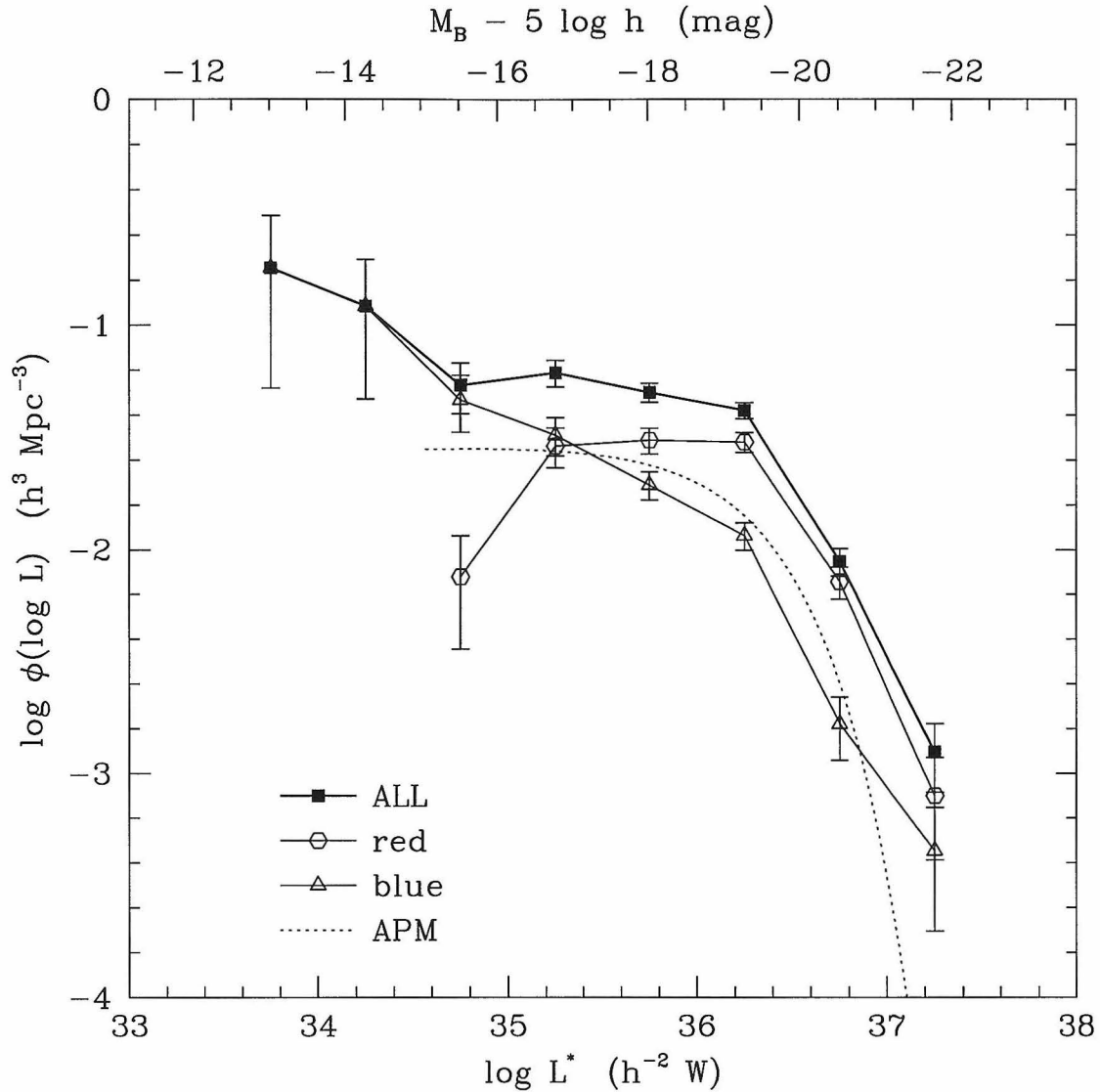
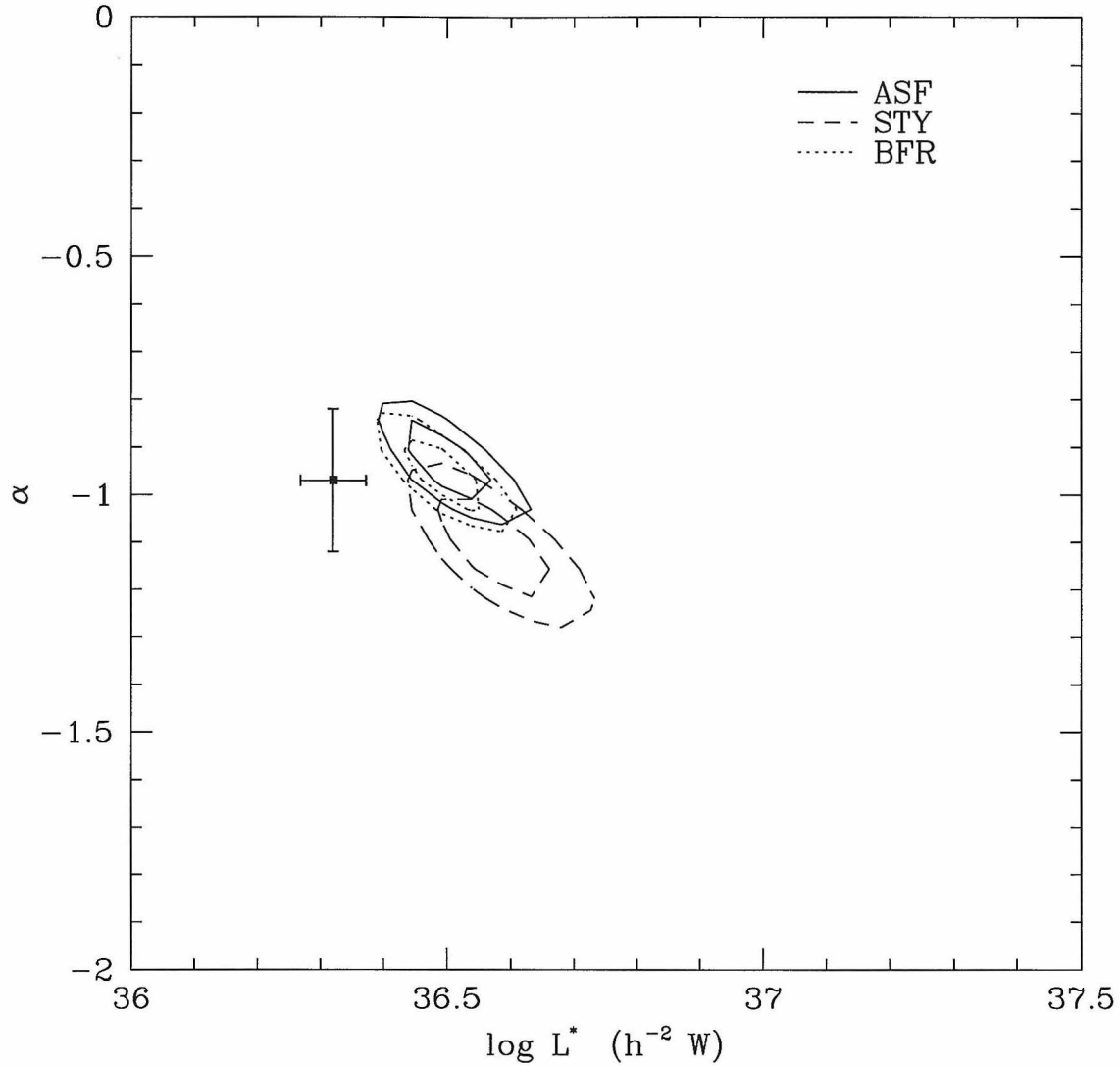


Figure 5.2: The *a priori* completeness function, computed by comparing the number-flux relation of sources observed spectroscopically with the total number-flux relation, which is just the number-flux relation for the sample at $\mathcal{R} < 23$ mag and an extrapolation at $\mathcal{R} > 23$ mag. See Figure 5.1 for more information. The low completeness at $\mathcal{R} < 19$ mag results from skipping some very bright sources, and the low completeness at $\mathcal{R} > 23.3$ mag results from the fact that the sample field area drops by more than 80 percent; see text for more information.



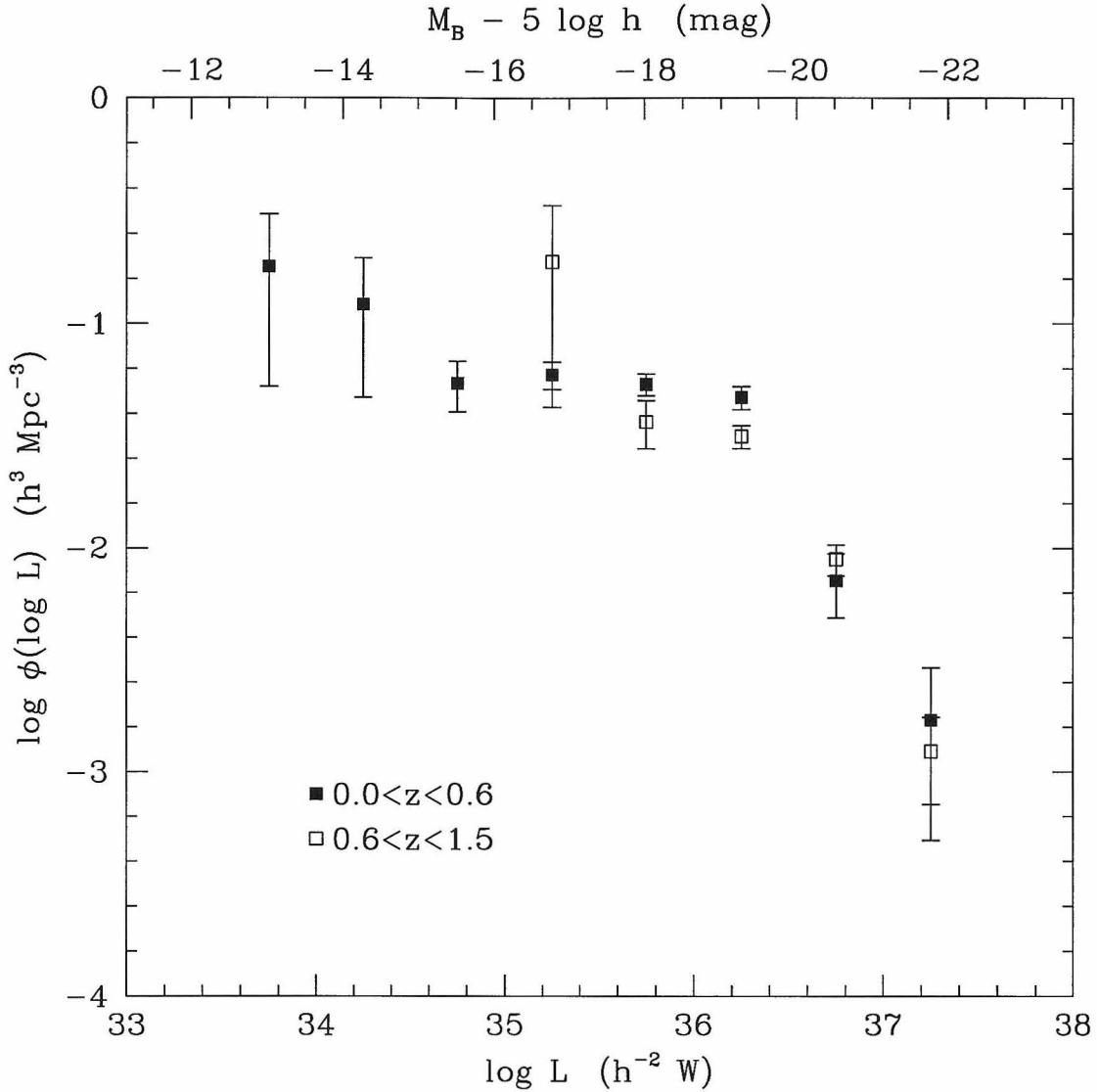
Sep 30 09:50:59 1997

Figure 5.3: Basic V-max results for the B -band galaxy luminosity function in the \mathcal{R} -selected HDF sample. The filled squares and heavy line are for the entire sample, while the open symbols and light lines are for red and blue halves, divided at spectral energy distribution $\nu S_\nu \propto \nu^{-1.5}$ in the spectral vicinity of the B band. The Hubble constant is taken to be $100 h \text{ km s}^{-1} \text{ Mpc}^{-1}$ in world model $(\Omega_M, \Omega_\Lambda) = (0.3, 0.0)$. The method and error bar estimation are described in the text. The dotted line shows the local luminosity function as determined by the Stromlo-APM group (Loveday *et al.* 1992), over the luminosity range in which it was determined.



Sep 30 09:51:18 1997

Figure 5.4: Basic maximum-likelihood results for the B -band galaxy luminosity function in the \mathcal{R} -selected HDF sample. The three sets of contours are for the three maximum-likelihood methods, ASF, STY and BFR, described in the text. The contours outline one and two-sigma confidence regions. The Hubble constant is taken to be $100 h \text{ km s}^{-1} \text{ Mpc}^{-1}$ in world model $(\Omega_M, \Omega_\Lambda) = (0.3, 0.0)$. The square dot shows the local luminosity function as determined by the Stromlo-APM group (Loveday *et al.* 1992), and the error bars show the published uncertainties in that result.



Sep 30 09:51:42 1997

Figure 5.5: V-max results for the B -band galaxy luminosity function in the \mathcal{R} -selected HDF sample, split by redshift at $z = 0.6$. The filled squares are for the low redshift sample, open for high. The Hubble constant is taken to be $100 h \text{ km s}^{-1} \text{ Mpc}^{-1}$ in world model $(\Omega_M, \Omega_\Lambda) = (0.3, 0.0)$. The method and error bar estimation are described in the text.

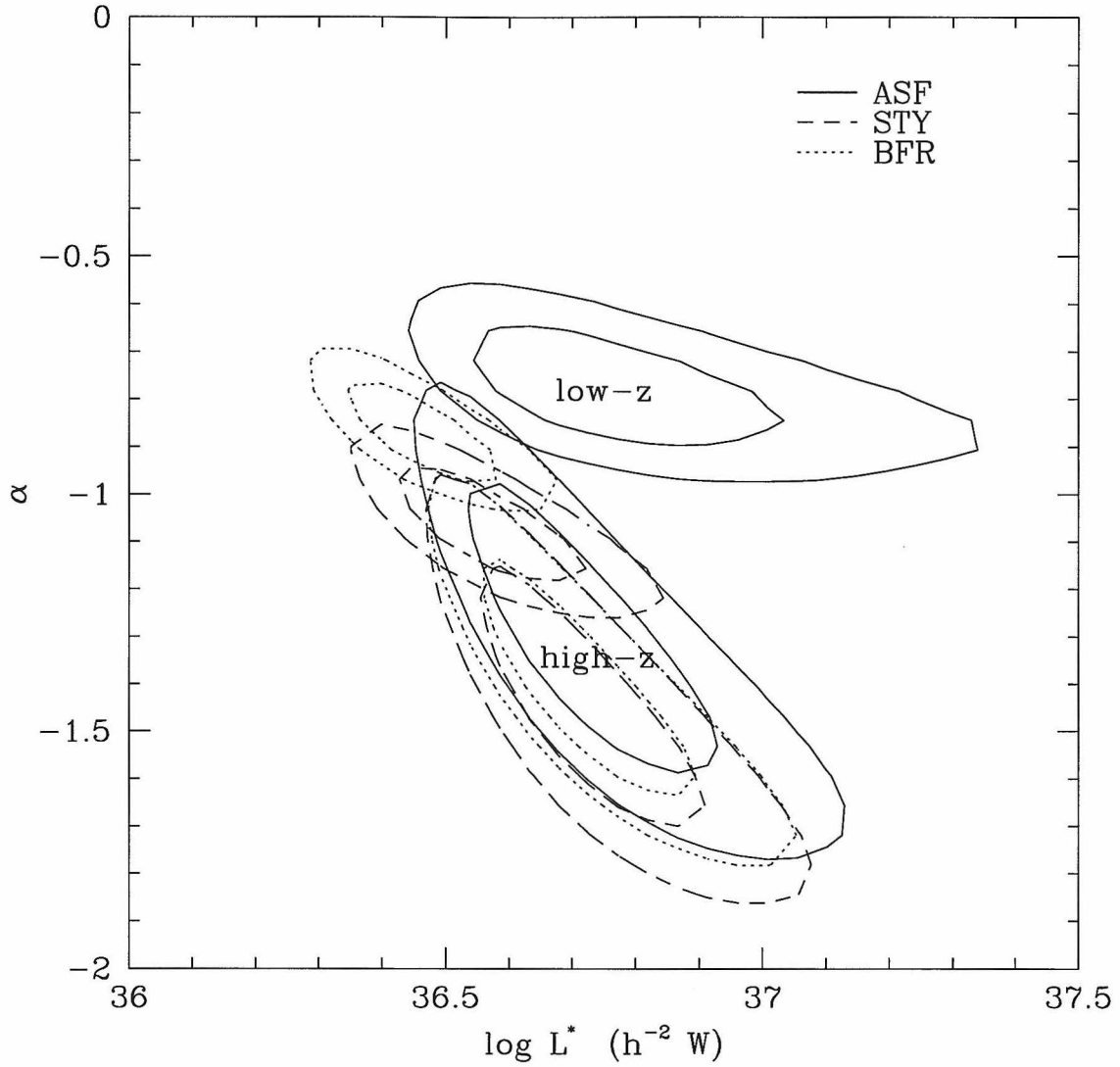
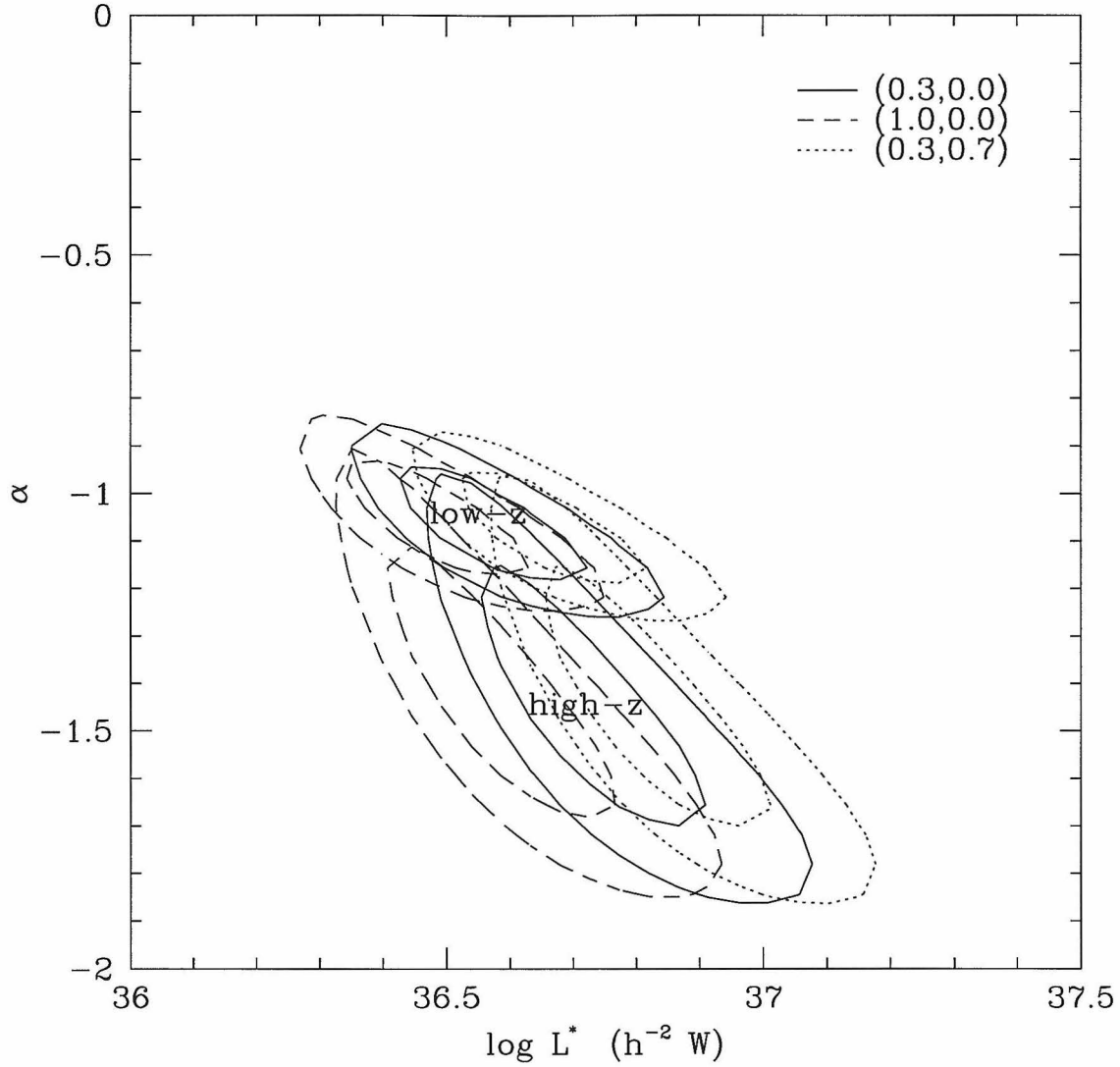
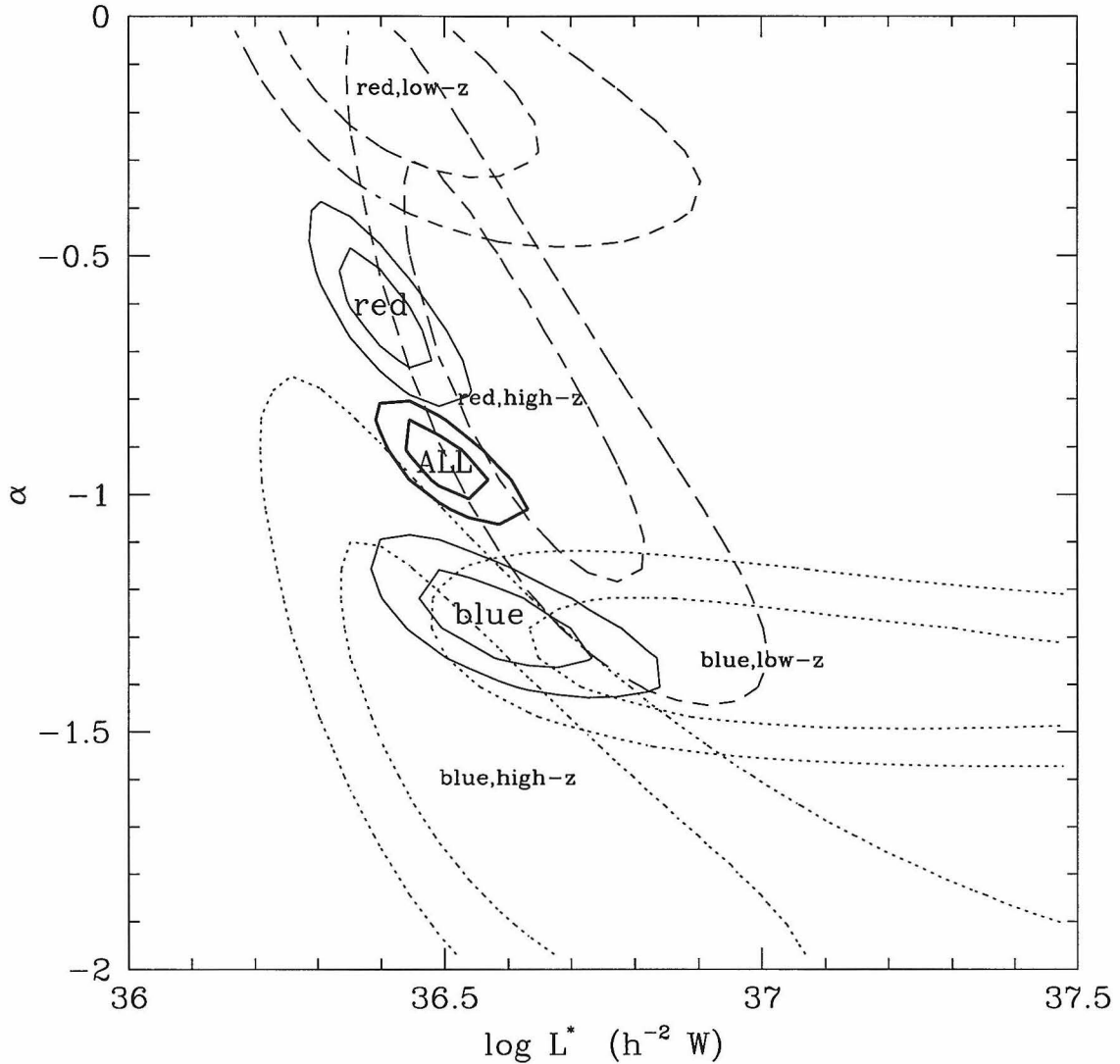


Figure 5.6: Maximum-likelihood results for the B -band galaxy luminosity function in the \mathcal{R} -selected HDF sample as a function of redshift. The low and high-redshift samples are $0 < z < 0.6$ and $0.6 < z < 1.5$, respectively. The three sets of contours are for the three maximum-likelihood methods, ASF, STY and BFR, described in the text. The contours outline one and two-sigma confidence regions. The Hubble constant is taken to be $100 h \text{ km s}^{-1} \text{ Mpc}^{-1}$ in world model $(\Omega_M, \Omega_\Lambda) = (0.3, 0.0)$.



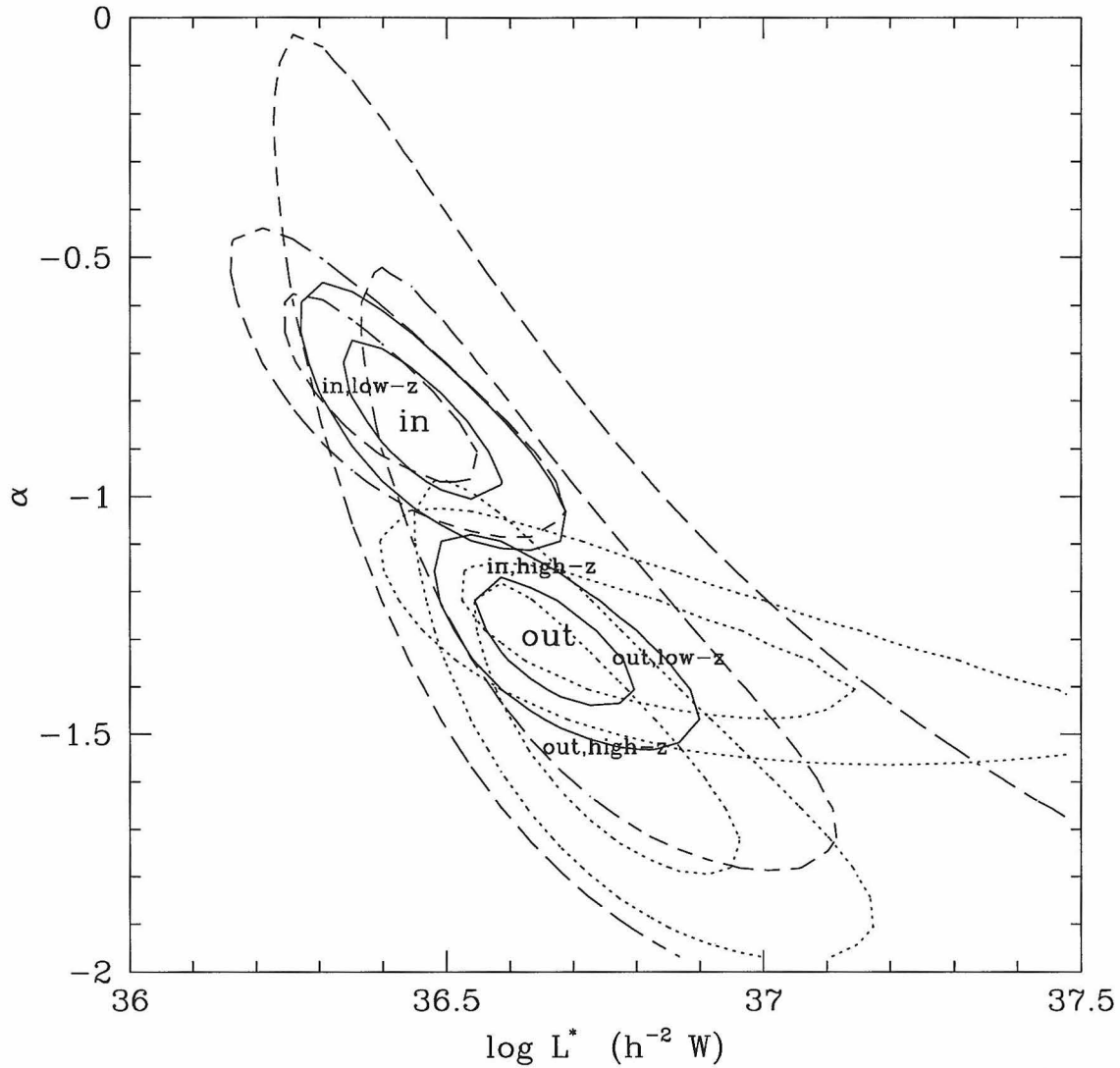
Sep 30 09:52:24 1997

Figure 5.7: World-model dependence of the STY maximum-likelihood results for the B -band galaxy luminosity function in the \mathcal{R} -selected HDF sample as a function of redshift. The low and high-redshift samples are just as in Figure 5.6, but here the three sets of contours are for three different world models, $(\Omega_M, \Omega_\Lambda) = (0.3, 0.0)$, $(1.0, 0.0)$ and $(0.3, 0.7)$. The contours outline one and two-sigma confidence regions. The Hubble constant is taken to be $100 h \text{ km s}^{-1} \text{ Mpc}^{-1}$.



Sep 30 09:53:14 1997

Figure 5.8: ASF maximum-likelihood results for the B -band galaxy luminosity function in the \mathcal{R} -selected HDF sample, as a function of color and redshift. The contours show one and two-sigma confidence regions. The heavy solid lines are for the entire sample, while the light solid lines are for red and blue halves, divided at spectral energy distribution $\nu S_\nu \propto \nu^{-1.5}$ in the spectral vicinity of the B band. The dotted and dashed lines are for samples also split by redshift, with “low- z ” being $0 < z < 0.6$ and “high- z ” being $0.6 < z < 1.5$. The Hubble constant is taken to be $100 h \text{ km s}^{-1} \text{ Mpc}^{-1}$ in world model $(\Omega_M, \Omega_\Lambda) = (0.3, 0.0)$. The ASF method is described in the text; it was chosen because it does not depend on an accurate estimate of the selection function, which can be non-trivial for color-selected samples.



Sep 30 09:52:59 1997

Figure 5.9: STY maximum-likelihood results for the B -band galaxy luminosity function in the \mathcal{R} -selected HDF sample, as a function of environment and redshift. The “in” sample consists of galaxies which have two or more companions in the field within 1000 km s^{-1} (rest-frame velocity difference), *i.e.*, galaxies in groups, and the “out” sample consists of all other galaxies. The contours show one and two-sigma confidence regions. The light solid lines are for the in and out samples; the dotted and dashed lines are for samples also split by redshift, with “low- z ” being $0 < z < 0.6$ and “high- z ” being $0.6 < z < 1.5$. The Hubble constant is taken to be $100 h \text{ km s}^{-1} \text{ Mpc}^{-1}$ in world model $(\Omega_M, \Omega_\Lambda) = (0.3, 0.0)$. The STY method is described in the text; it was chosen because it is not affected by redshift-space structure, which the “in” and “out” sample selection emphasizes.

Chapter 6 The evolution of field galaxies

This thesis opened with a “number problem”: There are far more faint galaxies observed in deep images than would be predicted from measurements of the local galaxy number density and standard cosmological world models. Has the number problem been resolved by the results of this thesis? No. However, the available space of resolutions has been restricted. This final Chapter presents a more detailed picture of how the Universe might behave, consistent with the available information from this thesis and elsewhere. The reader be warned: these are speculations, constrained by observations and guided by a principle that any speculation should be subject to observational test in the near future, but speculations nonetheless.

Perhaps the primary reason the number problem could not be directly resolved here is that this thesis presents results of a spectroscopic survey of faint galaxies with fluxes $\mathcal{R} < 24.5$ mag, whereas the number problem only becomes extremely severe at flux levels $\mathcal{R} > 25$ mag. So these observations represent only the “tip of the iceberg” where the hope was that we could get some idea of what is happening to the huge mass under the water by observing carefully what little lies above the surface. What these observations show is that out to redshifts around unity, there is very little evolution in the numbers or broadband luminosity distribution of bright (within an order of magnitude of L^*) galaxies (Chapter 5). It is worth emphasizing that it has not been shown that individual bright galaxies are maintaining their broadband luminosities; it has only been shown that as a class, the luminosity distribution remains constant.

Previous surveys, similar to that presented in this thesis, have suggested that the luminosity function was steeper, *i.e.*, more dwarf-rich, at high redshift; it has only developed into its local “flat” (constant number per log luminosity at the faint end) shape since $z \approx 0.5$ (Broadhurst *et al.* 1992; Lilly *et al.* 1995; Ellis *et al.* 1996). None of these studies show the effect with tremendous significance, but their results are certainly consistent with that picture, as are the results presented in Chapter 5.

The flattening of the luminosity function with time (or steepening with redshift) is the most natural explanation for the following two observational trends, taken in conjunction: (1) The number counts in visual or near-visual bands increase at the faint end by a factor of between 1.5 and 2 per magnitude. (2) The median redshift found in deep, flux-limited redshift surveys is not a strong function of the limiting flux. If the luminosity function showed no evolution, so it has had its local shape and normalization for all cosmic time, the faint end of the number counts ought to be flat (constant number per unit log flux) at the faint end. The essential reason is that the total volume of the visible Universe (at least to reasonable redshift) is finite at a few Hubble Volumes for reasonable cosmological world models (Appendix B) so at very faint levels, a telescope is not really seeing to greater and greater volumes, it is really just seeing further down the luminosity function. That is, if the faint end of the luminosity function is flat, the very faint end of the number counts also ought to be flat. This is less true in lower density Universes, but with the advent of the extremely deep Hubble Deep Field data (Williams *et al.* 1996), the number counts are inconsistent with a no-evolution model even in an empty or cosmological-constant-dominated Universe. That is just a reiteration of the number problem. Now, to make the counts rise at the faint end, the normalization, characteristic luminosity, or slope of the luminosity function can be changed. If the counts are made steep by evolution in either the normalization or the characteristic luminosity, however, fainter samples are being viewed at greater distance and a strong flux-redshift relation is created. But no strong flux-redshift trend is found, in the sense that median redshift is not a strong function of redshift survey limiting magnitude. The median redshift has been about a half for all deep surveys since the late eighties (Broadhurst *et al.* 1988), despite several magnitudes improvement in survey depth. This implies that at faint levels, sources are, by and large, being observed further down the luminosity function rather than further away. In this case, the faint end of the counts is the faint end of the luminosity function and the best model is that in the past the luminosity function had faint end slope in the range $-2.0 < \alpha < -1.5$, where α is defined by $\phi(L) \propto L^\alpha$ at the faint end (Chapter 4).

Of course there is a high-redshift tail to the redshift distribution the significance of which does indeed depend on the flux limit of the survey; it is this for example that is being observed in the U -band dropout $z > 3$ galaxy samples (Steidel *et al.* 1996). The increasing significance of this tail as the flux limit is decreased does affect the median redshift. Really it is the mode (most likely) redshift which is predicted to be constant with flux limit. This is the strongest observationally accessible prediction of this model of the excess number counts. In addition, of course, inferred luminosity functions, even from a sample like that presented in this thesis but with better statistics, should show a statistically significant evolutionary trend. In principle the redshift distribution can also be determined with gravitational lens statistics, but such tests tend to be more sensitive to the population in the tail at high redshift than the bulk at intermediate. Two pieces of evidence which very weakly support the steep luminosity function explanation of the number problem are that the faint galaxies are on average more morphologically irregular and bluer than local, bright galaxies (see references in Chapter 1). These trends support the steep luminosity function explanation because it makes the excess out of intrinsically faint sources at moderate redshift; in the local Universe, intrinsically faint galaxies are on average more irregular and bluer than bright galaxies (*e.g.*, Marzke *et al.* 1994; Marzke & da Costa 1997).

But this explanation of the number problem is purely phenomenological; it only says that there was a higher fraction of dwarf galaxies in the past than there is locally at the present day; it does not say what happened to those galaxies. There are several reasonable explanations, all discussed at some length in Chapter 1. The faint galaxies could have faded away to non-detectibility. They could have merged into bigger, brighter galaxies. Multiple sources counted as individual faint galaxies could in fact just be the highest surface-brightness spots in larger galaxies and therefore “over-counted.” At some level, all of these processes must be occurring. However, for several reasons, it is difficult to make fading the dominant process. If galaxies fade away because of the evolution of their stellar populations, fainter sources are expected to be redder and excess counts are expected in the infrared, in contrast to

the observations, which have now been pushed to extremely faint levels (*e.g.*, Hogg *et al.* 1997). Also, the bivariate distribution of galaxies in magnitude and color is inconsistent with any reasonable fading scenario (Hogg & Blandford in preparation).

The best bet for removing the dwarfs is probably merging, although it should be noted that merging scenarios are similar to those in which multiple faint sources seen in the image are in fact merely high surface-brightness features in more extended galaxies and therefore what are individual extended galaxies are getting counted multiple times. These scenarios are similar because they both get rid of the dwarfs by having what are now local, bright galaxies subsume multiple faint, distant galaxies over the course of their lives. Merging has been argued against on the basis of a continuity argument: if the correlation function observed for faint galaxies is supported by continuous infall and the infalling pieces have reasonable mass-to-light ratios, the total mass accreted by a typical bright galaxy by the present day would have to be immense (Colley *et al.* 1997). However, that argument depends on assumed typical mass-to-light ratios; in fact, these are a very strong function of age and stellar population and are subject to the important observational bias that brighter sources are easier to observe. As for the multiple components per galaxy scenario, one argument in its favor is that the apparently small faint galaxy half-light radii may be underestimated because the night sky level is mis-estimated. If the outskirts of galaxies extend far enough, all faint galaxies in fact overlap and produce a uniform background which is essentially indistinguishable from sky and therefore not attributed to the extragalactic Universe. Evidence for this is coming from measurements of the extragalactic background light (Bernstein 1998) and simulations of faint images (Hogg & Bernstein in preparation). Faint galaxies would then extend over much larger angular areas than has been thought up to now and multiple components within arcseconds of one another could easily lie within the same low-lying individual galaxy isophote.

These scenarios would be confirmed if redshift surveys much deeper than what is currently possible always found multiple sources at extremely close redshifts. Perhaps narrow-band imaging could be used in advance of huge improvements in spectroscopy; the faint sources are blue and ought to show emission lines. The merging and multi-

component scenarios could in principle be distinguished with detailed observations of close pairs; is the distribution of separations and velocities consistent with massive objects merging or just quiescent orbits in a mature galaxy? In practice the two scenarios are very difficult to differentiate. In the very far future there may be spectrographs capable of measuring internal velocity dispersions or rotation curves for these faint sources; such measurements could make the distinction easily.

Of course it is not necessary to wring one's hands over the lack of dwarfs locally if for some observational-bias reason the local luminosity function is wrong, simply missing the majority of intrinsically faint galaxies. This idea has been suggested by the discovery of galaxies with a wide range of central surface brightnesses, and in particular galaxies with surface brightnesses so low that they ought to go undetected by local surveys. In fact a correlation has been found between the number density of galaxies inferred from redshift surveys and their limiting surface brightness sensitivities, bolstering this idea (Dalcanton in preparation). It is certainly disturbing that all very faint, CCD-based redshift surveys find a higher total number density in the local Universe than bright, plate-based surveys do (Chapter 4). On the other hand, it appears that the flatness of the faint end is a robust result (*ibid.*), in which case large numbers of dwarfs do have to be disposed-of by the present day. These issues ought to be resolved by the upcoming, massive, CCD-based Sloan Survey.

The redshift peaks found in our survey at redshifts out to unity (Cohen *et al.* 1996a,b) appear to exist in a similar form at least out to redshifts around three (Steidel *et al.* 1997). Either structure in the Universe forms very early or else there is a strong spatial correlation in the galaxy formation rate, *i.e.*, the observed overdensities are merely overdensities of bright objects, not necessarily large overdensities in mass. This can in principle be tested with very high signal-to-noise spectra because galaxies which form together or because of one another or some common cause ought to show similarities in age and metallicity. Already the results of Chapter 3 suggest that some members of the redshift peaks may have identical ages or star formation histories. If this turns out to be true, the planned projects for measuring the power spectrum of mass fluctuations from galaxy positions would have to be carefully analyzed. Of

course once a galaxy has formed, it presumably acts like a “test particle” in the gravitational potential of the large scale structure and therefore still carries useful information.

Finally, the results of this thesis present a new puzzle, which may have a trivial solution. It is found that the broadband luminosity function does not evolve strongly (Chapter 5) whereas the emission-line luminosity function does (Chapter 3). The natural explanation of the evolving emission-line function is that the star formation rate was much higher in the past. But the star formation rate also ought to affect broadband luminosities, especially in the B band, where it has been measured in this study. Perhaps the higher contemporaneous star formation observed in the past exactly makes up for the lower total star formation which has occurred (because there has been less time), keeping the total broadband luminosity constant. A cosmic conspiracy? If so, it is not one over which this particular author will lose a lot of sleep.

References

- Bernstein R. A., 1998, Caltech PhD thesis
- Broadhurst T. J., Ellis R. S. & Shanks T., 1988, The Durham Anglo-Australian Telescope faint galaxy redshift survey, MNRAS 235 827
- Cohen J. G., Hogg D. W., Pahre M. A. & Blandford R., 1996a, Strong redshift clustering of distant galaxies, ApJ 462 L9
- Cohen J. G., Cowie L. L., Hogg D. W., Songaila A., Blandford R., Hu E. M. & Shopbell P., 1996b, Redshift clustering in the Hubble Deep Field, ApJ 471 L5
- Colley W. N., Gnedin O. Y., Ostriker J. P. & Rhoads J. E., 1997, Dynamics of “small galaxies” in the Hubble Deep Field, ApJ 488 579
- Ellis R. S., Colless M., Broadhurst T., Heyl J. & Glazebrook K., 1996, Autofib Redshift Survey I: Evolution of the galaxy luminosity function, MNRAS 280 235
- Hogg D. W., Neugebauer G., Armus L., Matthews K., Pahre M. A., Soifer B. T. & Weinberger A. J., 1997, Near infrared imaging of the Hubble Deep Field with the Keck Telescope, AJ 113 474
- Lilly S. J., Tresse L., Hammer F., Crampton D. & Le Fevre O., 1995, The Canada-France redshift survey VI: Evolution of the galaxy luminosity function to $z \sim 1$, ApJ 455 108
- Marzke R. O., Geller M. J., Huchra J. P. & Corwin H. G., 1994, The luminosity

- function for different morphological types in the CfA redshift survey, *AJ* 108 437
- Steidel C. C., Giavalisco M., Pettini M., Dickinson M., Adelberger K. L., 1996, Spectroscopic Confirmation of a Population of Normal Star-forming Galaxies at Redshifts $z > 3$, *ApJ* 462 L17
- Steidel C. C., Adelberger K. L., Dickinson M., Giavalisco M., Pettini M. & Kellogg M., 1997, A large structure of galaxies at redshift $z \sim 3$ and its cosmological implications, *ApJ* in press

Appendix A Magnitude systems

A.1 Vega-relative magnitudes

The system of *apparent magnitudes*, or simply *magnitudes*, is a logarithmic flux scale, defined such that the standard star Vega has magnitude zero in all bands. If Vega has flux S_0 in some band, an object with flux S is assigned the magnitude $m = -2.5 \log(S/S_0)$. Brighter objects have smaller magnitudes. The magnitude definitions and absolute calibrations (*i.e.*, zeropoints or Vega fluxes) used in this dissertation are given in Table A.1.

Magnitudes are designed for relative measurements, which, given the poorly understood, constantly changing properties of the atmosphere, are the only robust and precise measurements possible with groundbased telescopes. While it is straightforward (if, perhaps, not easy) to measure the relative fluxes of two astronomical objects at an accuracy of 10^{-3} , it is very difficult to measure an absolute flux to better than about 5 percent. Any such measurement requires accounting for absorption by the Earth’s atmosphere (which is time- and airmass-dependent) and a precise “laboratory” calibration of the instrument plus telescope system used to detect the light. For this reason, the absolute calibrations given in Table A.1 should be taken to be approximate. An additional reason for caution is that the data in Table A.1 are largely from secondary sources.

As an added bonus, the calibration chart used by Neugebauer (private communication) is given in Table A.2. The differences between Tables A.1 and A.2 are small, even though they are based on at least partially independent information.

A.2 A note on absolute calibration

Actually, the problem with absolute flux calibration of photometry goes deeper than the simple fact, mentioned in the previous Section, that it is difficult to measure. The flux calibrations given in Tables A.1 and A.2 in fact contain an arbitrary convention:

The absolute calibration of the magnitude systems (the $S_{\nu}^{(0)}$ values in Table A.1) are given in terms of a flux density (flux per unit log frequency), which is defined only at a single point in the spectrum, while any photometric bandpass in fact has a finite width, and probably a non-trivial profile. In practice, for each bandpass, an effective wavelength λ_{eff} is chosen, at which the zeropoint is correct. How does one compute λ_{eff} for a given bandpass? Should one take the mean of the transmission function? If so, in wavelength space or frequency space or log-frequency space? Different choices give different results. Once a choice has been made, the calibration will only be exactly correct (in the sense that the true S_{λ} of the source at λ_{eff} equals the photometrically-inferred value) for one particular spectral shape; all other spectral shapes will require a color-correction. For example, a very red object might have all its flux in a bandpass coming from the very reddest ten percent of the bandpass, or even from a part of a long wavelength tail caused by a “red leak” in the filter. For another, a source might be emitting all its flux in a single narrow line which does not happen to lie exactly at λ_{eff} . In practice, with visual and near-infrared bandpasses, these color-corrections are usually small because source spectra tend to be well-behaved and the usual bandpasses tend to be relatively narrow. However, this is a fundamental limitation to the absolute calibration of broadband photometric bandpasses, and another reason to treat all absolute calibrations with caution.

Of course this ambiguity can be seen as a blessing. Given a bandpass, absolute calibration merely requires the (arbitrary?) choice of a λ_{eff} and someone else’s painstakingly measured flux density $\log \lambda S_{\lambda}$ of Vega at that wavelength. The best absolute calibration of Vega in the visual as of this dissertation is due to Hayes (1985) and shown in Figure A.1; it is what was used to calibrate the photographic and Gunn bandpasses in Table A.1.

A.3 Absolute magnitudes

The absolute magnitude M is a measure of luminosity. It is the apparent magnitude the object would have if it were at 10 pc distance, so

$$M = m - 5 \log \left(\frac{D}{10 \text{ pc}} \right) \quad (\text{A.1})$$

where D is the distance to the object (ignoring k-correction and other issues discussed in Appendix B). Because Vega is roughly at 10 pc distance, this system is also more-or-less Vega-relative. Because all observable extragalactic objects are far more luminous than Vega, their absolute magnitudes will all be negative.

To convert the flux calibrations given in Table A.1 into luminosity calibrations, *i.e.*, log luminosities $\log(\nu L_\nu^{(0)})$, in Watts, of an absolute magnitude $M = 0$ object, simply add the logarithm of $4\pi(10 \text{ pc})^2$ in meters, or 36.08.

A.4 “AB” magnitudes

The “AB” magnitude system was designed to have absolute calibrations which are the same in f_ν for all bands, instead of having calibrations equal to the flux of Vega in each band. By definition, AB and Vega-relative magnitudes are equal in the V band. Note that construction of the AB system requires absolute calibration of the magnitude scales, so correct AB magnitudes cannot be known any better than the flux calibrations, despite the fact that Vega-relative magnitudes can be known to arbitrary accuracy. This fact alone recommends against using AB magnitudes except in special circumstances. Furthermore, as discussed above, there is a conventional or arbitrary component to the flux calibration!

To compute an AB calibration in the units employed in Table A.1, take the V -band calibration, add $\log \nu$ for the band in question, and subtract $\log \nu$ for the V band. So, for instance, the K_{AB} calibration is $\log(\nu S_\nu^{(0)}) = -8.31$ (in W m^{-2}).

A.5 Transformations between magnitudes

Frequently a transformation between different magnitudes is required, for example when the V and I -band magnitudes of a source are known and the R -band needs to be predicted. In this case some assumption needs to be made about the spectral energy distribution of the source. For extragalactic work the best assumption is that the distribution is a power law, $\nu f_\nu \propto \nu^n$. Then, to a reasonable approximation, the R -band flux can be found by interpolating between the V and I -band fluxes (found using the absolute calibrations of the V and I bands) on a log-log plot. The R -band absolute calibration is then applied to get an R -band magnitude. This procedure generalizes to the following rule:

To get the best estimate of a magnitude m_C in band C given magnitudes m_A and m_B in bands A and B , use

$$m_C = a m_A + b m_B + c \quad (\text{A.2})$$

where

$$a = \frac{\log \nu_C - \log \nu_B}{\log \nu_A - \log \nu_B} \quad (\text{A.3})$$

$$b = \frac{\log \nu_A - \log \nu_C}{\log \nu_A - \log \nu_B} \quad (\text{A.4})$$

$$c = -2.5(a Z_A + b Z_B - Z_C) \quad (\text{A.5})$$

where the $\log \nu_i$ are the effective wavelengths of each band i and the Z_i are the absolute calibrations $\log[\nu f_\nu^{(0)}]$.

Acknowledgments

Thanks go to Gerry Neugebauer for providing zeropoints and for pointing out the fundamental ambiguity in absolute calibration.

References

- Fukugita M., Shimasaku K. & Ichikawa T., 1995, Galaxy colors in various photometric band systems, *PASP* 107 945
- Hayes D. S., 1985, Stellar absolute fluxes and energy distributions from 0.32 to 4.0 μm , in Hayes D. S. *et al.* eds., *Proc IAU 111: Calibration of Fundamental Stellar Quantities*, Kluwer, Dordrecht, 225
- Holtzman J. A., Burrows C. J., Casertano S., Hester J. J., Trauger J. T., Watson A. M. & Worthey G., 1995, The photometric performance and calibration of WFPC2, *PASP* 107 1065
- Steidel C. C. & Hamilton D., 1993, Deep imaging of high redshift QSO fields below the Lyman limit II: Number counts and colors of field galaxies, *AJ* 105 2017
- Zombeck M. V., 1990, *Handbook of Space Astronomy and Astrophysics*, Cambridge University, Cambridge

band	λ_{eff} (μm)	$\Delta\lambda$ (μm)	$\log \nu$ (Hz)	$\log \nu S_{\nu}^{(0)}$ (W m^{-2})
<i>F300W</i>	0.29	0.073	15.01	−7.98
<i>U_n</i>	0.36		14.92	−7.89
<i>U</i>	0.365	0.068	14.91	−7.81
<i>B</i>	0.44	0.098	14.83	−7.54
<i>F450W</i>	0.45	0.096	14.82	−7.54
<i>B_J</i>	0.46	0.15	14.81	−7.56
<i>G</i>	0.48		14.80	−7.61
<i>V</i>	0.55	0.089	14.74	−7.70
<i>F606W</i>	0.59	0.15	14.71	−7.77
<i>r</i>	0.65	0.089	14.66	−7.86
<i>R</i>	0.69		14.64	−7.92
<i>R</i>	0.70	0.22	14.63	−7.91
<i>F814W</i>	0.79	0.15	14.58	−8.03
<i>I</i>	0.90	0.24	14.52	−8.12
<i>J</i>	1.25	0.3	14.38	−8.40
<i>H</i>	1.65	0.4	14.26	−8.71
<i>K_s</i>	2.15	0.3	14.14	−9.01
<i>K</i>	2.2	0.4	14.13	−9.04
<i>L</i>	3.6	1.2	13.92	−9.65

Table A.1: The Vega-relative magnitude wavelengths, frequencies and absolute calibrations used in this dissertation. The full width (*i.e.*, not half width) of the bandpass is symbolized $\Delta\lambda$. Frequencies are given in Hz and absolute calibrations are given in flux per unit ln wavelength $\nu S_{\nu} = \lambda S_{\lambda}$. Data for the custom HST bandpass magnitudes (*F300W etc.*) are from Holtzman *et al.* (1995). Data for *U_n*, *G* and *R* are from Steidel & Hamilton (1993; where the Vega-relative calibration on their AB system is given with the wrong sign—when corrected it provides the above calibrations). Filter information for *B_J* and *r* are from Fukugita *et al.* (1995), while the calibrations are my own calculation (using data in Hayes 1985 and the method described in Section A.2). Filter information for *K_s* come from Neugebauer (private communication) and the calibration from assuming that Vega is a hot blackbody in the region of the *K* band. Data for the remaining Johnson magnitudes are from a (very) secondary source (Zombeck 1990). No calibration should be treated with any more respect than it deserves (see text).

11 Dec 81, GXN
updated 9 Mar 97

ABSOLUTE CALIBRATION

Band	lam eff mu	log[nu] log[Hz]	Zero magnitude				m0	notes
			flam	fnu	log[fnu]			
			1E-11 W/m2	Jy mu		lg[W/m2Hz]		
U	0.36	14.92	3980	1720	-22.76	15.59	1	
B	0.43	14.84	7285	4490	-22.35	16.63	1	
V	0.548	14.74	3526	3530	-22.45	16.37	2	
R	0.7	14.63	1702	2780	-22.56	16.11	1	
I	0.9	14.52	830	2240	-22.65	15.88	1	
J	1.25	14.38	303	1578	-22.80	15.50	2	
H	1.65	14.26	115	1041	-22.98	15.04	2	
K	2.2	14.13	40	646	-23.19	14.53	2	
L	3.5	13.93	6.8	278	-23.56	13.61	2	
L'	3.7	13.91	5.5	251	-23.60	13.50	2	
M	4.8	13.80	2.02	155	-23.81	12.98	2	
N	10.1	13.47	0.109	37	-24.43	11.42	3	
O	20.2	13.17	0.0074	10	-25.00	10.00	3	

AB == -2.5 * log f nu - 56.13
log[f nu(mJy)] == (m0 - m)*0.4

Vega defined as 0 Mag for V and 1.25 <= lambda <= 4.8 mu.

- 1) Hayes 1979, Dudley Obs. RN. 14, 297.
- 2) Vega flux from Oke and Schild 1970, Ap.J., 161, 1015.
Kurucz, Peytreman and Avrett model 1972.
- 3) Becklin 1972 calibration.

Table A.2: Vega-relative magnitude wavelengths, frequencies and zeropoints according to Neugebauer (private communication).

Mar 27 14:07:34 1997

Hayes (1985) absolute spectrum of Vega

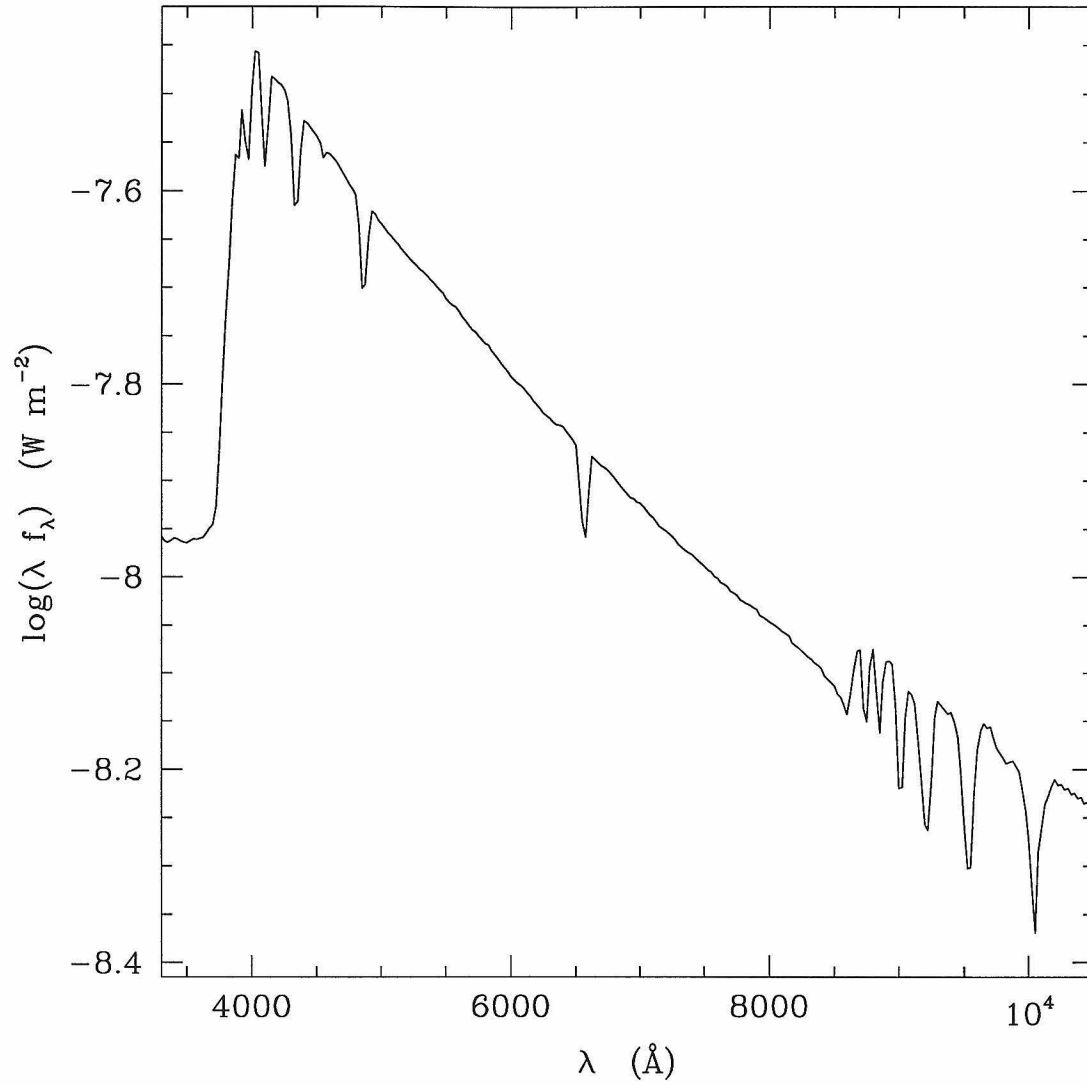


Figure A.1: The Hayes (1985) calibrated spectrum of Vega, plotted in $\log \lambda S_\lambda = \log \nu S_\nu$, in SI units. As described in the text, Vega-relative broadband photometry can be calibrated with this spectrum.

Appendix B Distance measures in cosmology

B.1 Introduction

In cosmology (or to be more specific, *cosmography*, the measurement of the Universe) there are many ways to specify the distance between two points, because in the expanding Universe, the distances between comoving objects are constantly changing, and Earth-bound observers look back in time as they look out in distance. The unifying aspect is that all distance measures somehow measure the separation between events on radial null trajectories, i.e., trajectories of photons which terminate at the observer.

In this note, formulae for many different cosmological distance measures are provided. I treat the concept of “distance measure” very liberally, so, for instance, the lookback time and comoving volume are both considered distance measures. The bibliography of source material can be consulted for derivations; this is merely a “cheat sheet.” *C* routines (KR) which compute all of these distance measures are available from the author upon request. Comments and corrections are highly appreciated, as are acknowledgments in research that makes use of this summary or code.

B.2 Cosmographic parameters

The *Hubble constant* H_0 is the constant of proportionality between recession speed v and distance d in the expanding Universe;

$$v = H_0 d \tag{B.1}$$

The subscripted “0” refers to the present epoch because in general H changes with time. The dimensions of H_0 are inverse time, but it is usually written

$$H_0 = 100 h \text{ km s}^{-1} \text{ Mpc}^{-1} \quad (\text{B.2})$$

where h is a dimensionless number parameterizing our ignorance. The inverse of the Hubble constant is the *Hubble time* t_H

$$t_H \equiv \frac{1}{H_0} = 9.78 \times 10^9 h^{-1} \text{ yr} = 3.09 \times 10^{17} h^{-1} \text{ s} \quad (\text{B.3})$$

and the speed of light c times the Hubble time is the *Hubble distance* D_H

$$D_H \equiv \frac{c}{H_0} = 3000 h^{-1} \text{ Mpc} = 9.26 \times 10^{25} h^{-1} \text{ m} \quad (\text{B.4})$$

These quantities set the scale of the Universe, and often cosmologists work in geometric units with $c = t_H = D_H = 1$.

The mass density ρ of the Universe and the value of the cosmological constant Λ are dynamical properties of the Universe, affecting the time evolution of the metric, but in these notes we will treat them as purely kinematic parameters. They can be made into dimensionless density parameters Ω_M and Ω_Λ by

$$\Omega_M \equiv \frac{8\pi G \rho_0}{3 H_0^2} \quad (\text{B.5})$$

$$\Omega_\Lambda \equiv \frac{\Lambda}{3 H_0^2} \quad (\text{B.6})$$

(Peebles, 1993, pp. 310–313), where the subscripted “0”s indicate that the quantities (which in general evolve with time) are to be evaluated at the present epoch. A third density parameter Ω_R measures the “curvature of space” and can be defined by the relation

$$\Omega_M + \Omega_\Lambda + \Omega_R = 1 \quad (\text{B.7})$$

These parameters totally determine the geometry of the Universe if it is homogeneous,

isotropic, and matter-dominated. By the way, the critical density $\Omega = 1$ corresponds to $7.5 \times 10^{21} h^{-1} M_{\odot} D_H^{-3}$, where M_{\odot} is the mass of the Sun.

Most theorists believe that it is in some sense “unlikely” that all three of these density parameters be of the same order, and we know that Ω_M is significantly larger than zero, so many guess that $(\Omega_M, \Omega_{\Lambda}, \Omega_R) = (1, 0, 0)$, with $(\Omega_M, 1 - \Omega_M, 0)$ and $(\Omega_M, 0, 1 - \Omega_M)$ tied for second place. If $\Omega_{\Lambda} = 0$, then the *deceleration parameter* q_0 is just half Ω_M , otherwise q_0 is not such a useful parameter. When I perform cosmographic calculations and I want to cover all the bases, I use the three world models

name	Ω_M	Ω_{Λ}
Einstein-de Sitter	1	0
low density	0.05	0
high lambda	0.2	0.8

These three models push the observational limits.

B.3 Redshift

The *redshift* z of an object is the fractional doppler shift of its emitted light resulting from radial motion

$$z \equiv \frac{\nu_e}{\nu_o} - 1 = \frac{\lambda_o}{\lambda_e} - 1 \quad (\text{B.8})$$

where ν_o and λ_o are the observed frequency and wavelength, and ν_e and λ_e are the emitted. Redshift is related to radial velocity v by

$$1 + z = \sqrt{\frac{1 + v/c}{1 - v/c}} \quad (\text{B.9})$$

where c is the speed of light. The difference between an object’s measured redshift and its *cosmological redshift* is due to its (radial) *peculiar velocity*; i.e., we define the cosmological redshift as that part of the redshift due solely to the expansion of the Universe, or *Hubble flow*. In terms of cosmography, the cosmological redshift is

directly related to the scale factor $a(t)$, or the “size” of the Universe. For an object at redshift z

$$1 + z = \frac{a(t_o)}{a(t_e)} \quad (\text{B.10})$$

where $a(t_o)$ is the size of the Universe at the time the light from the object is observed, and $a(t_e)$ is the size at the time it was emitted.

For small v/c , or small distance d , in the expanding Universe, the velocity is proportional to the distance (and all the distance measures, e.g., angular diameter distance, luminosity distance, etc., converge); taking the linear approximation this reduces to

$$z \approx \frac{v}{c} = \frac{d}{D_H} \quad (\text{B.11})$$

where D_H is the Hubble distance (see above). But this is *only true for small redshifts!*

Redshift is almost always determined with respect to us (or the frame centered on us but stationary with respect to the microwave background), but it is possible to define the redshift z_{12} between objects 1 and 2, both of which are cosmologically redshifted relative to us: the redshift z_{12} of an object at redshift z_2 relative to a hypothetical observer at redshift $z_1 < z_2$ is given by

$$1 + z_{12} = \frac{a(t_1)}{a(t_2)} = \frac{1 + z_2}{1 + z_1} \quad (\text{B.12})$$

B.4 Comoving distance (line-of-sight)

A small *comoving distance* δD_C between two nearby objects in the Universe is the distance between them which remains constant with epoch if the two objects are moving with the Hubble flow. In other words, it is the distance between them which would be measured with rulers at the time they are being observed (the *proper distance*) divided by the ratio of the scale factor of the Universe then to now. In other words the proper distance multiplied by $(1 + z)$. The total line-of-sight comoving distance D_C from us to a distant object is computed by integrating the infinitesimal δD_C contributions between nearby events along the radial ray from $z = 0$ to the object.

Following Peebles (1993, pp. 310–321) (who calls the transverse comoving distance by the very confusing name “angular size distance,” which is *not* the same as “angular diameter distance” introduced below), we define the function

$$E(z) \equiv \sqrt{\Omega_M (1+z)^3 + \Omega_R (1+z)^2 + \Omega_\Lambda} \quad (\text{B.13})$$

which is proportional to the time derivative of the logarithm of the scale factor (i.e., $\dot{a}(t)/a(t)$), with z redshift and the three density parameters defined as above. Since $dz = da$, $dz/E(z)$ is proportional to the time-of-flight of a photon traveling across the redshift interval dz , divided by the scale factor at that time. Since the speed of light is constant, this is a proper distance divided by the scale factor, which is the definition of a comoving distance. The total line-of-sight comoving distance is then given by integrating these contributions, or

$$D_C = D_H \int_0^z \frac{dz'}{E(z')} \quad (\text{B.14})$$

where D_H is the Hubble distance defined above.

In some sense the line-of-sight comoving distance is the fundamental distance measure in cosmography since, as will be seen below, all others are quite simply derived in terms of it. The line-of-sight comoving distance between two nearby events (i.e., close in redshift or distance) is the distance which we would measure locally between the events today if those two points were locked into the Hubble flow. It is the correct distance measure for measuring aspects of large-scale structure imprinted on the Hubble flow, e.g., distances between “walls.”

B.5 Comoving distance (transverse)

The comoving distance between two events at the same redshift or distance but separated on the sky by some angle $\delta\theta$ is $D_M \delta\theta$ and the transverse comoving distance D_M (so-denoted for a reason explained below) is simply related to the line-of-sight

comoving distance D_C :

$$D_M = \begin{cases} D_H \frac{1}{\sqrt{\Omega_R}} \sinh \left[\sqrt{\Omega_R} D_C / D_H \right] & \text{for } \Omega_R > 0 \\ D_C & \text{for } \Omega_R = 0 \\ D_H \frac{1}{\sqrt{|\Omega_R|}} \sin \left[\sqrt{|\Omega_R|} D_C / D_H \right] & \text{for } \Omega_R < 0 \end{cases} \quad (\text{B.15})$$

where the trigonometric functions \sinh and \sin account for what is called “the curvature of space.” (Space curvature depends on the particular coordinate system chosen, so it is not intrinsic; a change of coordinates makes space flat; the only intrinsic curvature is space-time curvature, which is related to the local mass-energy density or really stress-energy tensor.) For $\Omega_\Lambda = 0$, there is an analytic solution to the equations

$$D_M = D_H \frac{2[2 - \Omega_M(1 - z) - (2 - \Omega_M)\sqrt{1 + \Omega_M z}]}{\Omega_M^2(1 + z)} \quad \text{for } \Omega_\Lambda = 0 \quad (\text{B.16})$$

(Weinberg, 1972, p. 485; Peebles, 1993, pp. 320–321). Weedman (1986, pp. 59–60) calls this distance measure “proper distance,” which is very bad style¹, and gives the above formula, also for $\Omega_\Lambda = 0$ but in terms of $q_0 = \Omega_M/2$.

(Although these notes follow the Peebles derivation, there is a qualitatively distinct method using what is known as the *development angle* χ , which increases as the Universe evolves. This method is preferred by relativists such as Misner, Thorne & Wheeler 1973, pp. 782–785).

The comoving distance happens to be equivalent to the *proper motion distance* (hence the name D_M), defined as the ratio of the actual transverse velocity (in distance over time) of an object to its proper motion (in radians per unit time) (Weinberg, 1972, pp. 423–424). The proper motion distance is plotted in Figure B.1. Proper motion distance is used, for example, in computing radio jet velocities from knot motion.

¹The word “proper” has a specific use in relativity. The *proper time* between two nearby events is the time delay between the events in the frame in which they take place at the same location, and the *proper distance* between two nearby events is the distance between them in the frame in which they happen at the same time. It is the distance measured by a ruler at the time of observation. The transverse comoving distance D_M is *not* a proper distance—it is a proper distance divided by a ratio of scale factors.

B.6 Angular diameter distance

The *angular diameter distance* D_A is defined as the ratio of an object's physical transverse size to its angular size (in radians). It is used to convert angular separations in telescope images into proper separations at the source. It is famous for not increasing indefinitely as $z \rightarrow \infty$; it turns over at $z \sim 1$ and thereafter more distant objects actually appear larger in angular size. Angular diameter distance is related to the transverse comoving distance by

$$D_A = \frac{D_M}{1+z} \quad (\text{B.17})$$

(Weinberg, 1972, pp. 421–424; Weedman, 1986, pp. 65–67; Peebles, 1993, pp. 325–327). The angular diameter distance is plotted in Figure B.2.

There is also an angular diameter distance D_{A12} between two objects at redshifts z_1 and z_2 , frequently used in gravitational lensing. From a trial-and-error attempt to derive an equation in Blandford & Narayan (1992), I believe that the correct, general formula is

$$D_{A12} = \frac{1}{1+z_2} \left[D_{M2} \sqrt{1 + \Omega_R \frac{D_{M1}^2}{D_H^2}} - D_{M1} \sqrt{1 + \Omega_R \frac{D_{M2}^2}{D_H^2}} \right] \quad (\text{B.18})$$

where D_{C1} and D_{C2} are the transverse comoving distances to z_1 and z_2 , D_H is the Hubble distance, and Ω_R is the curvature density parameter (Peebles, 1993, pp. 336–337).

B.7 Luminosity distance

The *luminosity distance* D_L is defined by the relationship between bolometric (i.e., integrated over all frequencies) flux S and bolometric luminosity L :

$$D_L \equiv \sqrt{\frac{L}{4\pi S}} \quad (\text{B.19})$$

It turns out that this is related to the transverse comoving distance and angular diameter distance by

$$D_L = (1 + z) D_M = (1 + z)^2 D_A \quad (\text{B.20})$$

(Weinberg, 1972, pp. 420–424; Weedman, 1986, pp. 60–62). The latter relation follows from the fact that the surface brightness of a receding object is reduced by a factor $(1 + z)^{-4}$, and the angular area goes down as D_A^{-2} . The luminosity distance is plotted in Figure B.3.

If the concern is not with bolometric quantities but rather with differential flux S_ν and luminosity L_ν , as is usually the case in astronomy, then a correction, the *k-correction*, must be applied to the flux or luminosity because the redshifted object is emitting flux in a different band than that in which you are observing. The *k*-correction depends on the spectrum of the object in question, and is unnecessary only if the object has spectrum $\nu L_\nu = \text{constant}$. For any other spectrum the differential flux S_ν is related to the differential luminosity L_ν by

$$S_\nu = (1 + z) \frac{L_{(1+z)\nu}}{L_\nu} \frac{L_\nu}{4\pi D_L^2} \quad (\text{B.21})$$

where z is the redshift, the ratio of luminosities equalizes the difference in flux between the observed and emitted bands, and the factor of $(1 + z)$ accounts for the redshifting of the bandwidth. Similarly, for differential flux per unit wavelength,

$$S_\lambda = \frac{1}{(1 + z)} \frac{L_{\lambda/(1+z)}}{L_\lambda} \frac{L_\lambda}{4\pi D_L^2} \quad (\text{B.22})$$

(Peebles, 1993, pp. 330–331; Weedman, 1986, pp. 60–62). In this author's opinion, the most natural flux unit is differential flux per unit log frequency or log wavelength $\nu S_\nu = \lambda S_\lambda$ for which there is no redshifting of the bandpass so

$$\nu S_\nu = \frac{\nu_e L_{\nu_e}}{4\pi D_L^2} \quad (\text{B.23})$$

where $\nu_e = (1 + z)\nu$ is the emitted frequency.

The *distance modulus* DM is defined by

$$DM \equiv 5 \log \left(\frac{D_L}{10 \text{ pc}} \right) \quad (\text{B.24})$$

because it is the magnitude difference between an object's observed bolometric flux and what it would be if it were at 10 pc (don't ask me, ask an astronomer!). The distance modulus is plotted in Figure B.4. The absolute magnitude M is the astronomer's measure of luminosity, defined to be the apparent magnitude the object in question would have if it were at 10 pc, so

$$m = M + DM + K \quad (\text{B.25})$$

where K is the k-correction

$$K = -2.5 \log \left[(1+z) \frac{L_{(1+z)\nu}}{L_\nu} \right] = -2.5 \log \left[\frac{1}{(1+z)} \frac{L_{\lambda/(1+z)}}{L_\lambda} \right] \quad (\text{B.26})$$

B.8 Parallax distance

If it was possible to measure parallaxes for high redshift objects, the distance so measured would be the *parallax distance* D_P (Weinberg, 1972, pp. 418–420). It may be possible, one day, to measure parallaxes to distant galaxies using gravitational lensing, although in these cases, a modified parallax distance is used which takes into account the redshifts of both the source and the lens (Schneider, Ehlers & Falco, 1992, pp. 508–509), a discussion of which is beyond the scope of these notes.

B.9 Comoving volume

The *comoving volume* V_C is the volume measure in which number densities of non-evolving objects locked into Hubble flow are constant with redshift. It is the proper volume times three factors of the relative scale factor now to then, or $(1+z)^3$. Since the derivative of comoving distance with redshift is $1/E(z)$ (defined above), the angular

diameter distance converts a solid angle $d\Omega$ into a proper area, and two factors of $(1+z)$ convert a proper area into a comoving area, the comoving volume element in solid angle $d\Omega$ and redshift interval dz is

$$dV_C = D_H \frac{(1+z)^2 D_A^2}{E(z)} d\Omega dz \quad (\text{B.27})$$

where D_A is the angular diameter distance at redshift z and $E(z)$ is defined above (Weinberg, 1972, p. 486; Peebles, 1993, pp. 331–333). The comoving volume element is plotted in Figure B.5. The comoving volume element and its integral are both used frequently in predicting number counts or luminosity densities.

B.10 Lookback time

The *lookback time* t_L to an object is the difference between the age t_o of the Universe now (at observation) and the age t_e of the Universe at the time the photons were emitted (according to the object). It is used to predict properties of high-redshift objects with evolutionary models, such as passive stellar evolution for galaxies. Recall that $E(z)$ is the time derivative of the logarithm of the scale factor $a(t)$; the scale factor is proportional to $(1+z)$, so the product $(1+z)E(z)$ is proportional to the derivative of z with respect to the lookback time, or

$$t_L = t_H \int_0^z \frac{dz'}{(1+z')E(z')} \quad (\text{B.28})$$

(Peebles, 1993, pp. 313–315; Kolb & Turner 1990, pp. 52–56, give some analytic solutions to this equation, but they are concerned with the age $t(z)$, so they integrate from z to ∞). The lookback time is plotted in Figure B.6.

B.11 Probability of intersecting objects

Given a population of objects with comoving number density $n(z)$ (number per unit volume) and cross section $\sigma(z)$ (area), what is the incremental probability dP that

a line of sight will intersect one of the objects in redshift interval dz at redshift z ? Questions of this form are asked frequently in the study of QSO absorption lines or pencil-beam redshift surveys. The answer is

$$dP = n(z) \sigma(z) D_H \frac{(1+z)^2}{E(z)} dz \quad (\text{B.29})$$

(Peebles, 1993, pp. 323–325). The dimensionless differential intersection probability is plotted in Figure B.7.

Acknowledgments

Roger Blandford, Ed Farhi, Jim Peebles and Wal Sargent all contributed generously to my understanding of this material and Kurt Adelberger, Lee Armus, Deepto Chakrabarty, Tom Murphy, Gerry Neugebauer and Douglas Scott helped me with various drafts. I thank the NSF for financial support.

References

- Blandford R. & Narayan R., 1992, Cosmological applications of gravitational lensing, *ARA&A* **30** 311–358
- Carroll S. M., Press W. H. & Turner E. L., 1992, The cosmological constant, *ARA&A* **30** 499–542
- Kolb E. W. & Turner M. S., 1990, *The Early Universe*, Addison-Wesley, Redwood City
- Misner C. W., Thorne K. S. & Wheeler J. A., 1973, *Gravitation*, W. H. Freeman & Co., New York
- Peebles P. J. E., 1993, *Principles of Physical Cosmology*, Princeton University Press, Princeton
- Schneider P., Ehlers J. & Falco E. E., 1992, *Gravitational Lensing*, Springer, Berlin
- Weedman D. W., 1986, *Quasar Astronomy*, Cambridge University, Cambridge
- Weinberg S., 1972, *Gravitation and Cosmology: Principles and Applications of the General Theory of Relativity*, John Wiley & Sons, New York

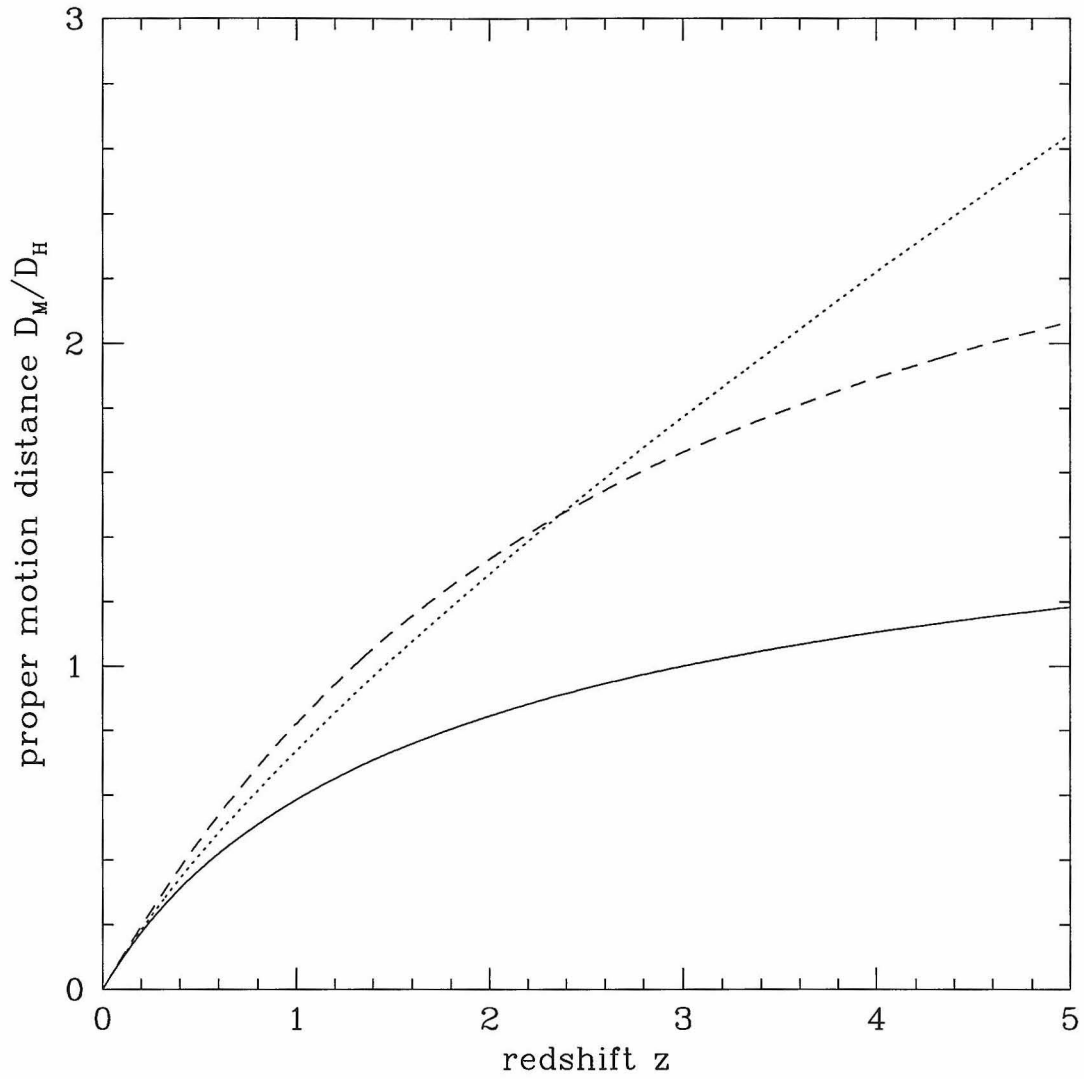


Figure B.1: The dimensionless proper motion distance D_M/D_H . The three curves are for the three world models, Einstein-de Sitter $(\Omega_M, \Omega_\Lambda) = (1, 0)$, solid; low-density, $(0.05, 0)$, dotted; and high lambda, $(0.2, 0.8)$, dashed.

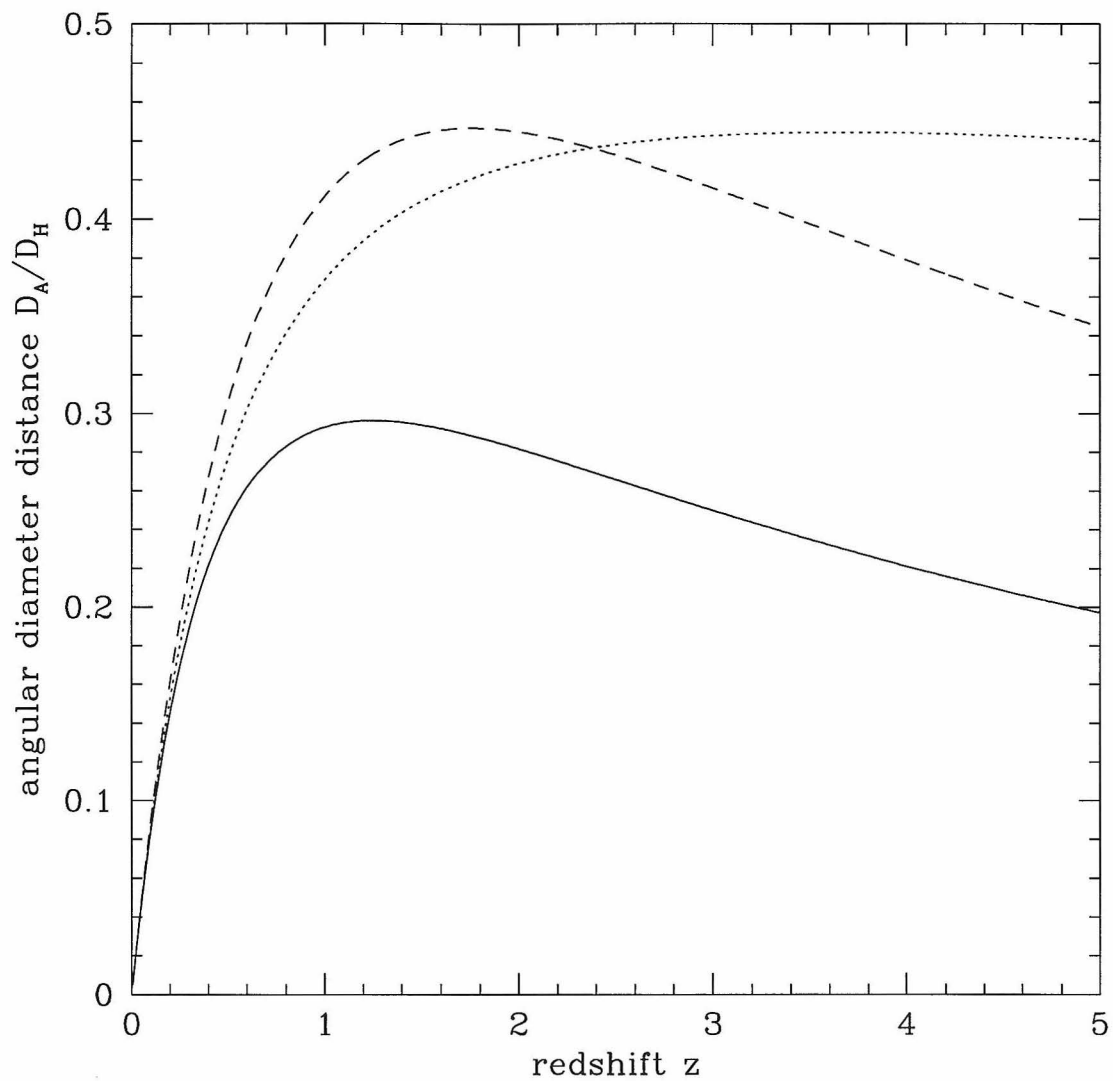


Figure B.2: The dimensionless angular diameter distance D_A/D_H . The three curves are for the three world models, $(\Omega_M, \Omega_\Lambda) = (1, 0)$, solid; $(0.05, 0)$, dotted; and $(0.2, 0.8)$, dashed.

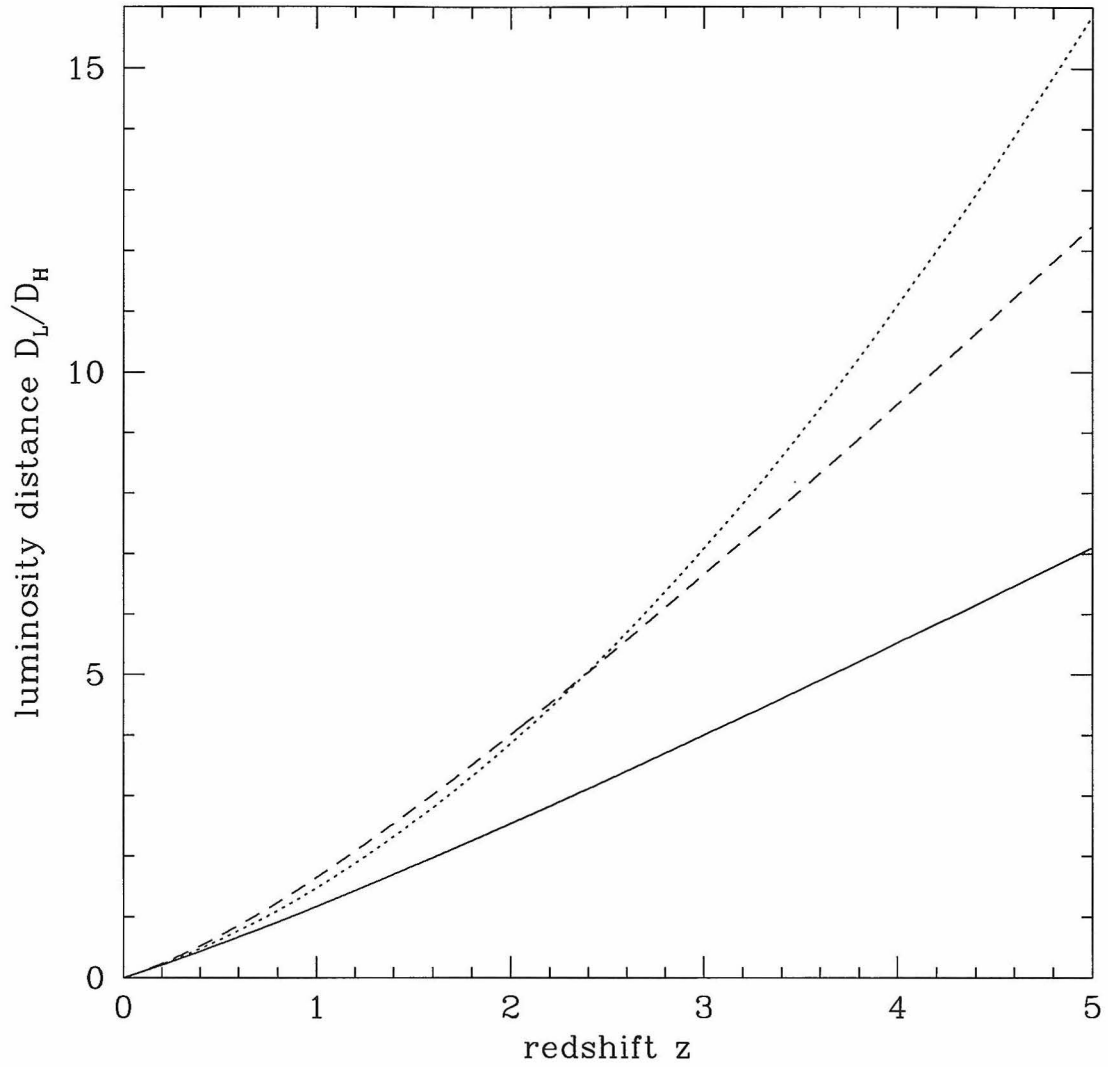


Figure B.3: The dimensionless luminosity distance D_L/D_H . The three curves are for the three world models, $(\Omega_M, \Omega_\Lambda) = (1, 0)$, solid; $(0.05, 0)$, dotted; and $(0.2, 0.8)$, dashed.

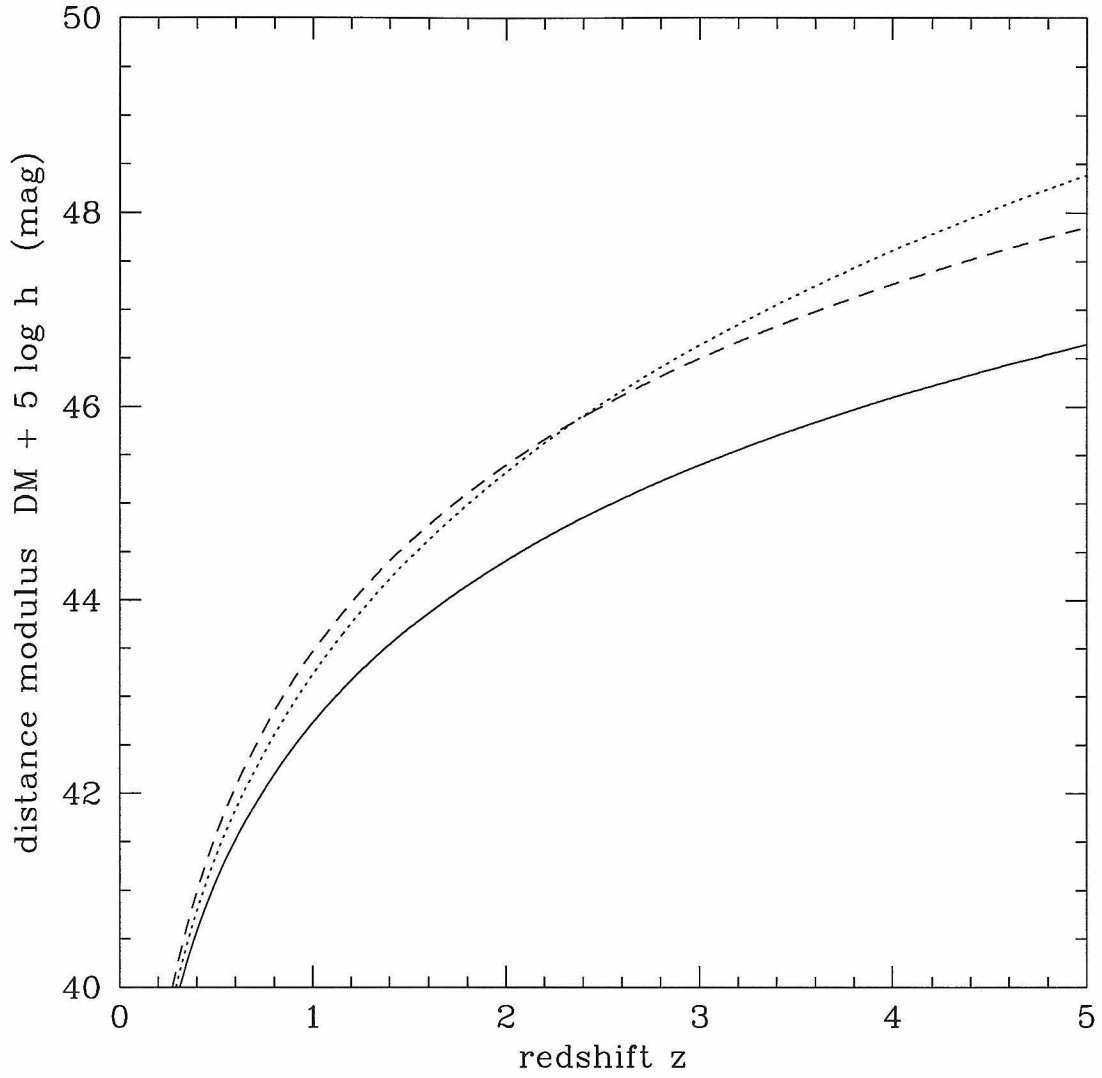


Figure B.4: The distance modulus DM . The three curves are for the three world models, $(\Omega_M, \Omega_\Lambda) = (1, 0)$, solid; $(0.05, 0)$, dotted; and $(0.2, 0.8)$, dashed.

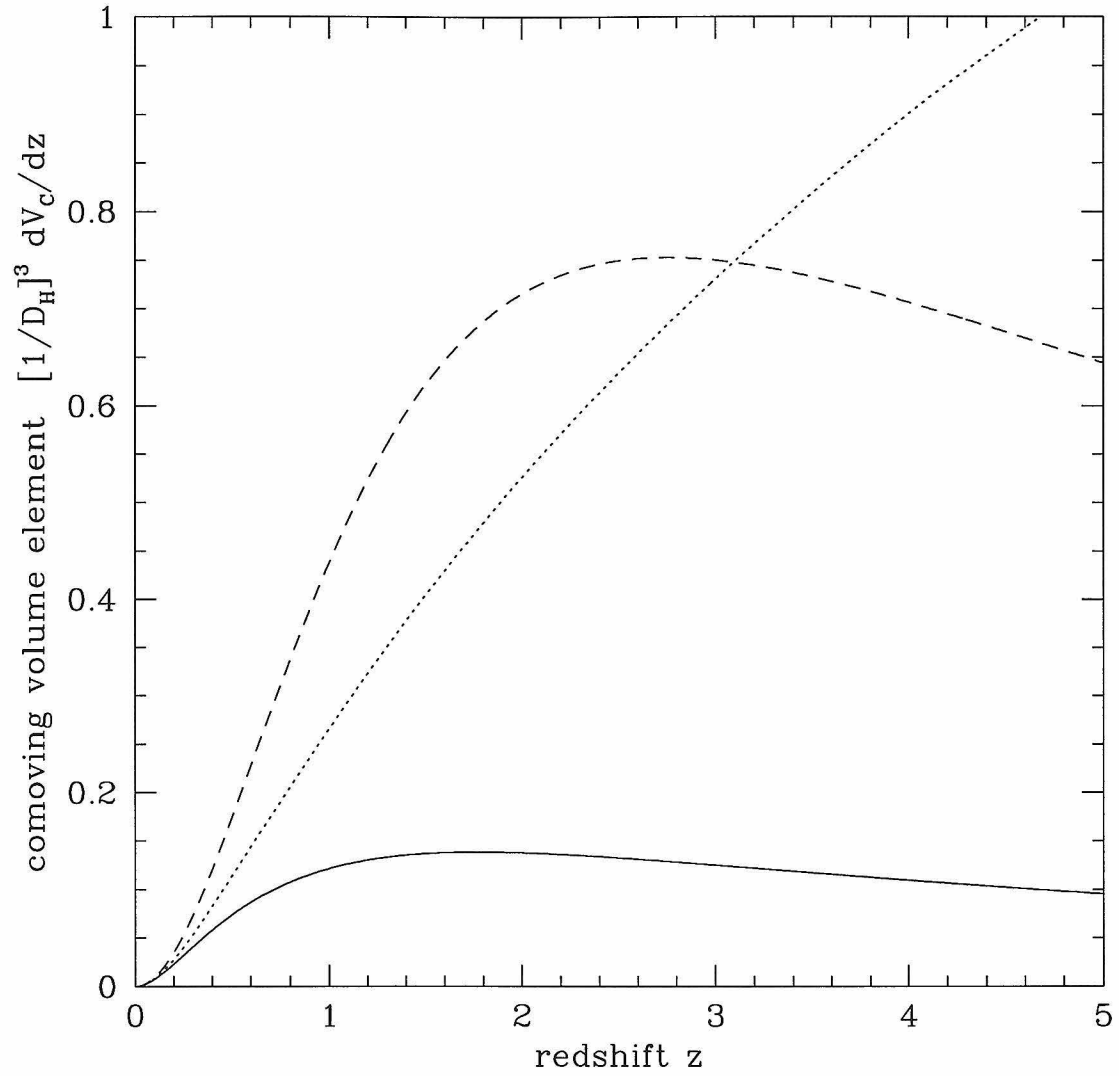


Figure B.5: The dimensionless comoving volume element $(1/D_H)^3 (dV_C/dz)$. The three curves are for the three world models, $(\Omega_M, \Omega_\Lambda) = (1, 0)$, solid; $(0.05, 0)$, dotted; and $(0.2, 0.8)$, dashed.

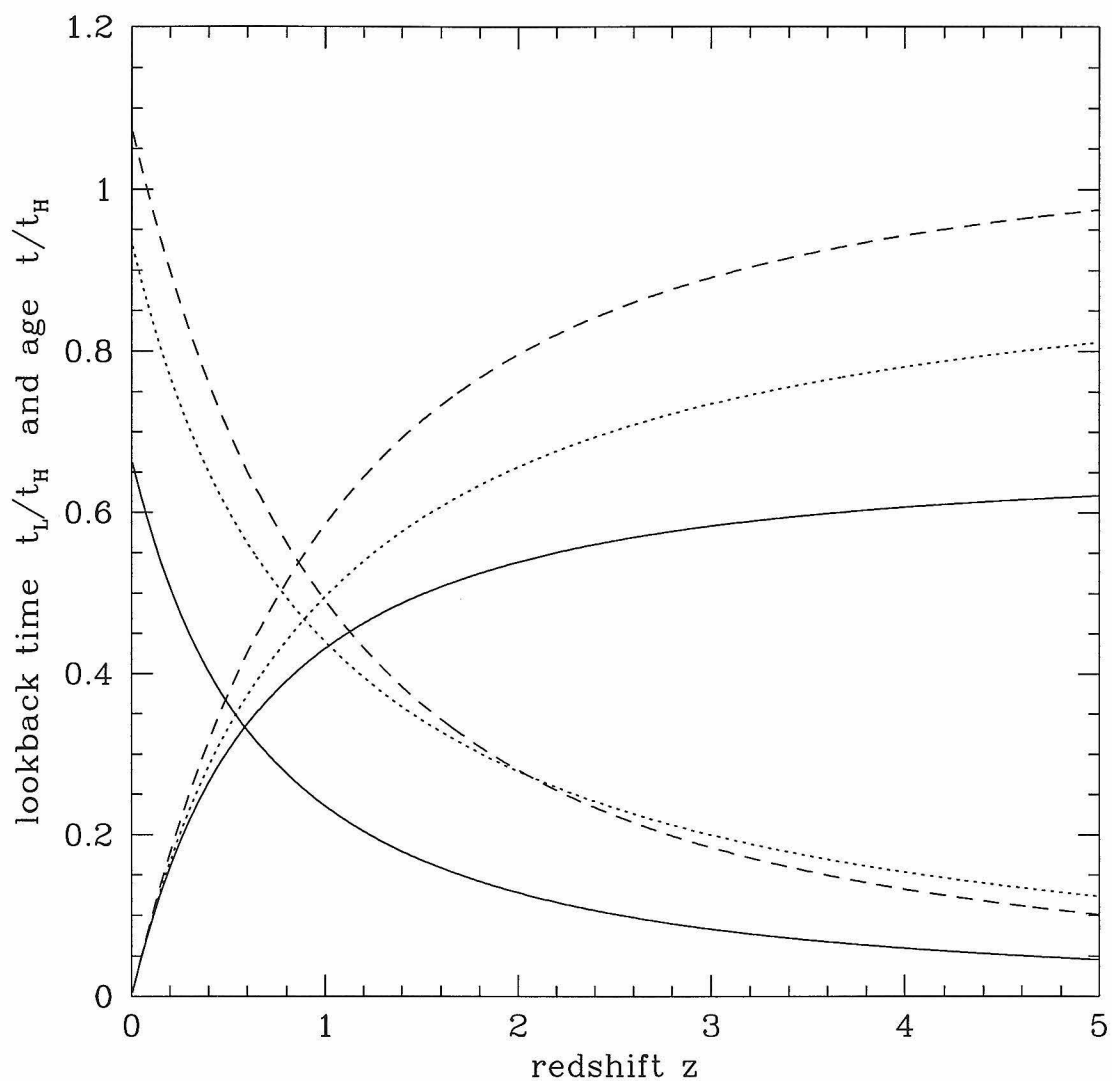


Figure B.6: The dimensionless lookback time t_L/t_H and age t/t_H . Curves cross at the redshift at which the Universe is half its present age. The three curves are for the three world models, $(\Omega_M, \Omega_\Lambda) = (1, 0)$, solid; $(0.05, 0)$, dotted; and $(0.2, 0.8)$, dashed.

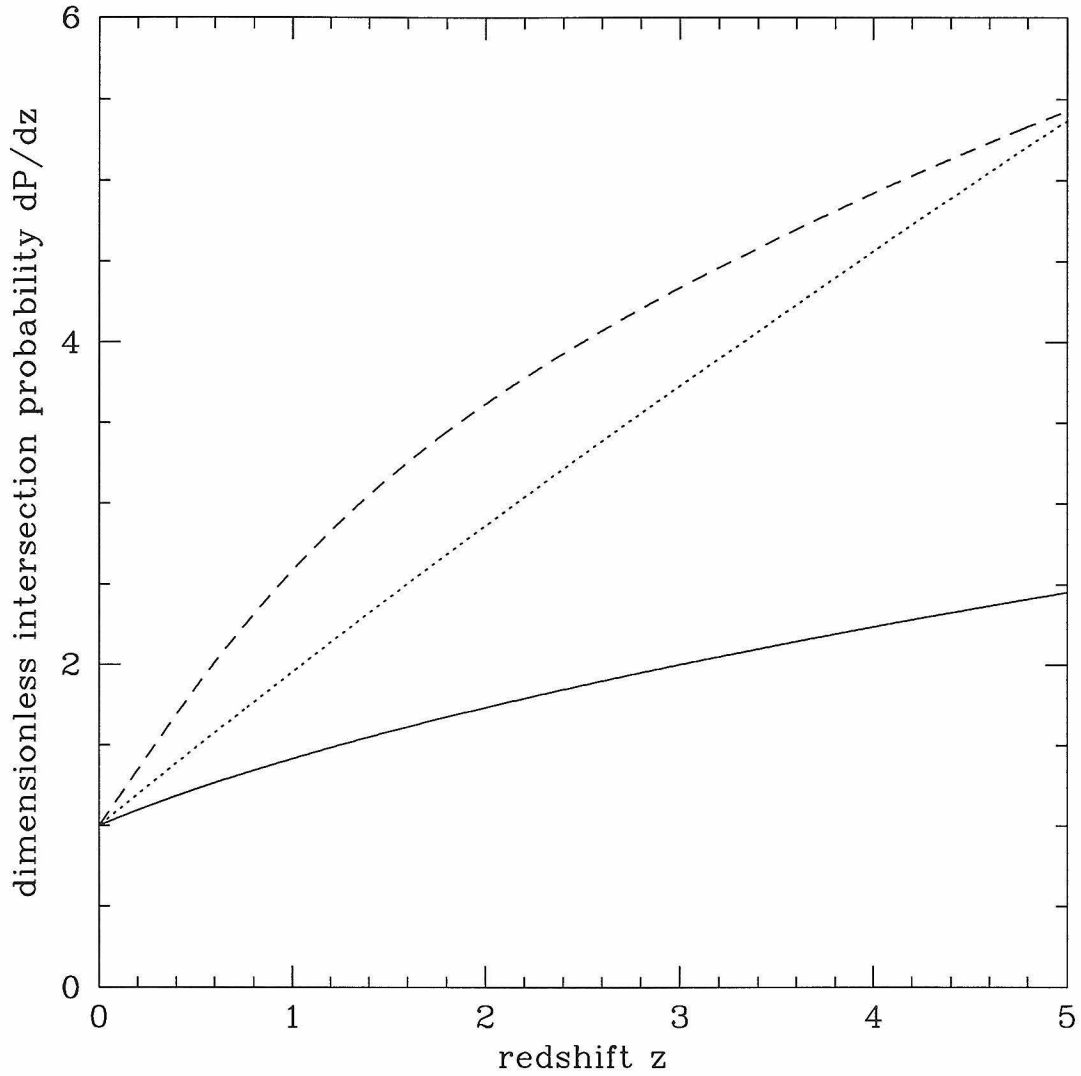


Figure B.7: The dimensionless differential intersection probability dP/dz ; dimensionless in the sense of $n(z) \sigma(z) D_H = 1$. The three curves are for the three world models, $(\Omega_M, \Omega_\Lambda) = (1, 0)$, solid; $(0.05, 0)$, dotted; and $(0.2, 0.8)$, dashed.

Appendix C Computer code

C.1 Cosmography routines in “cosmography.c”

```

/* -----
   Cosmography routines in C.
-----
   David W. Hogg
   hogg@tapir.caltech.edu
----- */

#define PI      (3.141592653589793238462643)
#define TINY    (1.0e-16)
#define NSTEPS  100
#define MAXSTEP (1.0/((double) NSTEPS))

/* -----
   angdidis.c
-----
   This function calculates the angular diameter distance d_A as a
   function of z, Omega_M and Omega_L in a matter-dominated universe,
   using the function propmotdis().  H0=c=1.
----- */
double angdidis(z,OmegaM,OmegaL)
    double z,OmegaM,OmegaL ;
{
    double propmotdis() ;
    return propmotdis(z,OmegaM,OmegaL)/(1.0+z) ;
}

/* -----
   angdidis2.c
-----
   This function calculates the angular diameter distance d_A from z1
   to z2 as a function of Omega_M and Omega_L in a matter-dominated
   universe, using the function propmotdis().  H0=c=1.
----- */
double angdidis2(z1,z2,OmegaM,OmegaL)
    double z1,z2,OmegaM,OmegaL ;
{
    double propmotdis(),sqrt(),y1,y2,y12,OmegaR ;

    OmegaR= 1.0-OmegaM-OmegaL ;

```

```

y1= propmotdis(z1,OmegaM,OmegaL) ;
y2= propmotdis(z2,OmegaM,OmegaL) ;
y12= y2*sqrt(1.0+y1*y1*OmegaR)-y1*sqrt(1.0+y2*y2*OmegaR) ;

return y12/(1.0+z2) ;
}

/* -----
comdis.c
-----
This function calculates the line-of-sight comoving distance d_C as
a function of z, Omega_M and Omega_L in a matter-dominated
universe, using dcomdisdz(). HO=c=1.
----- */
double comdis(z,OmegaM,OmegaL)
    double z,OmegaM,OmegaL ;
{
    double dz,dC,zz,dcomdisdz() ;

    dz= z/((double) NSTEPS) ;
    if(dz>MAXSTEP) dz=MAXSTEP ;
    dC= 0.0 ;
    for(zz=0.5*dz; zz<z; zz+=dz) dC += dz*dcomdisdz(zz,OmegaM,OmegaL) ;

    return dC ;
}

/* -----
comvol.c
-----
This function calculates the all-sky comoving volume V as a
function of z, Omega_M and Omega_L in a matter-dominated universe.
Formulae from Carrol, Press & Turner, 1992, and my own calculation.
----- */
double comvol(z,OmegaM,OmegaL)
    double z,OmegaM,OmegaL ;
{
    double V,dM,OmegaK,sqrtOmegaK,sqrt(),fabs(),asin(),asinh(),propmotdis() ;

    OmegaK= 1.0-OmegaM-OmegaL ;
    sqrtOmegaK= sqrt(fabs(OmegaK)) ;
    dM= propmotdis(z,OmegaM,OmegaL) ;

    if(OmegaK < -TINY)
        V= (dM*sqrt(1.0+OmegaK*dM*dM)-asin(dM*sqrtOmegaK)/sqrtOmegaK)
            /(2.0*OmegaK) ;
    else if(OmegaK > TINY)
        V= (dM*sqrt(1.0+OmegaK*dM*dM)-asinh(dM*sqrtOmegaK)/sqrtOmegaK)
            /(2.0*OmegaK) ;
    else
        V= dM*dM*dM/3.0 ;
}

```

```

return 4.0*PI*V ;
}

/* -----
dcomdisdz.c
-----
This function calculates the differential line-of-sight comoving
distance dD_c/dz as a function of z, Omega_M and Omega_L in a
matter-dominated universe. H0=c=1.
----- */
double dcomdisdz(z,OmegaM,OmegaL)
    double z,OmegaM,OmegaL ;
{
    double sqrt() ;
    return (1.0/sqrt((1.0+z)*(1.0+z)*(1.0+OmegaM*z)-z*(2.0+z)*OmegaL)) ;
}

/* -----
dcomvoldz.c
-----
This function calculates the one-steradian differential comoving
volume dV/dz as a function of z, Omega_M and Omega_L in a
matter-dominated universe. Formulae from Carrol, Press & Turner,
1992, Kolb & Turner, 1990, and my own calculation. H0=c=1.
----- */
double dcomvoldz(z,OmegaM,OmegaL)
    double z,OmegaM,OmegaL ;
{
    double dM,OmegaK,ddMdz,sqrt(),propmotdis(),dpropmotdisdz() ;

    OmegaK= 1.0-OmegaM-OmegaL ;
    dM= propmotdis(z,OmegaM,OmegaL) ;
    ddMdz= dpropmotdisdz(z,OmegaM,OmegaL) ;

    return dM*dM*ddMdz/sqrt(1.0+OmegaK*dM*dM) ;
}

/* -----
dlookbackdz.c
-----
This function calculates the change in lookback time dt/dz with
redshift z as a function of z, Omega_M and Omega_L in a
matter-dominated universe. Formula from Carrol, Press & Turner,
1992. H0=c=1.
----- */
double dlookbackdz(z,OmegaM,OmegaL)
    double z,OmegaM,OmegaL ;
{
    double sqrt() ;

```

```

return 1.0/((1.0+z)*sqrt((1.0+z)*(1.0+z)*(1.0+OmegaM*z)-z*(2.0+z)*OmegaL)) ;
}

```

```

/* -----
doptdepthdz.c
-----

```

This function calculates the change in optical depth $d\tau/dz$ with redshift z as a function of z , Ω_M and Ω_L in a matter-dominated universe. Formula from Peebles, 1993.
 $H_0=c=\sigma=n=1.$

```

----- */
double doptdepthdz(z, OmegaM, OmegaL)
    double z, OmegaM, OmegaL ;
{
    double sqrt() ;
    return (1.0+z)*(1.0+z)/
        sqrt((1.0+z)*(1.0+z)*(1.0+OmegaM*z)-z*(2.0+z)*OmegaL) ;
}

```

```

/* -----
dpropmotdisdz.c
-----

```

This function calculates the derivative of the proper motion distance d_M with respect to redshift z as a function of z , Ω_M and Ω_L in a matter-dominated universe. Formula from Carroll, Press & Turner, 1992. This function also requires the function `propmotdis()`. $H_0=c=1.$

```

----- */
double dpropmotdisdz(z, OmegaM, OmegaL)
    double z, OmegaM, OmegaL ;
{
    double ddMdz, OmegaK, dM, sqrt(), propmotdis() ;

    ddMdz = 1.0/sqrt((1.0+z)*(1.0+z)*(1.0+OmegaM*z)-z*(2.0+z)*OmegaL) ;

    OmegaK= 1.0-OmegaM-OmegaL ;
    if(OmegaK < -TINY){
        dM= propmotdis(z, OmegaM, OmegaL) ;
        ddMdz= sqrt(1.0-OmegaK*dM*dM)*ddMdz ;
    }else if(OmegaK > TINY){
        dM= propmotdis(z, OmegaM, OmegaL) ;
        ddMdz= sqrt(1.0+OmegaK*dM*dM)*ddMdz ;
    }

    return ddMdz ;
}

```

```

/* -----
intcomvol.c
-----

```

This function calculates the all-sky comoving volume V as a function of z , Ω_M and Ω_L in a matter-dominated universe by integrating `dcomvoldz()`. It was written to test `comvol()`.

```
----- */
double intcomvol(z, OmegaM, OmegaL)
    double z, OmegaM, OmegaL ;
{
    double dz, zz, V, dcomvoldz() ;

    dz= z/((double) NSTEPS) ;
    if(dz>MAXSTEP) dz=MAXSTEP ;
    V= 0.0 ;
    for(zz=0.5*dz; zz<z; zz+=dz) V+= dz*dcomvoldz(zz, OmegaM, OmegaL) ;

    return 4.0*PI*V ;
}
```

```
/* -----
lookback.c
-----

This function calculates the lookback time  $t(0)-t(z)$  as a function
of  $z$ ,  $\Omega_M$  and  $\Omega_L$  by integrating the output of dlookbackdz.
----- */
double lookback(z, OmegaM, OmegaL)
    double z, OmegaM, OmegaL ;
{
    double t, zz, dz, dlookbackdz() ;

    dz= z/((double) NSTEPS) ;
    if(dz>MAXSTEP) dz=MAXSTEP ;
    t= 0.0 ;
    for(zz=0.5*dz; zz<z; zz+=dz) t+= dlookbackdz(zz, OmegaM, OmegaL)*dz ;

    return t ;
}
```

```
/* -----
lumdis.c
-----

This function calculates the luminosity distance  $d_L$  as a function
of  $z$ ,  $\Omega_M$  and  $\Omega_L$  in a matter-dominated universe, using the
function propmotdis().  $H_0=c=1$ .
----- */
double lumdis(z, OmegaM, OmegaL)
    double z, OmegaM, OmegaL ;
{
    double propmotdis() ;
    return propmotdis(z, OmegaM, OmegaL)*(1.0+z) ;
}
```

```

/* -----
optdepth.c
-----

This function calculates the optical depth tau as a function
of z, OmegaM and OmegaL by integrating the output of doptdepthdz.
Again, H0=c=sigma=n=1.
----- */
double optdepth(z,OmegaM,OmegaL)
    double z,OmegaM,OmegaL ;
{
    double tau,zz,dz,doptdepthdz() ;

    dz= z/((double) NSTEPS) ;
    if(dz>MAXSTEP) dz=MAXSTEP ;
    tau= 0.0 ;
    for(zz=0.5*dz; zz<z; zz+=dz) tau+= doptdepthdz(zz,OmegaM,OmegaL)*dz ;

    return tau ;
}

/* -----
propmotdis.c
-----

This function calculates the proper motion distance d_M as a
function of z, Omega_M and Omega_L in a matter-dominated universe.
Formulae from Carrol, Press & Turner, 1992, Kolb \& Turner, 1990,
and my own derivation. Makes use of comdis(). H0=c=1.
----- */
double propmotdis(z,OmegaM,OmegaL)
    double z,OmegaM,OmegaL ;
{
    double dM,q0,OmegaK,sqrtOmegaK,sqrt(),fabs(),sin(),sinh() ;

    if(OmegaM<TINY && OmegaL<TINY){
        dM= (z+0.5*z*z)/(1.0+z) ;

    }else if(OmegaL<TINY){
        q0= 0.5*OmegaM-OmegaL ;
        dM= (z*q0+(q0-1.0)*(sqrt(2.0*q0*z+1.0)-1.0))/(q0*q0*(1.0+z)) ;

    }else{
        dM= comdis(z,OmegaM,OmegaL) ;
        OmegaK= 1.0-OmegaM-OmegaL ;
        sqrtOmegaK= sqrt(fabs(OmegaK)) ;
        if(OmegaK < -TINY) dM= sin(sqrtOmegaK*dM)/sqrtOmegaK ;
        else if(OmegaK > TINY) dM= sinh(sqrtOmegaK*dM)/sqrtOmegaK ;
    }

    return dM ;
}

```

C.2 Luminosity function estimation and simulation routines in "glf.c"

```

/* -----
   glf.c Galaxy Luminosity Function Package
-----
   David W. Hogg / hogg@tapir.caltech.edu / September 1997
-----

These routines estimate or construct the galaxy luminosity function
starting with a list of galaxy fluxes and redshifts. The galaxy
list must be complete from some maximum to some minimum flux,
although not all objects need to have measured redshifts.

The input lists are: "flux" containing log fluxes in (nu S_nu) in
SI units; "index" containing exponents n in the formula (nu S_nu)
propto nu^n; "redshift" containing redshifts; and "flag" containing
a flag indicating the status of the object

    flag == OKAY      Galaxy, redshift obtained
           NOTGAL     Not a galaxy (i.e., star or quasar or whatever)
           NOTOBS     Not observed spectroscopically
           NOID       Observed but no redshift obtained

Categories 2 and 3 are different because really, in category 3,
there is *some* information about the object, which can be used in
a number of ways. Some of the routines make assumptions about the
redshift distribution of the category 2 and 3 objects, some don't
need to.

The routines take fluxmin,fluxmax,zmin,zmax as inputs; these are
the flux and redshift limits of the survey (or subsample under
study). The lists are chopped at these limits. They take
solidangle as the solid angle of the survey in steradians.

Requires additional routines in "cosmography.c" and Numerical
Recipes routines "ran1.c" and "gasdev.c" (with floats converted to
doubles).

----- */
#include <stdio.h>

/* -----
   Definitions: all quantities in SI units, H_0 = 100 (km/s)/Mpc
----- */

#define SQR(x) ((x)*(x))
#define PI (3.141592653589793238462643)
#define LOG104PI (1.09920986)
#define LN10 (2.3025850930)

#define OKAY 0          /* flag definitions: OKAY, NOTGAL, NOTOBS, NOID */
#define NOTGAL 1
#define NOTOBS 2

```

```

#define NOID 3

#define NURATIO (1.57) /* ratio of frequency at which L is computed to
    frequency at which S is observed. */
#define RZERO (-7.92) /* \cal R-band zeropoint in nu F_nu, W/m^2 */

#define Dz (0.075) /* redshift step-size for integrating; tests show that
    0.075 is adequate for analyzing surveys of 300
    objects to z=1 */
#define Dflux (0.09) /* log flux step-size for integrating; tests show that
    0.09 is adequate for analyzing surveys of 300
    objects */
#define dH (9.2570e25) /* Hubble distance in meters, h=1 */
#define MAXPEAK 128 /* maximum number of redshift peaks for simulations */
#define DPEAK (0.03) /* mean comoving distance (in dH units) between peaks;
    0.03 is about right for a three-field survey, since
    0.09 is about right for a single-field survey. */
#define FPEAK (0.50) /* fraction of objects in peaks in simulations; 0.5
    is realistic */
#define xMIN (0.001) /* minimum L/Lstar in simulations */
#define xMAX (100.0) /* maximum L/Lstar in simulations */

#define TINY (1.0e-30)
#define MAXGPTS 5000 /* max grid size in etagot() */
#define MAXLINE 256 /* max line length in etagot() */

#define MS (0.2) /* L-direction metric in etagot() */
#define Mn (0.4) /* n-direction metric in etagot() */
#define Mz (0.04) /* z-direction metric in etagot() */

/* -----
    vmax()
    -----
    Construct the galaxy luminosity function by the 1/Vmax method, with
    a generalized Vmax that has both upper and lower redshift and flux
    cutoffs. This function takes as input the source lists and a set
    of luminosity bins, as well as an array to hold the constructed
    luminosity function phibin (and uncertainties errbin) in the bins.

    WARNING: This function puts all sources with luminosities outside
    the range of the bins into the first and last bins. So an upturn
    at either end could simply be this effect.
    ----- */
void vmax(flux,index,redshift,flag,ns,logLbin,phibin,errbin,nbin,
    fluxmin,fluxmax,zmin,zmax,OmegaM,OmegaL)
    int flag[],ns,nbin ;
    double flux[],index[],redshift[],logLbin[],phibin[],errbin[],
    fluxmin,fluxmax,zmin,zmax,OmegaM,OmegaL ;
{
/* --- Declare and initialize functions and variables. Zero bins. */
    int s,bin ;
    double fabs(),luminosity(),etatry(),etagot(),dcomvoldz(),sqrt(),newflux(),
    Vm,logL,z,S,delta,dlogL ;

```

```

    for(bin= 0 ; bin<nbin ; bin++) phibin[bin]=0.0 ;
/* --- Begin loop over galaxies. */
    for(s= 0 ; s<ns ; s++){
/* --- If the object is okay, compute luminosity. */
        if(flag[s]==OKAY && flux[s]>fluxmin && flux[s]<fluxmax
&& redshift[s]>zmin && redshift[s]<zmax){
            logL= luminosity(flux[s],index[s],redshift[s],OmegaM,OmegaL) ;
/* --- Find relvant luminosity bin. */
            bin= 0 ;
            do{
delta= fabs(logL-logLbin[bin++]) ;
            }while(delta>fabs(logL-logLbin[bin])) ;
            bin-- ;
/* --- Integrate volume from zmin to zmax, times completeness functions. */
            Vm= 0.0 ;
            for(z= zmin+0.5*Dz ; z<zmax ; z+=Dz){
S= newflux(z,flux[s],index[s],redshift[s],OmegaM,OmegaL) ;
if(S>fluxmin && S<fluxmax){
            Vm+= Dz*dcomvoldz(z,OmegaM,OmegaL)*etatry(S,index[s])
                *etagot(S,index[s],z) ;
        }
    }
/* --- Increment bin by 1/volume, error bin by square of that */
    if(Vm>TINY){
phibin[bin]+= 1.0/Vm ;
errbin[bin]+= 1.0/(Vm*Vm) ;
    }
}
}
/* --- Divide by bin width in log L and compute errors */
for(bin= 0 ; bin<nbin ; bin++){
    if(bin==0) dlogL= fabs(logLbin[1]-logLbin[0]) ;
    else if(bin==nbin-1) dlogL= fabs(logLbin[nbin-1]-logLbin[nbin-2]) ;
    else dlogL= 0.5*fabs(logLbin[bin+1]-logLbin[bin-1]) ;
    phibin[bin]= phibin[bin]/dlogL ;
    errbin[bin]= sqrt(errbin[bin])/dlogL ;
}
}

/* -----
asf()
-----
Estimate luminosity function parameters by the "arbitrary selection
function" maximum-likelihood technique. In addition to the source
lists, this function takes as input a set of L-star and alpha
values to try and an array to hold the derived likelihoods.
----- */
int asf(flux,index,redshift,flag,ns,logLstar,alpha,Like,nlf,
fluxmin,fluxmax,zmin,zmax,OmegaM,OmegaL)
    int flag[],ns,nlf ;
    double flux[],index[],redshift[],logLstar[],alpha[],Like[],
        fluxmin,fluxmax,zmin,zmax,OmegaM,OmegaL ;
{

```

```

/* --- Declare and initialize functions and variables. */
int s,lf,best ;
double asf1() ;
best= 0 ;
/* --- Begin loop over luminosity function models. */
for(lf= 0 ; lf<nlf ; lf++){
    Like[lf]= 0.0 ;
/* --- Begin loop over sources, incrementing the likelihoods of all the GLF
--- models if the object is in the subsample and okay. */
for(s= 0 ; s<ns ; s++){
    if(flag[s]==OKAY && flux[s]>fluxmin && flux[s]<fluxmax
&& redshift[s]>zmin && redshift[s]<zmax){
Like[lf]+= asf1(flux[s],index[s],redshift[s],logLstar[lf],
alpha[lf],zmin,zmax,OmegaM,OmegaL) ;
    }
}
/* --- Update best value, if necessary */
if(Like[lf]>Like[best]) best= lf ;
}
/* --- Return index of best luminosity function model. */
return best ;
}

/* -----
asf1()
-----

Compute the (log10) likelihood of getting a galaxy with the input
redshift, given its flux, its index, the luminosity function
parameters, redshift range, and world model.

Remember L-star is given in log10 SI units with h=1. Since we are
working in log space we use x*schechter(x,alpha) instead of simply
schechter(x,alpha) for the flux distribution.
----- */
double asf1(flux,index,redshift,Lstar,alpha,zmin,zmax,OmegaM,OmegaL)
    double flux,index,redshift,Lstar,alpha,zmin,zmax,OmegaM,OmegaL ;
{
/* --- Declare functions and variables. */
double log10(),pow(),dcomvoldz(),schechter(),luminosity(),etagot(),
z,L,x,dp,p,ptotal ;
/* --- Get the probability density p at this redshift. */
L= luminosity(flux,index,redshift,OmegaM,OmegaL) ;
x= pow(10.0,L-Lstar) ;
p= x*schechter(x,alpha)*etagot(flux,index,redshift) ;
/* --- Loop over redshifts to integrate the probability density to ptotal. */
ptotal= 0.0 ;
for(z= zmin+0.5*Dz ; z<zmax ; z+= Dz){
/* --- Compute probability increment and add it. */
L= luminosity(flux,index,z,OmegaM,OmegaL) ;
x= pow(10.0,L-Lstar) ;
dp= Dz*dcomvoldz(z,OmegaM,OmegaL)*
x*schechter(x,alpha)*etagot(flux,index,z) ;
ptotal+= dp ;
}
}

```

```

}
/* --- Return the likelihood, p/ptotal, after catching underflows. */
p= p/ptotal ;
if(p<TINY){
    fprintf(stderr,"#") ;
    p= TINY ;
}
return log10(p) ;
}

/* -----
sty()
-----

Estimate luminosity function parameters by the "Sandage, Tamann and
Yahil" maximum-likelihood technique. In addition to the source
lists, this function takes as input a set of L-star and alpha
values to try and an array to hold the derived likelihoods.
----- */

int sty(flux,index,redshift,flag,ns,logLstar,alpha,Like,nlf,
fluxmin,fluxmax,zmin,zmax,OmegaM,OmegaL)
    int flag[],ns,nlf ;
    double flux[],index[],redshift[],logLstar[],alpha[],Like[],
    fluxmin,fluxmax,zmin,zmax,OmegaM,OmegaL ;
{
/* --- Declare and initialize functions and variables. */
int s,lf,best ;
double sty1() ;
best= 0 ;
/* --- Begin loop over luminosity function models. */
for(lf= 0 ; lf<nlf ; lf++){
    Like[lf]= 0.0 ;
/* --- Begin loop over sources, incrementing the likelihoods of all the GLF
--- models if the object is in the subsample and okay. */
for(s= 0 ; s<ns ; s++){
    if(flag[s]==OKAY && flux[s]>fluxmin && flux[s]<fluxmax
&& redshift[s]>zmin && redshift[s]<zmax){
Like[lf]+= sty1(flux[s],index[s],redshift[s],logLstar[lf],alpha[lf],
fluxmin,fluxmax,OmegaM,OmegaL) ;
    }
}
/* --- Update best value, if necessary */
if(Like[lf]>Like[best]) best= lf ;
}
/* --- Return index of best luminosity function model. */
return best ;
}

/* -----
sty1()
-----

Compute the (log10) likelihood of getting a galaxy with the input
flux, given its redshift, its index, the luminosity function
parameters, flux range, and world model.

```

```

Remember L-star is given in log10 SI units with h=1.  Since we are
working in log space we use x*schechter(x,alpha) instead of simply
schechter(x,alpha) for the flux distribution.
----- */
double sty1(flux,index,redshift,Lstar,alpha,fluxmin,fluxmax,OmegaM,OmegaL)
    double flux,index,redshift,Lstar,alpha,fluxmin,fluxmax,OmegaM,OmegaL ;
{
/* --- Declare functions and variables. */
    double log10(),pow(),schechter(),luminosity(),etetry(),etaget(),
        f,L,x,dp,p,ptotal ;
/* --- Get the probability density p at this flux. */
    L= luminosity(flux,index,redshift,OmegaM,OmegaL) ;
    x= pow(10.0,L-Lstar) ;
    p= x*schechter(x,alpha)*etetry(flux,index)*etaget(flux,index,redshift) ;
/* --- Loop over fluxes to integrate the probability density to ptotal. */
    ptotal= 0.0 ;
    for(f= fluxmin+0.5*Dflux ; f< fluxmax ; f+= Dflux){
/* --- Compute probability increment and add it. */
        L= luminosity(f,index,redshift,OmegaM,OmegaL) ;
        x= pow(10.0,L-Lstar) ;
        dp= Dflux*x*schechter(x,alpha)*etetry(f,index)*etaget(f,index,redshift) ;
        ptotal+= dp ;
    }
/* --- Return the likelihood, p/ptotal, after catching underflows. */
    p= p/ptotal ;
    if(p<TINY){
        fprintf(stderr,"#") ;
        p= TINY ;
    }
    return log10(p) ;
}

/* -----
    bfr()
----- */

Estimate luminosity function parameters by the "Bivariate
Flux-Redshift" maximum-likelihood technique.  In addition to the
source lists, this function takes as input a set of L-star and
alpha values to try and an array to hold the derived likelihoods.
----- */

int bfr(flux,index,redshift,flag,ns,logLstar,alpha,Like,nlf,
fluxmin,fluxmax,zmin,zmax,OmegaM,OmegaL)
    int flag[],ns,nlf ;
    double flux[],index[],redshift[],logLstar[],alpha[],Like[],
        fluxmin,fluxmax,zmin,zmax,OmegaM,OmegaL ;
{
/* --- Declare and initialize functions and variables. */
    int s,lf,best ;
    double bfr1() ;
    best= 0 ;
/* --- Begin loop over luminosity function models. */
    for(lf= 0 ; lf< nlf ; lf++){

```

```

    Like[lf]= 0.0 ;
/* --- Begin loop over sources, incrementing the likelihoods of all the GLF
--- models if the object is in the subsample and okay. */
    for(s= 0 ; s< ns ; s++){
        if(flag[s]==OKAY && flux[s]>fluxmin && flux[s]<fluxmax
        && redshift[s]>zmin && redshift[s]<zmax){
Like[lf]+= bfr1(flux[s],index[s],redshift[s],logLstar[lf],alpha[lf],
fluxmin,fluxmax,zmin,zmax,OmegaM,OmegaL) ;
        }
    }
/* --- Update best value, if necessary */
    if(Like[lf]> Like[best]) best= lf ;
}
/* --- Return index of best luminosity function model. */
return best ;
}

/* -----
bfr1()
-----

Compute the (log10) likelihood of getting a galaxy with the input
flux and redshift, given its index, the luminosity function
parameters, flux range, redshift range, and world model.

Remember L-star is given in log10 SI units with h=1. Since we are
working in log space we use x*schechter(x,alpha) instead of simply
schechter(x,alpha) for the flux distribution.

NB: the normalization (ptotal) integral is very similar for
different galaxies, although it is computed separately for every
one. The integral depends only on the index (and LF parameters
etc). It would be possible to greatly speed this up by having the
routine remember a table of integrated ptotals.
----- */
double bfr1(flux,index,redshift,Lstar,alpha,fluxmin,fluxmax,zmin,zmax,
    OmegaM,OmegaL)
    double flux,index,redshift,Lstar,alpha,fluxmin,fluxmax,zmin,zmax,
    OmegaM,OmegaL ;
{
/* --- Declare functions and variables. */
    double log10(),pow(),schechter(),luminosity(),dcomvoldz(),etetry(),etagot(),
    f,z,L,x,dp,p,ptotal,dV ;
/* --- Get the probability density p at this flux. */
    L= luminosity(flux,index,redshift,OmegaM,OmegaL) ;
    x= pow(10.0,L-Lstar) ;
    p= x*schechter(x,alpha)*etetry(flux,index)*etagot(flux,index,redshift) ;
/* --- Loop over redshifts and fluxes to integrate the probability density
--- to ptotal. */
    ptotal= 0.0 ;
    for(z= zmin+0.5*Dz ; z< zmax ; z+= Dz){
        dV= Dz*dcomvoldz(z,OmegaM,OmegaL) ;
        for(f= fluxmin+0.5*Dflux ; f< fluxmax ; f+= Dflux){
/* --- Compute probability increment and add it. */

```

```

    L= luminosity(f,index,z,OmegaM,OmegaL) ;
    x= pow(10.0,L-Lstar) ;
    dp= dV*Dflux*x*schechter(x,alpha)*etatry(f,index)*etagot(f,index,z) ;
    ptotal+= dp ;
  }
}
/* --- Return the likelihood, p/ptotal, after catching underflows. */
p= p/ptotal ;
if(p<TINY){
  fprintf(stderr,"#") ;
  p= TINY ;
}
return log10(p) ;
}

/* -----
count()
-----

Compute the contribution to one point in the number counts dN/dlogS
in one steradian at input (log) flux (log nu S_nu), from one
Schechter luminosity function component acting from redshift zmin
to zmax with phi^star=1 in Hubble volumes. An effective spectral
index neff (nu L_nu propto nu^neff) is given for k-correction.
Note that L^star is all-sphere, not just one radian.
----- */
double count(flux,Lstar,alpha,neff,zmin,zmax,OmegaM,OmegaL)
{
  double flux,Lstar,alpha,neff,zmin,zmax,OmegaM,OmegaL ;
  {
  /* --- Declare functions and variables, initialize. */
  double dcomvoldz(),pow(),luminosity(),schechter(),DV,z,x,dNdlogS ;
  dNdlogS= 0.0 ;
  /* --- Loop over redshift, computing volume increment, scaled luminosity,
  --- and count increment. */
  for(z= zmin+0.5*Dz ; z<= zmax ; z+= Dz){
    DV= Dz*dcomvoldz(z,OmegaM,OmegaL) ;
    x= pow(10.0,luminosity(flux,neff,z,OmegaM,OmegaL)-Lstar) ;
    dNdlogS+= DV*LN10*x*schechter(x,alpha) ;
  }
  return dNdlogS ;
}
}

/* -----
fake()
-----

Create a simulated galaxy catalog, with redshift peaks and a
realistic completeness function in flux and redshift. The number
of objects, world model and luminosity function parameters are
input. Randomly chosen redshifts and luminosities are pulled from
the correct distributions via routines getwallredshift(),
getredshift() and getluminosity(). This function takes ns, Lstar
and alpha as input parameters and returns fluxes, indices,
redshifts and flags.
----- */

```

```

int fake(flux,index,redshift,flag,ns,Lstar,alpha,fluxmin,fluxmax,zmax,
        OmegaM,OmegaL,seed)
    int flag[],ns ;
    double flux[],index[],redshift[],Lstar,alpha,fluxmin,fluxmax,zmax,
        OmegaM,OmegaL ;
    long *seed ;
{
/* --- Initialize functions and variables */
    void exit() ;
    int s,peak,NPEAK ;
    double ran1(),getredshift(),getwallredshift(),getluminosity(),getindex(),
        lum2flux(),comdis(),propmotdis(),etatry(),etagot(),zpeak[MAXPEAK],
        d2[MAXPEAK],L,x ;
/* --- Choose NPEAK "redshift peak" locations and record the transverse
    --- comoving distance squared at each peak */
    NPEAK= (int) (comdis(zmax,OmegaM,OmegaL)/DPEAK) ;
    if(NPEAK>MAXPEAK){
        fprintf(stderr,"fake(): too many peaks!\n") ;
        exit(0) ;
    }
    for(peak= 0 ; peak< NPEAK ; peak++){
        zpeak[peak]= getwallredshift(zmax,OmegaM,OmegaL,seed) ;
        d2[peak]= propmotdis(zpeak[peak],OmegaM,OmegaL)
            *propmotdis(zpeak[peak],OmegaM,OmegaL) ;
    }
/* --- Cumulate the transverse distance squared d2[] at the peaks as a tool
    --- for putting peak objects into the peaks */
    for(peak= 1 ; peak< NPEAK ; peak++){
        d2[peak]+= d2[peak-1] ;
    }
/* --- Begin loop over sources */
    s= 0 ;
    while(s< ns){
/* --- If the source is in a peak, choose one of the peak redshifts according
    --- to the d2 distribution */
        if(ran1(seed)< FPEAK){
            x= ran1(seed)*d2[NPEAK-1] ;
            peak= 0 ;
            while(x> d2[peak]) peak++ ;
            redshift[s]= zpeak[peak] ;
/* --- If not peak choose a "field" redshift */
        }else{
            redshift[s]= getredshift(zmax,OmegaM,OmegaL,seed) ;
        }
/* --- Choose a luminosity from the luminosity function */
        L= getluminosity(Lstar,alpha,seed) ;
/* --- Choose a spectral index from the index distribution */
        index[s]= getindex(seed) ;
/* --- Compute the observed flux */
        flux[s]= lum2flux(L,index[s],redshift[s],OmegaM,OmegaL) ;
/* --- Compare with flux limits to see if object is in photometric sample */
        if(flux[s]<fluxmax && flux[s]>fluxmin){
/* --- Roll dice and compare with the completeness functions, setting flags */

```

```

        flag[s]= NOTOBS ;
        if(ran1(seed) <= etatry(flux[s],index[s])){
if(ran1(seed) <= etagot(flux[s],index[s],redshift[s]))
        flag[s]= OKAY ;
else flag[s]= NOID ;
        }
        s++ ;
    }
}
/* --- Done: return number of simulated sources */
return s ;
}

/* -----
getredshift()
-----

This function uses acceptance/rejection method to return a random
redshift using the comoving volume as a distribution function. It
makes use of Numerical Recipes ran1() and my own dcomvoldz() in
cosmography.c

WARNING: it is assumed that the volume element is always less than
or equal to the Euclidean volume element. This is not true for
all world models!
----- */
double getredshift(zmax,OmegaM,OmegaL,seed)
    double zmax,OmegaM,OmegaL ;
    long *seed ;
{
    void exit() ;
    double pow(),ran1(),dcomvoldz(),Vmax,V,z,ratio ;
    Vmax= zmax*zmax*zmax ;
    do{
        V= Vmax*ran1(seed) ;
        z= pow(V,(1.0/3.0)) ;
        ratio= dcomvoldz(z,OmegaM,OmegaL)/(z*z) ;
        if(ratio>1.0){
            fprintf(stderr,"getredshift(): ERROR: ratio > 1\n") ;
            exit(0) ;
        }
    }while(ran1(seed)>ratio) ;
    return z ;
}

/* -----
getwallredshift()
-----

This function uses acceptance/rejection method to return a random
redshift using the line-of-sight comoving distance element as a
distribution function. It makes use of Numerical Recipes ran1()
and my own dcomdisdz() in cosmography.c

WARNING: it is assumed that the comoving distance element is always

```

```

less than or equal to the Euclidean distance element. This is not
necessarily true for all world models!
----- */
double getwallredshift(zmax,OmegaM,OmegaL,seed)
    double zmax,OmegaM,OmegaL ;
    long *seed ;
{
    void exit() ;
    double ran1(),dcomdisdz(),Dmax,z,ratio ;
    Dmax= zmax ;
    do{
        z= Dmax*ran1(seed) ;
        ratio= dcomdisdz(z,OmegaM,OmegaL) ;
        if(ratio>1.0){
            fprintf(stderr,"getwallredshift(): ERROR: ratio > 1\n") ;
            exit(0) ;
        }
    }while(ran1(seed)>ratio) ;
    return z ;
}

/* -----
getluminosity()
-----

This function returns a luminosity, drawn from a luminosity
function using the acceptance/rejection method. The luminosity
function is of Schechter form and the comparison function is the
corresponding power law with no exponential.
----- */
double getluminosity(Lstar,alpha,seed)
    double Lstar,alpha ;
    long *seed ;
{
    /* --- declare functions and variables */
    void exit() ;
    int flag=0 ;
    double L,x,ratio,phi,phimin,phimax,ran1(),pow(),fabs(),log(),log10(),exp() ;
    /* --- need to treat alpha=-1.0 separately; set phimin and phimax */
    if(fabs(alpha+1.0)<TINY){
        flag=1 ;
        phimax= log(xMAX) ; phimin= log(xMIN) ;
    }else{
        phimax= pow(xMIN,alpha+1.0) ; phimin= pow(xMAX,alpha+1.0) ;
    }
    do{
        /* --- choose a random number and transform to get the trial value */
        phi= phimin+(phimax-phimin)*ran1(seed) ;
        if(flag){
            x= exp(phi) ;
        }else{
            x= pow(phi,1.0/(alpha+1.0)) ;
        }
        /* --- compute and check ratio of trial function to real function */

```

```

    ratio= exp(-x) ;
    if(ratio>1.0){
        fprintf(stderr,"getluminosity(): ERROR: ratio = %e > 1\n",ratio) ;
        exit(0) ;
    }
/* --- roll dice and if a failure, try again */
}while(ran1(seed)>ratio) ;
/* --- compute and return log luminosity */
L= Lstar+log10(x) ;
return L ;
}

/* -----
getindex()
-----
Return a spectral index, drawn from the spectral index distribution.

WARNING: NOT YET IMPLEMENTED
----- */
double getindex(seed)
    long *seed ;
{
    double gasdev() ;
    return gasdev(seed)*0.91-1.6 ;
}

/* -----
newflux()
-----
Compute the flux of an object at new redshift z given its flux,
index, and actual redshift. This shows how the index n is used --
n=0 means no k-correction, in the standard terminology; n>0 means
the object is bluer so brighter at higher redshift than simple use
of the luminosity distance would suggest; vice versa for n<0.
----- */
double newflux(z,flux,index,redshift,OmegaM,OmegaL)
    double z,flux,index,redshift,OmegaM,OmegaL ;
{
    double log10(),lumdis() ;
    return (flux
    - 2.0*log10(lumdis(z,OmegaM,OmegaL)/lumdis(redshift,OmegaM,OmegaL))
    + index*log10((1.0+z)/(1.0+redshift))) ;
}

/* -----
lum2flux()
-----
Compute the (log10) flux of an object given its luminosity, index,
and redshift. Note that this uses the all-sphere (4 pi ster)
luminosity. This also shows how the index n is used -- n=0 means
no k-correction, in the standard terminology; n>0 means the object
is bluer.
----- */

```

```

double lum2flux(L,index,redshift,OmegaM,OmegaL)
    double L,index,redshift,OmegaM,OmegaL ;
{
    double log10(),lumdis() ;
    return (L - 2.0*log10(dH*lumdis(redshift,OmegaM,OmegaL))
    + index*log10((1.0+redshift)/NURATIO) - LOG104PI) ;
}

/* -----
    luminosity()
-----
    Compute the (log10) luminosity of an object given its flux, index,
    and redshift. Note that this is the all-sphere (4 pi ster)
    luminosity. This also shows how the index n is used -- n=0 means
    no k-correction, in the standard terminology; n>0 means the object
    is bluer so at high redshift it appears brighter than other objects
    with the same intrinsic luminosity but n=0; vice versa for n<0.
----- */
double luminosity(flux,index,redshift,OmegaM,OmegaL)
    double flux,index,redshift,OmegaM,OmegaL ;
{
    double log10(),lumdis() ;
    return (flux + 2.0*log10(dH*lumdis(redshift,OmegaM,OmegaL))
    - index*log10((1.0+redshift)/NURATIO) + LOG104PI) ;
}

/* -----
    schechter()
-----
    Calculate the dimensionless value of the Schechter luminosity
    function y=phi/phi_star as a function of x=L/L_star, given an
    exponent alpha.
----- */
double schechter(x,alpha)
    double x,alpha ;
{
    double pow(),exp() ;
    return (pow(x,alpha)*exp(-x)) ;
}

/* -----
    etatry()
-----
    Return the probability that a source of log flux S and spectral index
    n was observed spectroscopically. This is the a priori completeness
    function, symbolized eta_try in the thesis.
----- */
double etatry2(flux,index)
    double flux,index ;
{
    if(flux>(RZERO-0.4*22.0)) return 1.0 ;
    else if(flux>(RZERO-0.4*23.0)) return 0.8 ;
    else if(flux>(RZERO-0.4*24.0)) return 0.1 ;
}

```

```

    else return 0.0 ;
}
double etatry(flux,index)
    double flux,index ;
{
/* --- declare variables */
    void exit() ;
    static int ng=0 ;
    static double Sg[MAXGPTS],etag[MAXGPTS] ;
    FILE *fp,*fopen() ;
    char line[MAXLINE] ;
    int ig ;
    double fabs(),delta ;
/* --- if the file has not been read, read it */
    if(ng<1){
        fp= fopen("etatry.out","r") ;
        if(fp!=NULL){
            while(fgets(line,MAXLINE,fp)!=NULL && ng<MAXGPTS){
if(line[0]!='#'){
/* --- read completeness values, one per line */
                if(sscanf(line,"%lf %lf",Sg+ng,etag+ng)==2){
                    Sg[ng]= RZERO-0.4*Sg[ng] ;
                    ng++ ;
                }
            }
        }
        fprintf(stderr,"etatry(): read %d grid points from etatry.out\n",ng) ;
    }else{
        fprintf(stderr,"etatry(): no file etatry.out\n") ;
        exit(0) ;
    }
    fclose(fp) ;
}
/* --- find grid point closest to the input value, output */
    ig= 0 ;
    do{
        delta= fabs(flux-Sg[ig++]) ;
    }while(delta>fabs(flux-Sg[ig])) ;
    ig-- ;
    return etag[ig] ;
}

/* -----
    etagot()
-----

```

Read a data file and, based on its contents, return the probability of obtaining a redshift given that a spectrum has been taken. This is the a posteori completeness function, symbolized `eta_got` in the thesis. Inputs are log flux, spectral index, and redshift.

The data file has a special, immutable format which should be obvious from the code. In the one-dimensional list of completeness values, which in fact lie in a three-dimensional grid, fluxes cycle

```

fastest, then indices, and redshifts cycle slowest. Lines
beginning with '#' are ignored.
----- */
double etagot2(flux,index,redshift) double flux,index,redshift;{return 1.0;}
double etagot(flux,index,redshift)
    double flux,index,redshift ;
{
/* --- declare variables */
void exit() ;
static int ncomp= -3,nz=0,nn=0,nS=0 ;
static double Sgrid[MAXGPTS],ngrid[MAXGPTS],zgrid[MAXGPTS],
compgrid[MAXGPTS] ;
FILE *fp,*fopen() ;
char line[MAXLINE],*cpointer ;
int ibest,iz,in,iS,incr ;
double fabs(),delta ;
/* --- if the file has not been read, read it */
if(ncomp<1){
    fp= fopen("completeness.out","r") ;
    if(fp!=NULL){
        while(fgets(line,MAXLINE,fp)!=NULL && ncomp<MAXGPTS){
if(line[0]!='#'){
/* --- read completeness values, one per line */
if(ncomp>=0 && sscanf(line,"%lf",compgrid+ncomp)==1){
    ncomp++ ;
/* --- but first read grid locations in order: redshift, index, flux */
}else if(ncomp== -3){
    cpointer= line ;
    while(sscanf(cpointer,"%lf%n",zgrid+nz,&incr)==1 && nz<MAXGPTS){
        cpointer+= incr ;
        nz++ ;
    }
    ncomp++ ;
}else if(ncomp== -2){
    cpointer= line ;
    while(sscanf(cpointer,"%lf%n",ngrid+nn,&incr)==1 && nn<MAXGPTS){
        cpointer+= incr ;
        nn++ ;
    }
    ncomp++ ;
}else if(ncomp== -1){
    cpointer= line ;
    while(sscanf(cpointer,"%lf%n",Sgrid+nS,&incr)==1 && nS<MAXGPTS){
        cpointer+= incr ;
/* --- convert magnitudes to fluxes */
        Sgrid[nS]= RZERO-0.4*Sgrid[nS] ;
        nS++ ;
    }
    ncomp++ ;
}
}
}
    fprintf(stderr,"etagot(): %d points (%dx%dx%d) in completeness.out\n",

```

```

        ncomp,nz,nn,nS) ;
        if(nz*nn*nS!=ncomp){
fprintf(stderr,"etagit(): %d does not equal %dx%dx%d!\n",
ncomp,nz,nn,nS) ;
exit(0) ;
        }
        }else{
        fprintf(stderr,"etagit(): no file completeness.out\n") ;
        exit(0) ;
        }
        fclose(fp) ;
    }
/* --- WARNING: HACK: assume no incompleteness for z<0.6 */
if(redshift<0.6){
    return 1.0 ;
}
else{
/* --- find grid point closest to the input value */
    iz= in= iS= 0 ;
    do{
        delta= fabs(redshift-zgrid[iz++]) ;
    }while(delta>fabs(redshift-zgrid[iz])) ;
    iz-- ;
    do{
        delta= fabs(index-ngrid[in++]) ;
    }while(delta>fabs(index-ngrid[in])) ;
    in-- ;
    do{
        delta= fabs(flux-Sgrid[iS++]) ;
    }while(delta>fabs(flux-Sgrid[iS])) ;
    iS-- ;
/* --- return closest value */
    ibest= iz*nn*nS+in*nS+iS ;
    return compgrid[ibest] ;
    }
}

```

Biography

David Wardell Hogg was born in Toronto on 8 September 1970 to Frances Benson Hogg and Peter Wardell Hogg. He received his high school diploma from the University of Toronto Schools in June 1988, represented Canada at the 19th International Physics Olympiad in Austria that same month, and then began his undergraduate study at the Massachusetts Institute of Technology (MIT) in Cambridge in September 1988. At MIT he majored in physics, minored in philosophy, working in the MIT Media Laboratory during the academic years, and working at the Canadian Institute for Theoretical Astrophysics (CITA) in Toronto in the summers after his second and third years. He graduated in June 1992 with an SB, spent the summer working at CITA again and then moved to Pasadena to begin graduate study at the California Institute of Technology (Caltech) in September 1992. He married Heather Stratton in May 1994 but the couple separated in July 1997. At Caltech he published thirteen refereed papers, mainly in cosmology, taught a recitation section of first-year physics for four years running, wrote a set of lecture notes on Special Relativity, and completed this PhD thesis.